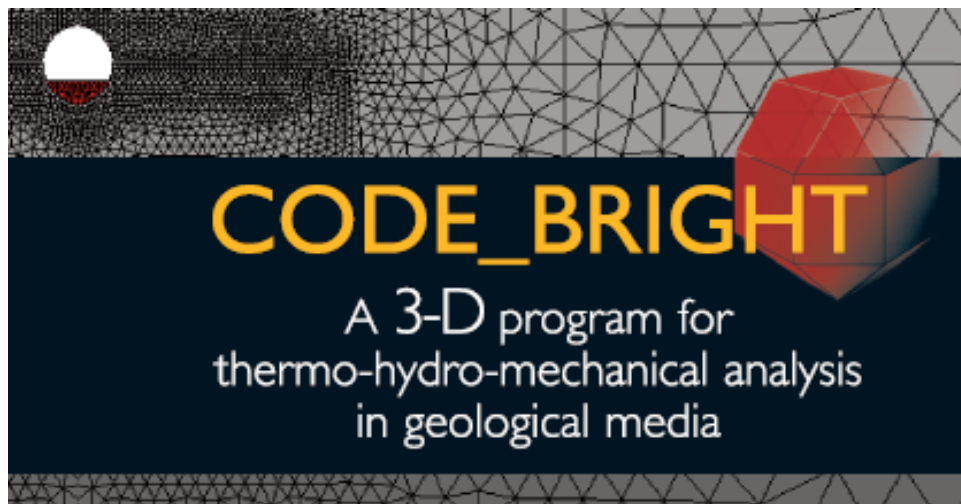


10th Workshop of CODE_BRIGHT USERS

3th May 2018
Barcelona, Spain



Department of Civil and Environmental Engineering
UPC-BarcelonaTech
Barcelona, Spain

CIMNE
International Center for Numerical Methods in Engineering
Barcelona, Spain

CODE_BRIGHT

**A 3-D program for thermo-hydro-mechanical analysis in
geological media**



10th WORKSHOP OF CODE_BRIGHT USERS

Barcelona, 3th May 2018

Department of Civil and Environmental Engineering

(UPC-BarcelonaTech, Barcelona, Spain)

CIMNE

(International Center for Numerical Methods in Engineering,
Barcelona, Spain)

CONTENTS

Viscoplastic constitutive equations for copper to model canister deformations and implementation in Code_Bright

P. Khadivipanah, S. Olivella, J. Vaunat

Heat dissipation in rock around caverns for heavy oil storage

X. Pintado

Loess slope instability under atmospheric boundary condition

L. Li, M. Datcheva, W. Baille

Water and heat fluxes in embankments under climatic actions. Modelling of a case study

V. Guachizaca, C. Villarraga, J. Vaunat, R. Oorthuis, MW. Saaltink, A. Lloret, M. Hürlimann

Three-dimensional simulation of the HE-E heater experiment performed at the Mont Terri rock laboratory (Switzerland)

L. Friedenber, K. Wiczorek, O. Czaikowski

Modelling of cement-groundwater-rock interaction at the Grimsel test site (Switzerland)

CM. Chaparro, MW. Saaltink, JM. Soler

Heating of a steel-lined micro-tunnel in the Callovo-Oxfordian formation

S. Tourchi, D. Ruiz, M. Manica, J. Vaunat, A. Gens, M. Vu

Assessment of a FEBEX model

A. Rodriguez-Dono & S. Olivella

Modelling of fiber-reinforced concrete and application case

IP. Damians, S. Olivella, C. Cots

Modelling spherical gas flow in MX80 bentonite

IP. Damians, S. Olivella, A. Gens

Modeling the reactivation of a ductile fault

V. Vilarrasa, R. Makhnenko, F. Parisio

Thermo-hydro-mechanical simulation of gas injection into fractured media

A. Zareidarmiyani, H. Salarirad, V. Vilarrasa, S. Olivella

THM modelling of methane hydrate dissociation/formation in marine sediments

M. de la Fuente, J. Vaunat, H. Marin

VISCOPLASTIC CONSTITUTIVE EQUATIONS FOR COPPER TO MODEL CANISTER DEFORMATIONS AND IMPLEMENTATION IN CODE_BRIGHT

Peiman Khadivipanah, Sebastia Olivella and Jean Vaunat

Department of Civil Engineering, Polytechnic University of Catalonia, Barcelona, Spain.

ABSTRACT

Ultimate storage of spent nuclear fuel is located in copper canisters which are surrounded by bentonite clay. After placement of the canisters, Bentonite swelling due to water saturation and hydrostatic pressure cause the canisters will be subjected to compressive loads. The canisters are constructed with a load carrying cast insert of ductile iron which is surrounded by a 50 mm thick corrosion resistant copper shell. The copper shell is not in itself load carrying but must maintain its corrosion barrier ability when the compressive load is applied very slowly. For materials where the load is applied slowly, materials creep properties are of great importance. It has been shown that creep ductility for oxygen free copper can be very low ($< 1\%$). The objective of the paper is to develop algorithms describing rate-dependent (viscoplastic) constitutive equations (Bodner and Partom model) based on a single internal state variable which is a function of plastic work are used to calculate the response of copper to change of strain rate over a range of temperatures for copper canister and Implement it in Code_Bright. Bodner-Partom constitutive equations must be checked for their validity, for this purpose, the stress-strain response of a uniaxial tensile bar at a constant velocity was computed in Code_Bright and then the results were compared with the solution obtained from Stealth Finite Difference Code.

Keywords: viscoplastic constitutive equations, copper canister, Bodner-Partom, Code_Bright

In the present work, the shear test has been modelled using the Bodner_Partom model in Code_Bright in 2D dimension. samples ($h = 622$ mm, $L = 158$ mm) made of highly compacted MX-80 bentonite surrounding a canister ($h = 450$ mm, $L = 80$ mm) made of copper were prepared. The shear test apparatus used had a housing divided into two similar parts by a plane perpendicular to the cube axis. One of these parts was held fixed and the other could be displaced perpendicularly to the cube axis. The samples were placed in the housing of the shear apparatus. Afterward, the samples were completely saturated with water, thereby inducing a swelling pressure in the bentonite. Finally, the samples were sheared.

In the upper half of geometry, the displacement of 0.001 m/s has been applied to the sample within a time interval of 30 seconds. The shear zone thickness is 30 mm. The mesh used in this model is uniform and the number of nodes and elements in this mesh are 507 and 456 respectively, as shown in Figure 1

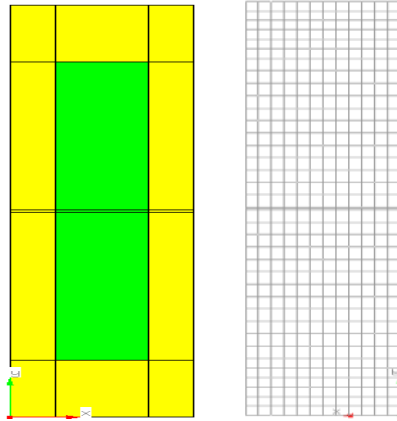


Figure 1 The geometry of Canister-clay. The canister and clay is depicted with green and yellow colors respectively and 3D finite Quadrilateral element meshes

In elasticity, a linear elastic model is used for canister in which the Poisson ratio is 0.35 and the Elastic modulus is 132999.3 MPa and for clay, the Poisson ratio is 0.49 and Elastic modulus is 304 MPa. The viscoplastic model of the copper canister is used by the Bodner-Partom model, and the main copper parameters are shown in Table 1. Mohr-Coulomb viscoplasticity for clay is investigated and clay parameters are depicted in table 2.

Table 1 Input parameters of copper.

Parameter	Value	Unit
D_0	10^4	s^{-1}
Z_1	237	MPa
m_0	0.15	$(MPa)^{-1}$
m_1	0.25	$(MPa)^{-1}$
α	0.50	$(MPa)^{-1}$

Table 2 Input parameters of clay.

Parameter	Value	Unit
m	3	
Γ_0	10^{-3}	s^{-1}
Q	0	$Jmol^{-1}$
C	3.672	$(MPa)^{-1}$
α	10^{-6}	
δ	0	

Results

After the computation in Code_Bright, the results for Canister-clay are calculated in post-process, all analyzes are shown in the following figures.

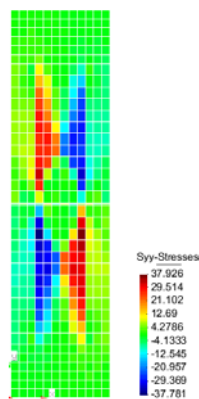


Figure 2 Contour fill of Syy-Stresses.

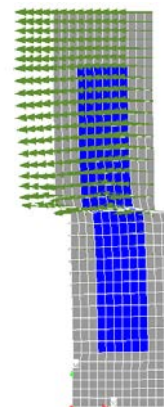


Figure 3 Display vector of Displacement.

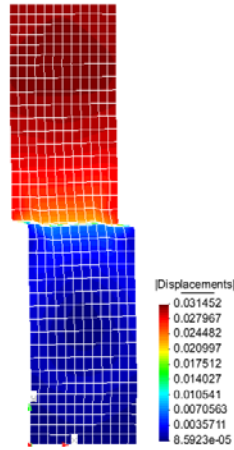


Figure 4 Contour fill of Displacements.

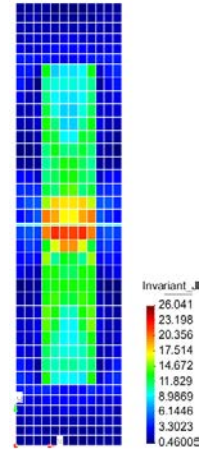


Figure 5 Contour fill of Invariant_J.

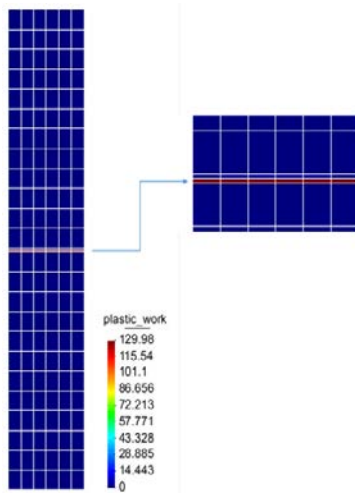


Figure 6 Contour fill of Plastic work.

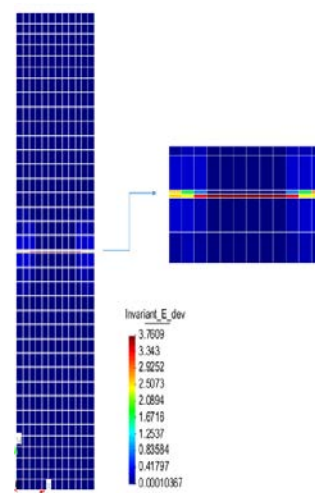


Figure 7 Contour fill of Invariant_E.

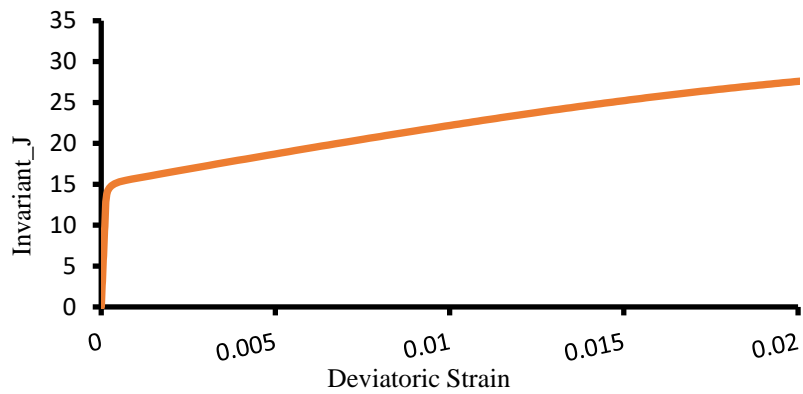


Figure 8 Invariant_J-Deviatoric strain curve.

6. REFERENCE

1. Sierakowski. R. L.(1997). "Strain rate behavior of metals and composites", Civil and Environmental Engineering and Geodetic Science The Ohio State University, Columbus, Ohio USA.
2. Bodner. S.R, Merzer. A.(1978). "Viscoplastic constitutive equations for copper with strain rate History and temperature Effects", Faculty of Mechanical Engineering, Technion - Israel Institute of Technology, Haifa, Israel.
3. Rajendran. A. M, Grove. D. J.(1987). "Bodner-Partom viscoplastic model in Stealth finite difference code", University of Dayton Research Institute 300 College Park Dayton, OH 45469.
4. Börgesson L. (1986). Model shear tests of canisters with smectite clay envelopes in deposition holes. SKB TR 86-26, Svensk Kärnbränslehantering AB.
5. Rubin. M.B, Bodner. S.R.(1995). An incremental elastic-viscoplastic theory indicating a reduced modulus for non-proportional buckling, International journal of solids and structures, 32(20): 2967-2987.
6. Sansour. C, Kollmann. F.G.(1998). Large viscoplastic deformations of shells. Theory and finite formulation. Computational Mechanics, 21(6): 512-525.
7. Hart. T, Schwan. S, Lehn. J, Kollmann. F.G.(1995). Identification of material parameters for inelastic constitutive models including damage. Computational Mechanics, 16(5): 315-327.
8. Klosowski. P, Woznica. K.(2004). Numerical treatment of elasto viscoplastic shells in the range of moderate and large rotations. Computational Mechanics, 34: 194-212.
9. Klosowski. P, Zagubien. A, Woznica K.(2004). Investigation on rheological properties of technical fabric Panama. Archives of Applied Mechanics, 73(9-10): 661-681.
10. Perzyna. P.(1996). Fundamental problems in viscoplasticity. Advances in Mechanics, 9:243-377.
11. Johnson. G.R, Cook. W.H.(1983). A constitutive model and data for metals subjected to large strains, high strain rates and high temperatures. 7th International Symposium on Ballistics, The Hague, pp. 541-547.
12. Zerilli. F.J, Armstrong R.W.(1997). Dislocation-mechanics-based constitutive relations for material dynamics calculations. Journal of Applied Physics, 61(5): 1816-1825.
13. Khan. A.S, Huang. S.(1992). Experimental and theoretical study of mechanical behaviour of 1100 aluminum in the strain rate range 10^{-5} - 10^4 s⁻¹. International Journal of plasticity, 8: 397-424.
14. Jiang. L, Wang. H, Liaw. P.K, Brooks. C.R, Klarstrom. D.L.(2004). Temperature evolution during low-cycle fatigue of ULTIMET alloy: experimental and modeling. Mechanics of materials, 36: 73-84.
15. Skipor. A.F, Harren. S.V.(1998). Thermal cycling of temperature and strain rate dependent solder joints. Mechanics of Time-Dependent Material, 2: 59-83.
16. Rubin. M.B.(1989). A time integration procedure for plastic deformation in elastic-viscoplastic metals. Zeitschrift für Angewandte Mathematik und Physik (ZAMP), 40(6): 846-871.
17. Sung. J.C, Achenbach J.D.(1990). Heating at a propagating crack tip in a viscoplastic material. International Journal of Fracture, 44(4): 301-309.
18. Foringer. M.A, Robertson D.D, Mall. S.(1997). A micromechanics-based approach to fatigue life modeling of titanium-matrix composites. Composites Part B, 28B: 507-521.
19. Arya. V.K.(1996). Efficient and accurate explicit integration algorithm with application to viscoplastic models. International Journal for Numerical Methods in Engineering, 39(2): 261-279.
20. Freed. A.D, Virrilli M.J.(1988). A viscoplastic theory applied to copper. Proceeding of the MECAMAT, Besançon, Vol. I, pp. 27-39.
21. Hackenberg. H.P.(1995). Large deformation finite element analysis with inelastic constitutive models including damage. Computational Mechanics, 16(5): 315-327.
22. Sansour. C, Kollmann. F.G.(2001). On theory and numerics of large viscoplastic deformation. Computer Methods in Applied Mechanics and Engineering, 191: 423-450.
23. Barta. R.C, Jaber. N.A, Malsbury. M.E.(2003). Analysis of failure model in an impact loaded thermoviscoplastic prenotched plate. International Journal of plasticity, 19: 139-196.

24. Esat. I.I, Bahai H, Shati F.K.(1999). Finite element modelling of anisotropic elastic-viscoplastic behaviour of metals. *Finite elements in Analysis and Design*, 32: 279-287.
25. Olivella. S, Gens, A., Carrera, J. EE Alonso. (1996). "Numerical formulation for a simulator (CODE_BRIGHT) for the coupled analysis of saline media", Polytechnic University of Catalonia (University in Barcelona, Spain).
26. Olivella, S., Gens, A., Carrera, J. and Alonso, E.E. (1994). "A model for coupled deformation and nonisothermal multiphase flow through saline media", First International Congress in Environmental Geotechnics, Edmonton, pp. 895-900.
27. Olivella, S., Carrera, J., Gens, A. and Alonso, E.E. (1994). "Non-isothermal multiphase flow of brine and gas through saline media", *Transport in Porous Media*, Vol. 15, pp. 271-93.
28. Olivella, S. (1995). "Nonisothermal multiphase flow of brine and gas through saline media", Doctoral thesis, Departamento de Ingeniería del Terreno, UPC, Barcelona.

HEAT DISSIPATION IN ROCK AROUND CAVERNS FOR HEAVY OIL STORAGE

X. Pintado*

* Saanio & Riekkola Oy; Laulukuja 4, 00420 Helsinki, Finland
Email: xavier.pintado@btech.fi

Key words: Heavy oil, thermal conductivity, specific heat, dissipation.

Abstract. *FORTUM Energy and Power Oy is the owner of four caverns with a capacity of 100 000 m³ each one for heavy oil storage. This fluid should be kept at 55°C in order to be able to be pumped. These caverns are located in Inkoo (South of Finland). For keeping the temperature at 55°C, it is necessary to supply heat. The dimensioning of the heat supply was performed in 3-D taking into account the shape of the surface and the exact positions of the caverns. Only the energy balance equation was solved and the heavy oil was not simulated. The results indicate that the heating process is slow enough for assuring the null influence of the boundaries position in the results. The heavy oil was not simulated due to CODE_BRIGHT does not solve the Navier-Stokes equations (Darcy's law is just a particular case of the Navier-Stokes equations and cannot be used for the simulation of a fluid), but the results indicated that it is not necessary to consider the properties of the fluid into the caverns in a first approximation of the heat supply design.*

1 INTRODUCTION

The storage of hydrocarbons like heavy oil is necessary for assuring the continuous supply of these important products in developed societies. These products are stored in large tanks on the surface or in caverns, near the coast. The underground facilities present some advantages in countries with cold weather like Finland because the heavy oil should be stored at 55°C in order to be able to be pumped. If the heavy oil is stored at certain depth, the rock can contribute to insulate the heavy oil due to its relatively low thermal conductivity but it is necessary to supply heat for keeping this temperature because of the lower temperature of the rock, which is approximately the average temperature at the surface. The geothermal gradient has negligible effects at the first tens of meters (it is around 1.4 °C/100 m in western coast of Finland^[1]).

Heavy oil has a density of 995 kg/m³, a heat capacity of 2 kJ/(kgK) and a thermal conductivity of 0.13 W/(mK). This thermal conductivity is very low. As examples, water has a thermal conductivity of 0.6 W/(mK), a saturated clay around 1.3 W/(mK), a rock, as it will be seen later, around 3 W/(mK) but metals have larger thermal conductivities, like cast iron, 36 W/(mK), or copper, 390 W/(mK). This means that the heat transport into the fluid will be mainly by convection, not by conduction, so the equations taking into account the movement of the fluid (Navier-Stokes equations) should be solved if the heavy oil is taken into account in the calculation.

The parameters of rock were the same parameters used for the design of the spent nuclear fuel repository in Olkiluoto (Finland):

- Thermal conductivity: 2.82 W/(mK) ^[2]
- Specific heat: 764 kJ/(kgK) ^[2]
- Density: 2743 kg/m³ ^[2]

The caverns are emplaced in coastal area of Inkoo, near of Helsinki, the capital of Finland. There is a coal stack pile of coal up 16 m asl (above sea level). The rest of the coastal area has been considered at 2.5 m asl. The bottom part of the caverns is at -46.5 m asl

2 SIMULATION DESCRIPTION

The caverns were simulated into a rock box with dimensions of 1234x1038x146.5 m (the last magnitude is not the same in all geometry because there are three levels: sea level, port facilities and stack pile coal, Figure 1).

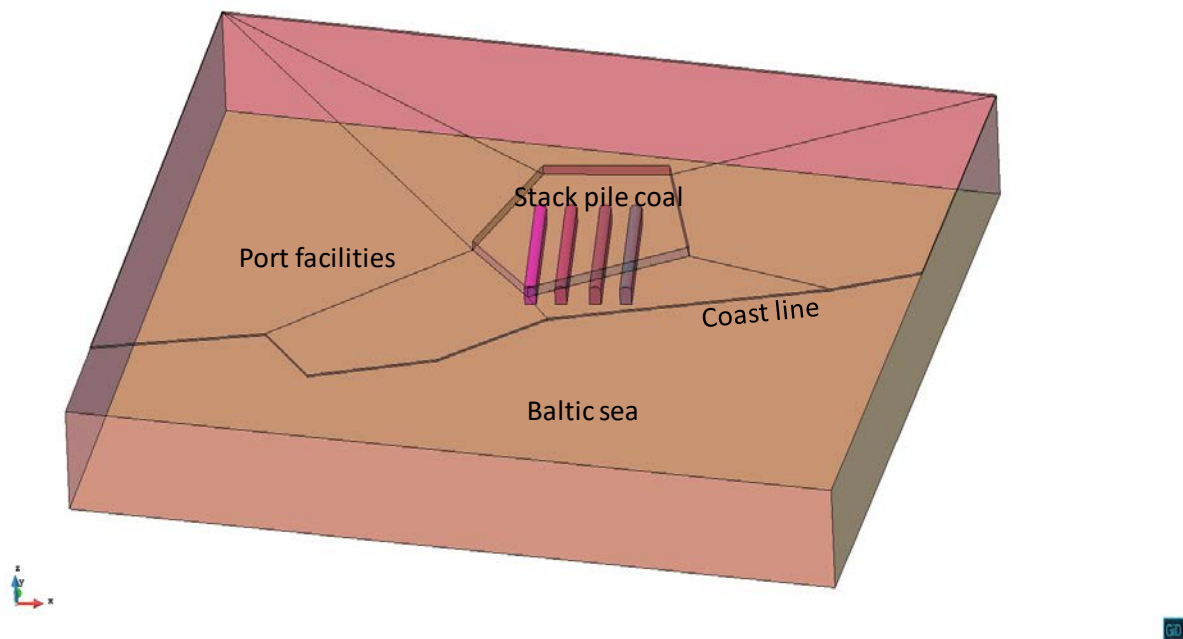


Figure 1. Geometry of the oil tanks and rock.

The temperature in cavern walls was fixed at 55°C. The temperature at the surface was fixed in 5.9°C and it was considered constant (no seasonal changes). The temperature at the bottom of the model was fixed at 7.95°C, following the thermal gradient. The influence of the position of the boundaries and the boundary condition was analysed in a sensitivity analysis, which has proof that the boundaries were far enough from the caverns. The initial temperature follows the thermal gradient in depth starting with the temperature at the surface. The mesh had 606 736 nodes and 3 767 175 linear tetrahedron elements (Figure 2). Mesh around caverns was denser, specially between them.

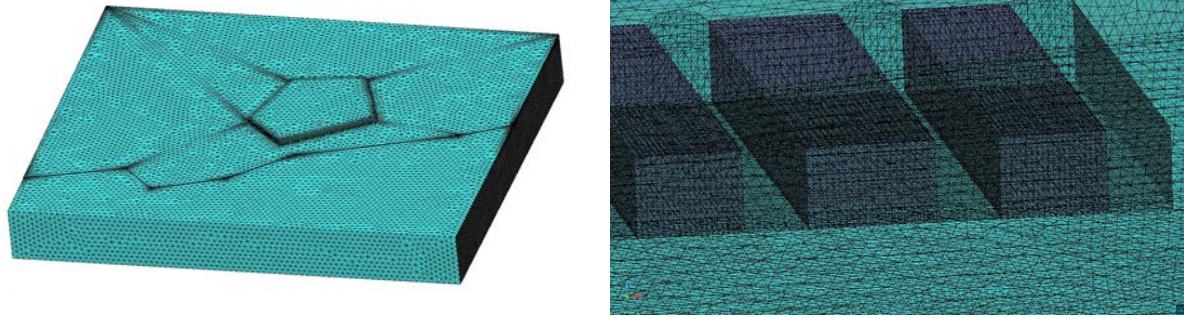


Figure 2. Mesh and detailed mesh around the caverns. The rock between caverns was especially dense for avoiding mesh dependency.

3 RESULTS

The results are presented in Table 1. The power needed for keeping the temperature at 55°C at the four tanks was calculated in some intervals of time and the average for each step is presented. As it was expected, the amount of heat necessary is going down due to the heating of the rock.

Table 1. Power necessary (kW) for different time intervals and for the four caverns.

Period (months)	Power (kW). Four caverns
1-3	2625
3-12	1700
12-24	1120
24-60	810

The distance to the boundaries and the boundary conditions were also checked:

- Fixed temperature at the surface equal to 5.9°C and fixed temperature at the bottom equal to 7.95°C. No heat flow on lateral surfaces. Thermal dimensioning has been done with the results of this case. (Case 9b).
- No heat flow in any surface (Case 9d).
- Fixed temperature at the surface equal to 5.9°C and no heat flow at the rest of the surfaces (Case 9e).
- Fixed temperature at the surface equal to 5.9°C and fixed temperature at the bottom equal to 7.95°C. The lateral temperature is fixed as function of the distance to the surface following the geothermal gradient (Case 9g).
- The temperature in walls increases linearly during the first month (Case 9h).

The results proof that the boundary conditions do not have influence on the results except when the domain is insulated (as it can be expected) and the difference can be seen only after some years. The heat basically increases the temperature of rock and after some time, it escapes mainly through the surface. Figure 3 shows the heat supply.

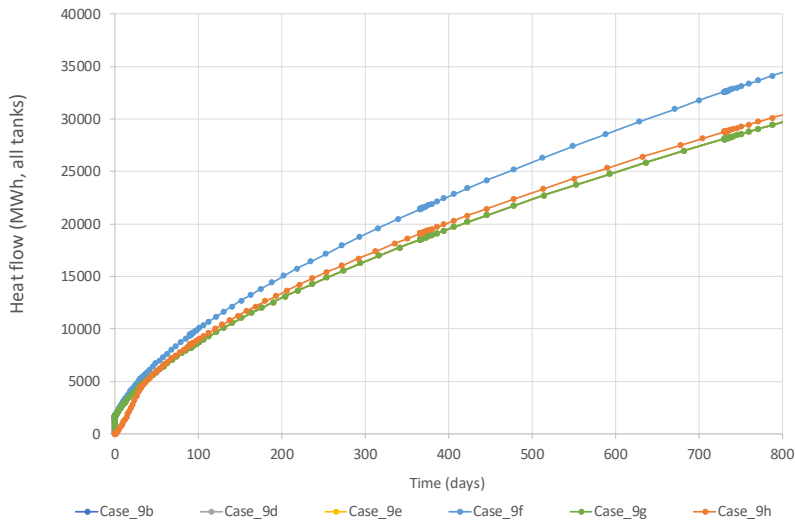


Figure 3. Heat supply. All tanks.

The heat injection at the beginning should not be taken into account due to the non-realistic high amount of heat necessary for keeping the temperature of walls at 55°C. The mass of oil will supply heat and recover the temperature quite fast. This analysis cannot be done solving only the heat transport equation due to the heat transport through the heavy oil will be mainly by convection. Figure 4 shows the power necessary. The scale is logarithmic and the first day is not showed due to the unrealistic heat supply for keeping the temperature at 55°C in walls (the model increases it suddenly). If the temperature increment is during the first 30 days, the power needed is smoother at the beginning.

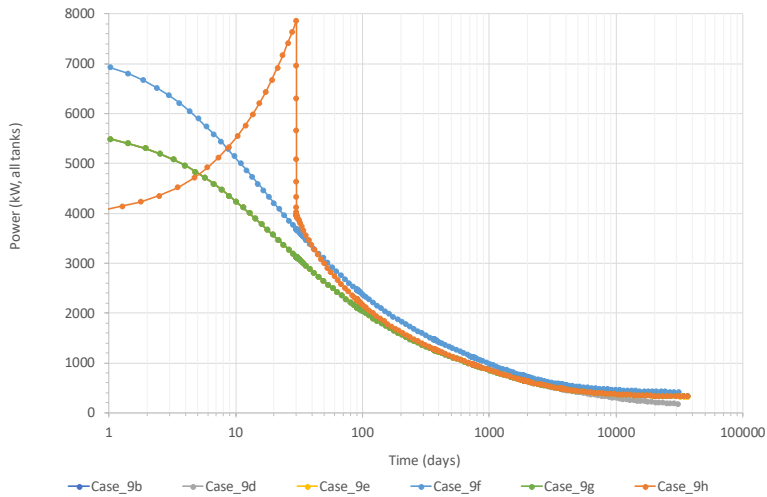


Figure 4: Power needed for keeping the temperature at 55°C at the four tanks in tanks walls.

Two cases were run taking into account the presence of heavy oil in tanks but solving only the energy balance equation. Heavy oil thermal conductivity in one case is 0.13 W/(mK) and in the second case, the thermal conductivity is quite large (larger than copper). In this second case, it is assumed that the fluid moves fast enough for keeping the same temperature in all fluid. The reason for running these cases was just to check the average temperature of the four tanks

evolution (Figure 5) and not to study the temperature distribution inside the tanks. This should be done with a Computer Fluid Dynamics (CFD) software and it is out of the scope of this work.

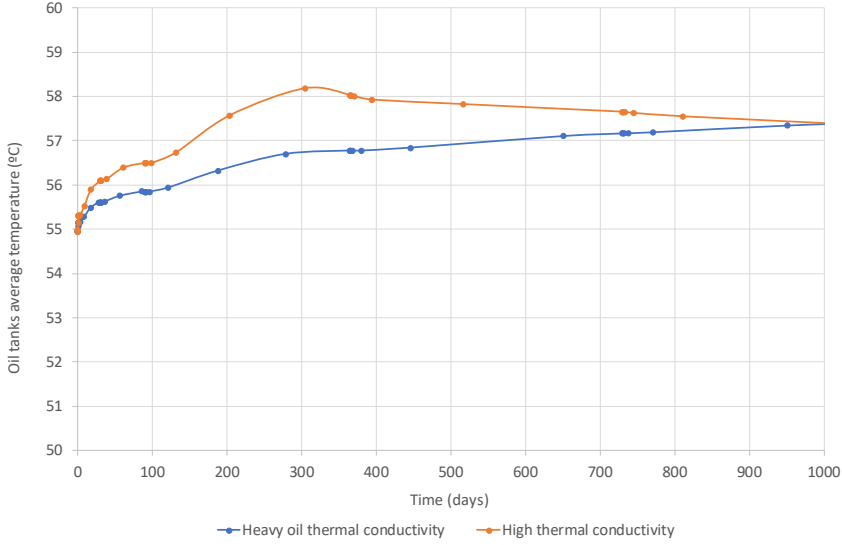


Figure 5. Average temperature in heavy oil.

The temperature distribution after 90 days and two years in central section of the oil caverns can be seen in Figure 6. It is possible to see that the heat wave is still quite far from the boundaries and the heating process is controlled by the thermal properties of the rock and its initial temperature.

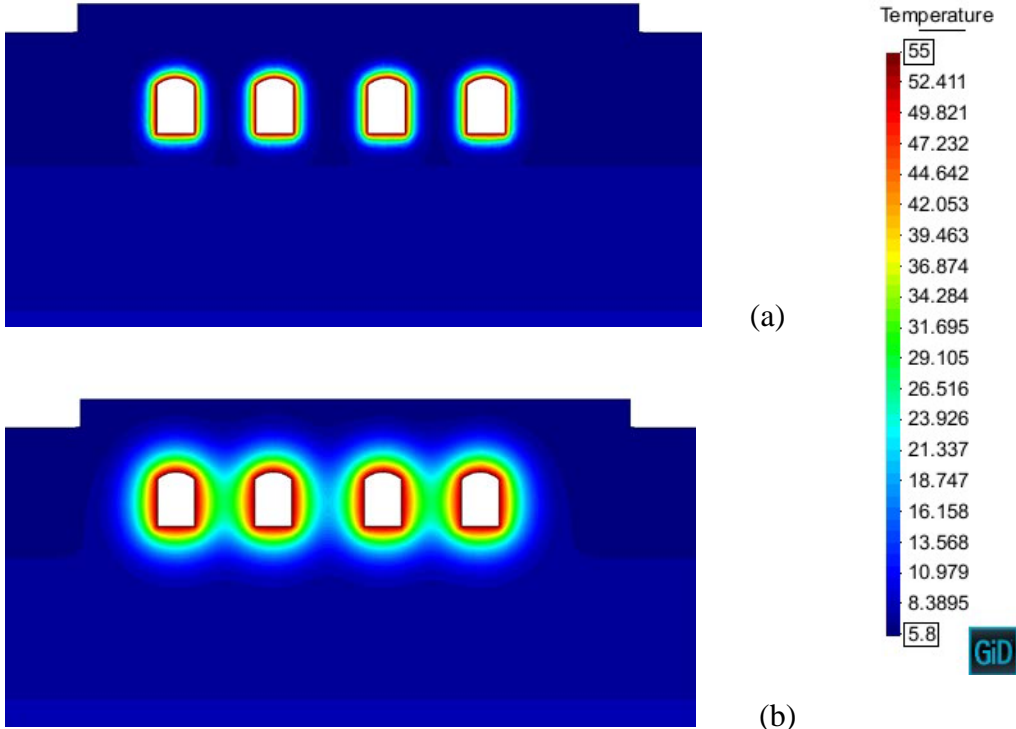


Figure 5. Temperature distribution after 90 days (a) and two years (b).

4 CONCLUSIONS

- The thermal analysis is enough for the calculation of the power supply for keeping the temperature of the caverns at 55°C.
- The heat supply for keeping the temperature in walls at 55°C at the early stage (firsts days) is extremely high and cannot be studied (although it was calculated). At this early stage, the heat accumulated in the mass of heavy oil will play certain role but as it has been said before, the behavior of the heavy oil cannot be analysed with CODE_BRIGHT (the Navier-Stokes equations should be solved).
- The domain is large enough for avoiding the effect of the boundaries.

ACKNOWLEDGEMENTS

This work was supported by FORTUM Energy and Power Oy. The author acknowledges Henry Sammalniemi for his technical and administrative assistance.

REFERENCES

-
- ^[1] Sedighi, M., Bennett, D., Masum, S.A., Thomas, H.R., Johansson, E. (2014). Analysis of temperature data at the Olkiluoto. Posiva working report 2013-58. Eurajoki, Finland.
- ^[2] Kukkonen, I., Kivekäs, L., Vuoriainen, S., Kääriä, M. (2011). Thermal properties of rocks in Olkiluoto: Results of laboratory measurements 1994-2010. Posiva working report 2011-17. Eurajoki, Finland.

LOESS SLOPE INSTABILITY UNDER ATMOSPHERIC BOUNDARY CONDITION

Lingyun Li*, Maria Datcheva *† and Wiebke.Baille*

* Ruhr-Universität Bochum, Department of Civil and Environmental Engineering,
Universitätsstr. 150, 44780 Bochum, Germany

† Bulgarian Academy of Sciences, Institute of Mechanics,
Acad. G. Bonchev St., bl. 4, 1113 Sofia, Bulgaria
Email: Maria.Datcheva@ruhr-uni-bochum.de

Key words: Slope, Atmospheric boundary condition, BBM, Collapsible loess.

Abstract. *Baqiao slope suffered a landslide in 2011 in northwest China. Code_Bright was used to analyse the behaviour of the slope during various atmospheric boundary conditions with the aim of simulating displacements, total stresses and pore water pressures. To represent the mechanical behaviour of collapsible loess, Barcelona Basic Model has been considered. The parameters of the mechanical and hydraulic model have been determined from the laboratory tests. The final simulated plastic region will be compared with the real landslide mass. A detailed analysis was performed to understand the process failure of rainfall induced landslide. It was concluded that coupled thermo-hydro-mechanical (THM) simulation combined atmospheric boundary condition can better predict the instability deformation of slope, compared with simplistic model.*

1 INTRODUCTION

The continuous rainfall since September 4 made Shaanxi at 2:10 pm on September 17, a landslide on the northern slope in Baqiao, a suburban district of Xi'an, northwest China's Shaanxi Province. From 10 a.m. to 11 p.m. on September 18, three consecutive landslides occurred again, that buried a residential house. As of 5:30 p.m., Saturday's landslide at about 2 pm unleashed about 100,000 cubic meters of rock and mud down the mountain. However, there were three follow-up slides between 10 a.m. and 11 am Sunday as heavy rains continued slashing the city. About 10,000 cubic meters of newly-triggered rock and mud roared down to the site. The sliding mass is mainly constituted of loess, figure 1 shows the picture of landslide in the field. Due to the permeability of loess material, once precipitation would just have small influence on the upper surface layer, it is seasonal to consider accumulated precipitation events effect on the slope stability, evaporation capacity in September is also among the largest evaporated period in the whole year.

The Baqiao landslide happened area, the Bailu tableland, is formed by loess deposits which covers an area of 238 km² with steep edges. The average slope gradients of the tableland in the

southeast section of the study area ranges between 35 and 55°, with isolated slopes of steeper than 55°. It is located 5 km southeast from Xi'an city. The strata of Baqiao slope is primarily Quaternary strata which covers the entire area of the Malan and Lishiⁱ, which deposited in Late Pleistocene and Middle Pleistocene, separately. The geometry and stratigraphic information of Baqiao slope are taken from the characteristic of this area. A rough sketch of slope is created in simulation depends on the real measurement.

Loess has a relatively loose texture, metastability strength characteristics, collapsibility, and unique jointing structure, which make it instability under influx conditionⁱⁱ. The material makes up of this slope is aeolian deposit loess. Loess sample were extensively analysed by laboratory tests on intact block samples taken from same region. Experiments such as infiltration, water retention, shear tests and oedometer tests were carried out on saturated and unsaturated samples in laboratory to get the knowledge of geotechnical profile, a relationship between elastic plastic behaviour and matric suction was established. Some parameter values which are unavailable got from laboratory were collected from literatures. In addition, initial condition such as initial porosity and matric suction of slope simulation is based on assumption. CODE_BRIGTH combined Barcelona basic model has been widely used to simulated collapsible soilⁱⁱⁱ. Tremendous tests have been taken to validate Barcelona basic model representing collapse behaviour^{iv}.



Figure 1: Baqiao landslide on 11 September, 2011

2 DESCRIPTION OF NUMERICAL MODEL

The representative section of Baqiao slope is shown in Figure 2. Depending on the geology strata, the slope is constituted by three layers. Bottom layer is Q1 loess. The middle is Q2 loess and the upper layer is Q3. From Q1 to Q3, the strength and stiffness become less, the potential collapse and permeability become more. In order to take into accounting the features of the

upper layer, Q3 loess is characterized by means of the BBM model. An elastic and plastic compressibility for saturated states should be included in the model. The Q1 is set as linear elastic plastic (Mohr-Coulomb model) material.

The evolution of deformation and liquid pressure under variables as stress was modelled using the elastic-plastic constitutive laws for Q3 and Q2 loess materials. The coupled hydro mechanical problem is calculated under the boundary conditions variable with time (rain, temperature, relative humidity) are imposed on slope surface. A coupled thermal multiphase flow was developed to study mass and energy transfer in slope. The atmospheric boundary condition is got from the field measurement data.

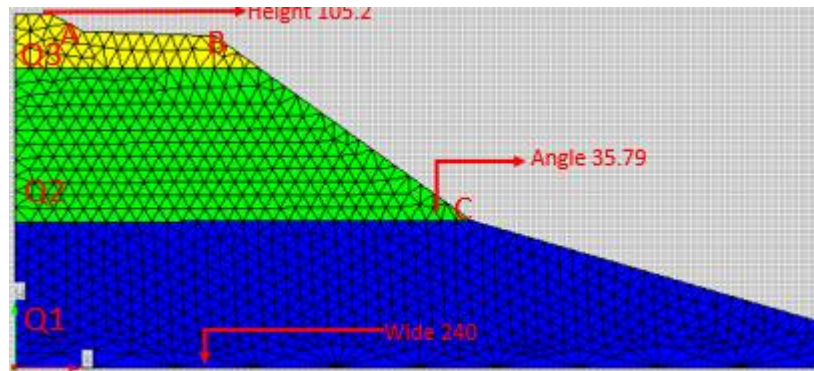


Figure 2: Used materials and performed test for material characterization

Laboratory devices which are showed in Figure 3, were conducted to the parameter values, such as compressibility, initial pre consolidation stress under various matric suction (corresponding to the LC in BBM). The main feature of collapsible soil is that it can develop large deformation under suction reduced process. The initial apparent pre consolidation stress determines the elastic domain, which is determined by the combination of net mean stress and matric suction. The higher the suction, the larger the elastic domain and compressibility^v.

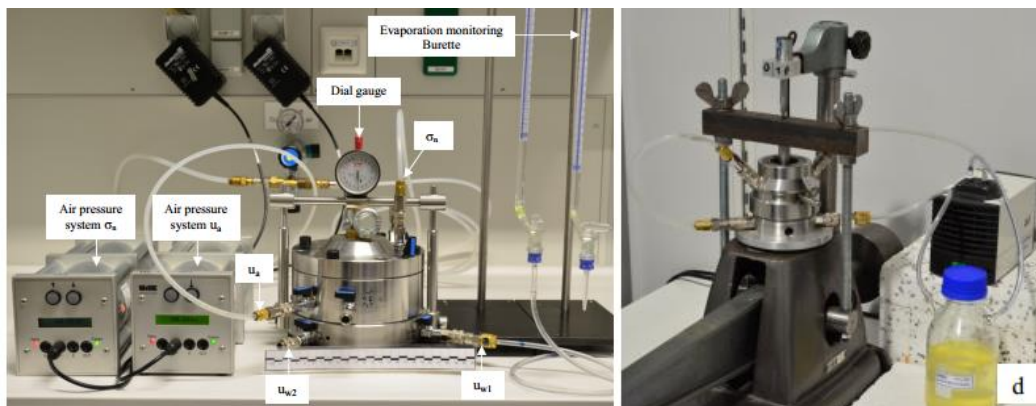


Figure 3: UPC-Barcelona cell with ATT technique modified UPC-Isochoric-Oedometer cell with VET technique^{vi}

3 RESULTS

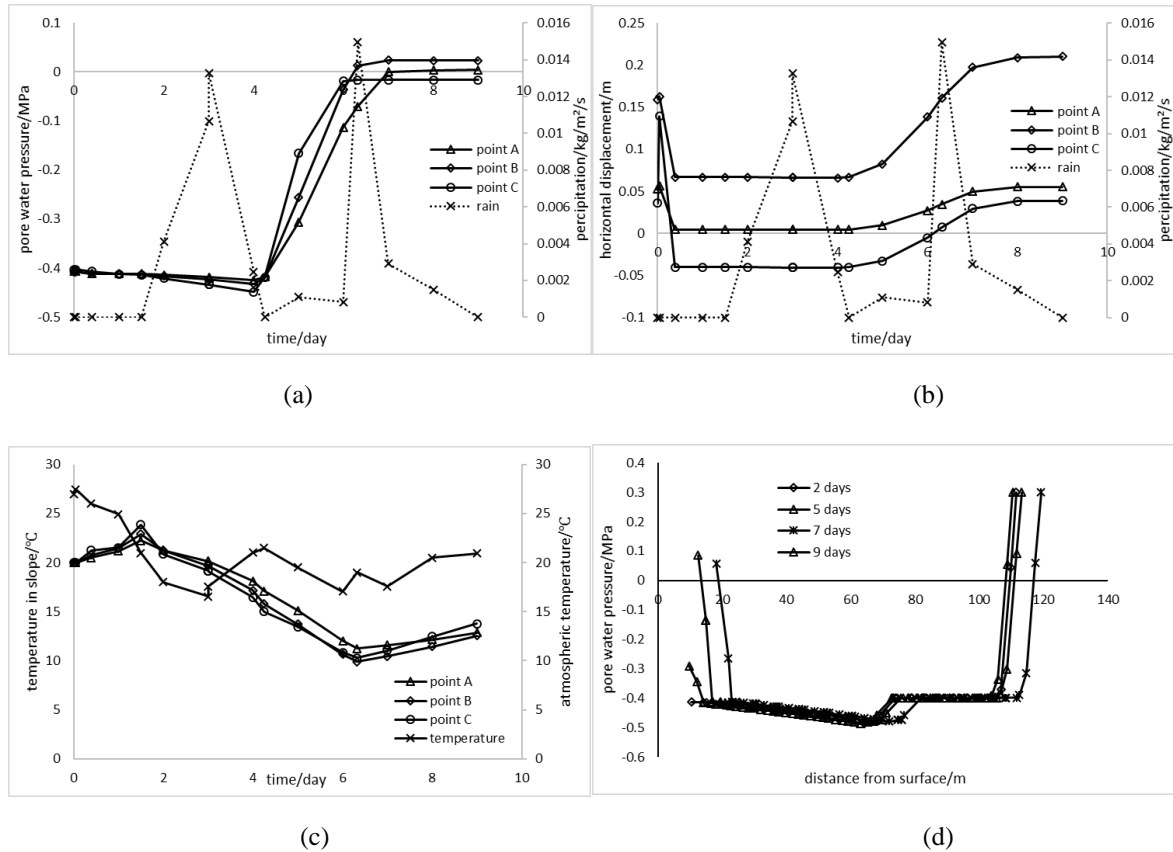


Figure 4: (a) pore water pressure versus time (b) horizontal displacement versus time (c) temperature versus time (d) pore water distribution along slope in section A

The evolution of liquid pressure in position A, B, C are showed in figures 4a, which represent the liquid pressure is greatly dependent on the hydraulic boundary conditions. In non-precipitation days, there is gentle increase of matric suction on the surface, while in rainfall days, the pore water pressure increase sharply. The final liquid pressure in slope is independent of the initial degree of saturation once the material gets fully saturation during the calculation process. Figure 4(d) indicates the phreatic line is controlled by the rainfall duration. The phreatic line moves downwards after long duration of rainfall. Despite the rainfall, there is always an unsaturated zone, where liquid pressure remains less than 0. From the results, we can see that the Q1 layer and the groundwater table are not influenced by the atmospheric boundary conditions. In CODE_BRIGHT surface runoff can be considered when liquid pressure larger

than gas pressure, but no ponding is simulated, which means there is no storage of water and excess infiltration is runoff. Some delayed phenomenon can be seen from the results, which means for low permeability material, it takes time for phreatic line to move deeper.

Figure 4(b) shows horizontal displacement of soil in A, B, C positions. In this case horizontal and vertical permeability are considered to be equal. Evaporation phenomenon happened when the atmospheric relative humidity larger than that of material, which makes capillary rise inside the soil, tension stress developed under evaporation process. The horizontal displacement under evaporation process is comparatively less than the value under precipitation process. Evaporation and precipitation produced by temperature and relative humidity gradients caused by atmospheric boundary fluctuations outside. The temperature variation caused by atmospheric boundary condition is more sensitive, compared with liquid pressure and displacement. After thermal equilibrium between outside and material, they seem change simultaneously in same trend.

4 CONCLUSIONS

2D numerical models have been developed for a qualitative and partial quantitative understanding of the processes that causes Baijiao slope instability under atmospheric conditions. The properties of the materials are emphasized, for which Barcelona basic model is chosen for simulation. Model parameters based on laboratory tests is applied in numerical model. The model boundary condition considers evaporation processes, due to temperature and relative humidity gradients, and precipitation processes. It leads to significant variations of liquid pressure and deformation over time. The sliding surface and the scale of sliding mass after simulation will be compared with field measurement in the further work. Parameter analysis on the initial condition values could also been taken.

REFERENCES

- [i] Zhuang, J. Q., & Peng, J. B. (2014). A coupled slope cutting—a prolonged rainfall-induced loess landslide: a 17 October 2011 case study. *Bulletin of Engineering Geology and the Environment*, 73(4), 997-1011.
- [ii] Derbyshire E, Dijkstra TA, Smalley IJ, Li Y (1994) Failure mechanisms in loess and the effects of moisture content changes on remolded strength. *Quatern Int* 24:5–15
- [iii] Costa, L. M., Pontes, I. D. S., Guimarães, L. J. N., & Ferreira, S. R. M. (2008). Numerical modelling of hydro-mechanical behaviour of collapsible soils. *International Journal for Numerical Methods in Biomedical Engineering*, 24(12), 1839-1852.
- [iv] Cui, Y. J., & Delage, P. (1996). Yielding and plastic behaviour of an unsaturated compacted silt. *Géotechnique*, 46(2), 291-311.

[v] Alonso, E. E.; Gens, A.; Josa A. (1990). A constitutive model for partially saturated soils. *Géotechnique*. 40(3):405–30.

[vi] Al-Obaidi, Q. A. J. (2015). Hydro-mechanical behaviour of collapsible soils. Ruhr-Universität Bochum, Department of Civil and Environmental Engineering, Bochum, Germany

WATER AND HEAT FLUXES IN EMBANKMENTS UNDER CLIMATIC ACTIONS. MODELLING OF A CASE STUDY

V. Guachizaca*, C. Villarraga*, J. Vauna*t, A. Lloret*, M. Saaltink*,
R. Oorthuis*, M. Hürlimann*

* Division of Geotechnical Engineering and Geosciences, Department of Civil and Environmental Engineering, Technical University of Catalonia (UPC)
Campus Nord UPC, 08034 Barcelona, Spain
E-mail: code.bright@upc.edu, web page: www.etcg.upc.edu/recerca/webs/code_bright/

Key words: T-H coupled analysis, Soil-atmosphere interaction, Embankment.

Abstract. *SMuCPHy is a multidisciplinary project along the Challenge line “Action on climate change and efficiency in the use of resources and raw materials” with special attention on the investigation of geological-geotechnical hazards under Climate Change and related adaptation strategies. This work presents the monitoring of a full-scale embankment with different slope orientations (North and South) and vegetation covers (bare and vegetated) built in the ParcUPC Agròpolis with materials proceeding from the Llobregat river delta. The soil-atmosphere interaction is studied with the monitoring of several variables at different vertical profiles such as: soil and air temperature, relative humidity, barometric pressure, heat flow, pore water pressure, volumetric water content and solar radiation. The monitored data will improve the understanding of the soil-atmosphere interactions and provide essential input data for numerical modelling of the coupled thermo-hydro-mechanical processes in geological media. In the present work a numerical model carried out with the finite element Code_Bright software is proposed. It couples the thermal and hydraulic processes to understand the interaction between soil and atmosphere at the non-vegetated slopes. The results obtained with the model, comparing with the in-situ measurements of temperature and volumetric water content at -1 and -16cm depth, are similar, especially at the northern slope from July 2017 till February 2018. The retention curve hysteresis effect obtained from the monitored data, the effect of vegetation and the mechanical coupling will be studied in the future to implement the model.*

1 INTRODUCTION

Climatic changes will induce variations on the hydric and thermal state of the geo-structures, which will lead to slope mass-wasting like shallow slides or other erosional processes. Climate effects such as rainfall and the soil-vegetation-atmosphere (SVA) interactions play a key role and should be studied in order to mitigate the risk of erosion¹. The understandings of the soil-vegetation-atmosphere interactions is fundamental for the correct assessment of rainfall-induced slides and other slope mass-wasting processes². In this summary we present a full-scale embankment with different orientations (North and South) and vegetation covers (bare and vegetated) in order to study the interactions between soil an

atmosphere considering a thermo-hydro formulation model, focusing on the bare slopes. The results will provide essential data for a better understanding of the infiltration process and the influence of the atmosphere to predict the engineering behavior of earth materials and the stability of natural and man-made slopes.

2 DESCRIPTION OF THE FULL-SCALE EXPERIMENT

2.1 General aspects

The embankment measures 18 m long, 12 m wide and 2.5 m height, which incorporates a total volume of about 326 m³ (Figure 1). It was constructed at the end of 2016 at ParcUPC Agròpolis, located on the deltaic floodplain of the Llobregat River. The slopes are built at 33.7 degree corresponding to 3H : 2V. The construction phases included three steps: first, the core was built; then an irregular, studded structured and impermeable polyethylene geomembrane was laid out; and, finally, a 50 - 70 cm thick soil layer was accumulated on the geomembrane. A shallow soil layer on an impermeable bedrock is a very common condition in many mountainous areas including the Pyrenees or the Catalan Coastal Ranges, where multiple slope rainfall-induced failures have occurred in the past^{3,4,5}.

The surficial soil layer includes four monitored slope partitions, which are laterally separated by the geomembrane: a vegetated and a bare slope at the South side of the embankment and another two partitions with and without vegetation at the North-facing slope. This set-up provide information on the effect of orientation (solar radiation) and of vegetation, two fundamental aspects in the evaluation of the influence of future changes on slope mass-wasting.

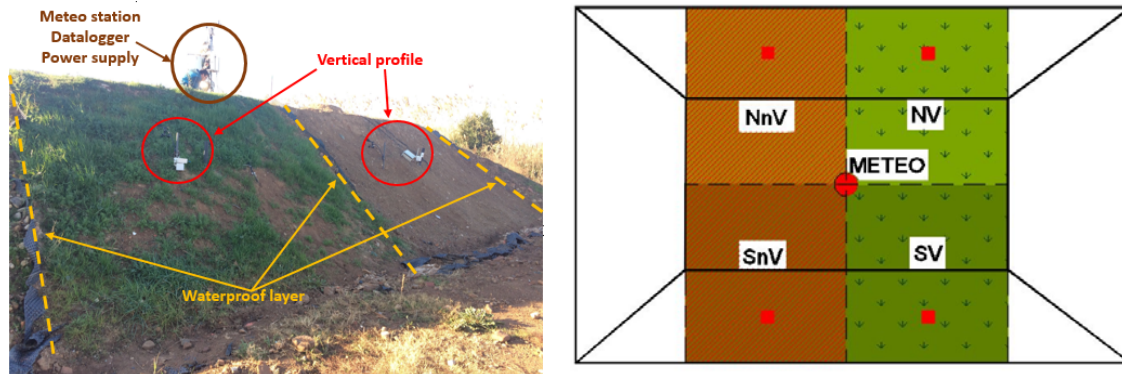


Figure 1. (a) Photograph of the embankment after installation of the sensors looking towards the North slope; (b) Schematic overview of the full-scale experiment divided into four partitions: SV, SnV, NV and NnV (see text for explanations). The position of the four vertical sensor profiles (red squares) and the meteorological station (red dot) is illustrated.

Finally, the sensors were installed at vertical infiltration profiles inside the upper soil layer of each of the four partitions. In addition, a meteorological station was fixed at the top of the

embankment. The power supply of the entire monitoring system is given by solar panels and batteries.

As stated above the experiment includes four different zones: i) South slope with vegetation (SV), ii) South slope without vegetation (SnV), iii) North slope with vegetation (NV), ii) North slope without vegetation (NnV). Each of the four zones is equipped by a vertical profile of different sensors (Figure 1b) and the devices that measure the surface runoff and seepage. Thus, a complete analysis of the soil-vegetation-atmosphere interaction is possible incorporating observations gathered by the meteorological station.

2.2 Description of the vertical sensor profiles and meteorological station

Each vertical profile measures air and soil temperature, relative humidity, barometric pressure, heat flux, pore water pressure (PWP) and volumetric water content (VWC) at different positions. A net solar radiation device was installed at each of the orientations (North and South). The general distribution of the different devices is shown by the example of vertical profile NnV (Figure 2a). In addition, photographs of the soil texture format profiles NnV and NV during the sensors installation are shown in Figure 2b and Figure 2c respectively. They show the sandy loamy soil with isolated gravel particles at both trenches, while the presence of organic material in the form of plant roots is visible in the vegetated south (NV) profile.

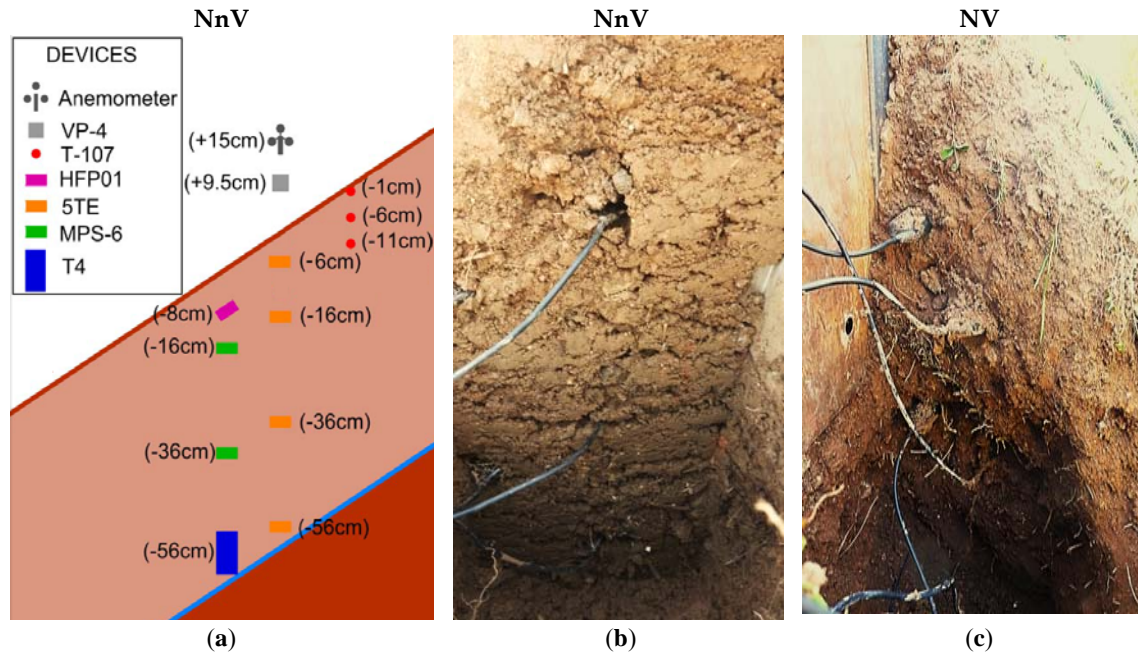


Figure 2. (a) Schematic design of vertical profile NnV indicating the location of the sensors; (b) Photograph taken during installation of sensors at NnV profile; (c) Photograph taken during installation of sensors at NV profile.

3 MODEL

The modelling of the soil-atmosphere interactions has been done with the finite element software Code_Bright⁶. The mechanical interaction has not been implemented and only the hydro-thermal interactions has been considered, using the balance equations of water and heat. The constitutive laws related to this equations are: Heat capacity, phase change, Darcy for flux of water, Fourier for flux of heat, and retention curve⁷.

3.1 Geometry, mesh, initial and boundary conditions

The geometry and the finite element mesh used in the model is shown in Figure 3, corresponding to the North and South non-vegetated slopes. The thickness at the middle of the North and South slope varies between 86 and 72cm respectively, with an average slope of 33°. The thickness of the slope at the upper part is about 41cm. The finite element mesh has a structure of 1254 nodes and 1170 quadrilaterals and has been densified at the slope surface to obtain more accurated results at the soil-atmosphere interaction.

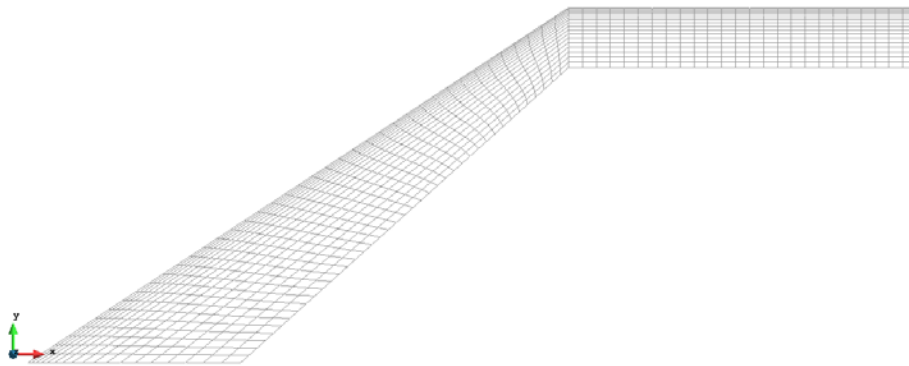


Figure 3. Mesh the finite elements of the north and south slope.

The initial conditions of the model were defined on 11 January 2017 after the embankment construction. The initial moisture content was obtained from in-situ soil samples taken at both slopes. The initial temperature of the slopes was defined according to the air temperature, considering the effect of radiation at each slope.

The boundary condition imposed at the surface of the slope is no-linear and simulates the effects of the atmosphere, where the solar radiation defined as the net radiation is equal to the total radiation less the radiation reflected by the surface of the ground and plus the radiation diffracted by the atmosphere. This condition also includes the environmental temperature, relative humidity and rainfall. The relative humidity and temperature are weighted by an embankment-atmosphere surface coefficient, which includes the wind turbulent effect by the von Karman's law. The internal contour of the slope was defined with a null flow condition simulating the waterproof membrane.

3.2 Retention curve

The retention curve relates the degree of saturation with suction, which is a very important physical property to understand the hydro-mechanical behavior of unsaturated soils. The model considers double porosity and is justified by the presence of fines in the soil (clayey silt) which particles are grouped forming two types of macro and micro structures. The bimodal retention curve was obtained with the Van Genuchten model choosing the parameters that best fit the in-situ measurements related to the VWC and suction recorded at the embankment by the 5TE and MPS-6 sensors respectively. Figure 4 shows the retention curve measured in-situ during the period of one year and the adjustment applying the minimum squares method for both North and South oriented slopes.

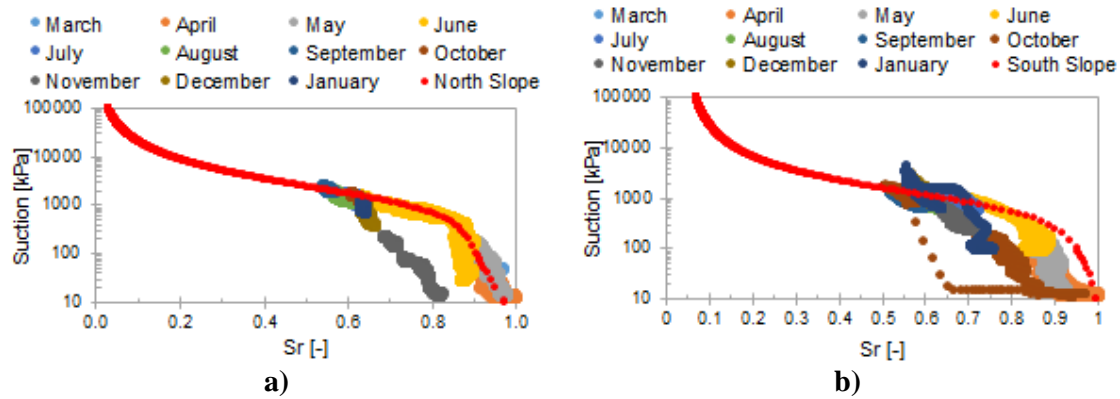
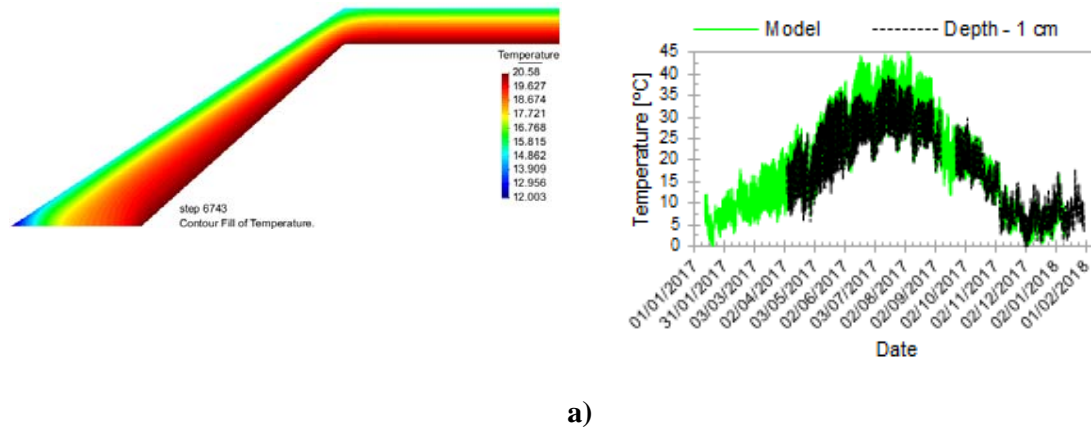


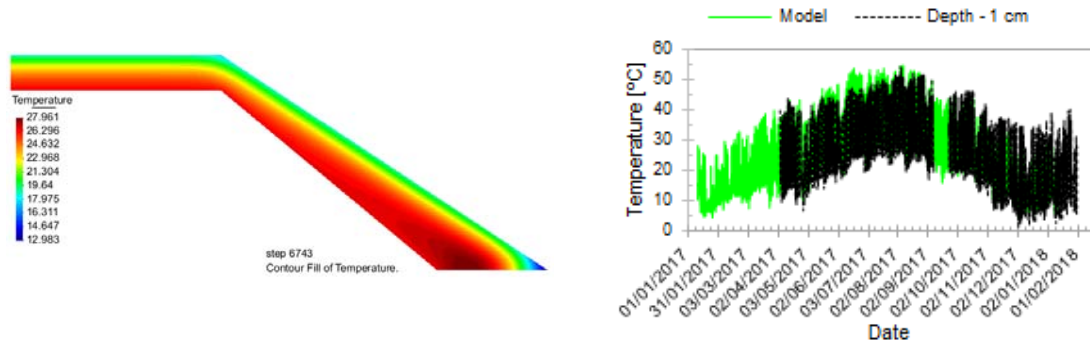
Figure 4. Bimodal water retention curve: a) North Slope; b) South Slope.

4 RESULTS

The results obtained with the thermo-hydro (T-H) coupled modeling regarding temperature and VWC are shown in Figure 5 and Figure 6 respectively. The results correspond to the non-vegetated embankment slopes at the North and South slopes of the experimental embankment.

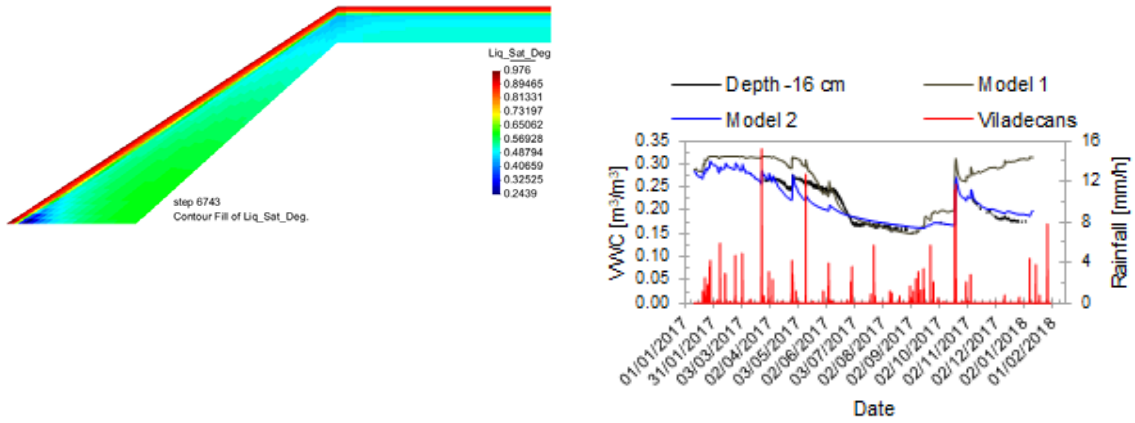


a)

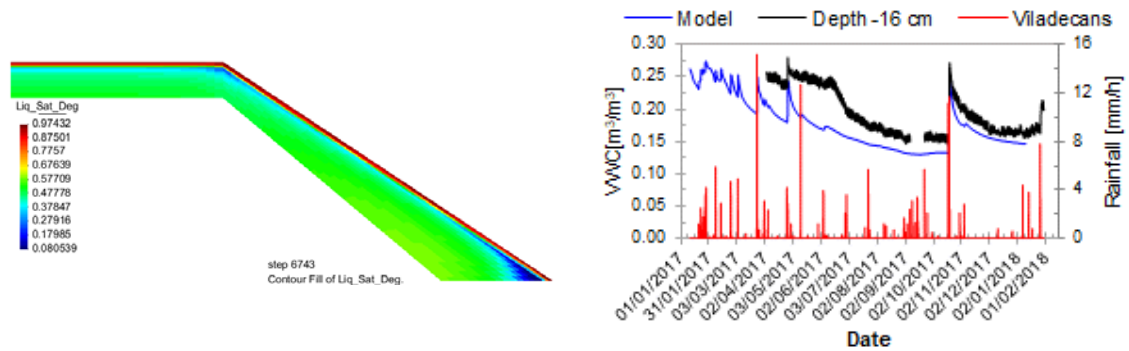


b)

Figure 5. Time-evolution of temperature: a) North Slope; b) South Slope



a)



b)

Figure 6. Time-evolution of volumetric water content: a) North Slope; b) South Slope

The model of the present investigation represents well the variations of temperature at the surface (-1 cm) and follows the seasonal cycles (Figure 5). The effect of daily variations are observed, with higher soil temperature at the surface compared to the air, due to the effect of solar radiation. In addition, the effect of solar radiation is more noticeable at the South slope, with higher temperatures compared to the North-faced slope.

Figure 6 a shows the variations of the North slope VWC at 16cm depth. The state at the start of the measurements was computed by applying the model for a previous period starting at embankment construction. The results obtained by the model during March 2017, when the sensors were installed, are in agreement with the in-situ measurements recorded by the sensors. The mechanical coupling and the hysteresis phenomenon (Figure 4) are not considered. Under these hypotheses, the South slope model results (Figure 6 b) are below the in-situ measurements. In any case higher drying rates are predicted at both slopes.

Another important fact relies on the slope orientation and the incident solar radiation. During the winter months (November-January) the North slope is not affected by direct solar radiation and only diffusive atmospheric radiation takes a role. Diffusive radiation is considered in order to model the VWC changes during these months. Not considering diffusive radiation will lead to an increase in the VWC model, tending to saturation, which is opposite to the observed behaviour.

5 CONCLUSIONS

The model is able to reproduce the in-situ embankment measurements and will allow to apply predictive records based on the climate change to see its effect on geo-structures. The initial conditions were computed by modeling the equilibrium phase with the atmosphere, which gives good results. The VWC are generally well predicted excepted during the first drying period. This maybe due to deformation and hysteresis effects. They will be further studied in the project together with the effect of vegetation.

6 REFERENCES

- [1] Tang, A. M., Hughes, P. N., Dijkstra, T. A., Askarinejad, A., Brenčić, M., Cui, Y. J., ... Van Beek, V., 2018. Atmosphere–vegetation–soil interactions in a climate change context; impact of changing conditions on engineered transport infrastructure slopes in Europe. *Quarterly Journal of Engineering Geology and Hydrogeology*, (March), 2017–2103, <https://doi.org/10.1144/qjegh2017-103>.
- [2] Casini, F., Askarinejad, A., & Springman, S. M., 2016. Infiltration-induced Slope Instability: a multi-scale approach. *E3S Web of Conferences*, 9, 04005, <https://doi.org/10.1051/e3sconf/20160904005>.
- [3] Portilla, M., Chevalier, G., Hürlimann, M., 2010. Description and analysis of the debris flows occurred during 2008 in the Eastern Pyrenees. *Nat. Hazards Earth Syst. Sci.*, 10, 1635–1645, doi:10.5194/nhess-10-1635-2010.
- [4] Corominas, J., Moya, J., 1999. Reconstructing recent landslide activity in relation to rainfall in the Llobregat River basin, Eastern Pyrenees, Spain. *Geomorphology*, 30, 79–93, doi:10.1016/S0169-555X(99)00046-X.

V. Guachizaca*, C. Villarraga*, J. Vauna*t, A. Lloret*, M. Saaltink*,
R. Oorthuis*, M. Hürlimann*

- [5] Gallart, F., Clotet-Perarnau, N., 1988. Some aspects of the geomorphic processes triggered by an extreme rainfall event: the November 1982 flood in the Eastern Pyrenees. *Catena Suppl.*, 13, 79–95.
- [6] Departament d' Enginyeria del Terreny, Cartografia i Geofísica. 2017. "CODE_ BRIGHT User's Guide."
- [7] Gaetano, E., Cotecchia, F., Pedone, G., Vaunat, J., Vardon, P.J., Pereira, C., Springman, Sarah M. et al., 2017. Numerical Modelling of Slope–vegetation–atmosphere Interaction: An Overview. *Quarterly Journal of Engineering Geology and Hydrogeology* 50 (3): 249–70, <https://doi.org/10.1144/qjegh2016-079>.
- [8] Oorthuis, R., Hürlimann, M., Fraccica, A., Lloret, A., Moya, J., Puig-Polo, C., Vaunat, J., 2018. Monitoring of a Full-Scale Embankment Experiment Regarding Soil-Vegetation-Atmosphere Interactions. *Water*.

THREE-DIMENSIONAL SIMULATION OF THE HE-E HEATER EXPERIMENT PERFORMED AT THE MONT TERRI ROCK LABORATORY (SWITZERLAND)

Larissa Friedenberg, **Klaus Wiczorek**, **Oliver Czaikowski**

Gesellschaft für Anlagen- und Reaktorsicherheit (GRS) gGmbH
Theodor-Heuss-Str. 4, 38122 Braunschweig, Germany
email: larissa.friedenberg@grs.de

Key words: claystone, nuclear waste disposal, in-situ experiment

1. INTRODUCTION

For constructing a nuclear waste repository in argillaceous rock and for ensuring that the safety criteria are met over very long time periods, profound knowledge about the material behaviour of the coupled system of waste containers, engineered barriers (EBS), and the host rock is indispensable. Large-scale simulation experiments performed in underground research laboratories contribute to gaining this knowledge. One of these underground research laboratories is the Mont Terri Rock Laboratory (MTRL) which is situated in the canton of Jura near St-Ursanne (Switzerland) in the Opalinus clay rock formation (Mont Terri 2018).

The HE-E heater experiment performed at the MTRL is an experiment that simulates the very early phase after waste emplacement according to the Swiss repository concept at a 1:2 scale. It was built and started in 2011 in the frame of the EC-funded PEBS project (FP7/2007-2011, grant agreement no. 249681) until 2014 and is now running on behalf of a consortium of NAGRA, ENRESA, BGR, Obayashi, and GRS (German funding organisation: BMWi, FKZ 02E10689). This experiment is the first realistic in-situ experiment where granular buffer materials are used.

In contrast to preceding numerical simulations (Gaus et al. 2014, Garitte 2016) the emphasis of the model calculation presented here is on the geometrical detail and the resulting improvement in simulating the effects recorded in the near field of the heaters.

2. THE HE-E EXPERIMENT

The HE-E features two test sections in a micro-tunnel of 1.3 m diameter and 10 m length, with electrical heaters simulating the thermal input of the high-level waste. The heaters are resting on highly compacted bentonite blocks and the remaining space is filled with granular bentonite or sand-bentonite buffer (Fig. 1). Each heater has a length of 4 m and supplies a maximal power of 2400 Watt. The sections are separated by concrete plugs (Teodori et al. 2012).

Installation of the experiment began in December 2010, and the heaters were started in June 2011. The first two days of heating were used as a calibration phase with a power of 150 – 200 Watt. Afterwards the power was increased in several linear phases until a maximum temperature of 140 °C on the liner surface was reached, which has been kept constant since then.

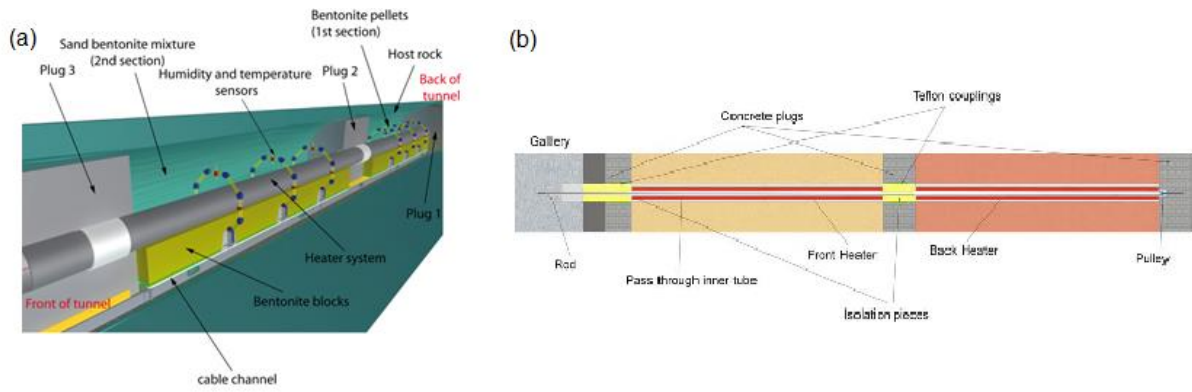


Figure 1. Overview of the HE-E configuration (Teodori et al. 2012).

The main objective of the HE-E is to gain insight in the early non-isothermal re-saturation period of the buffer and its impact on the thermal-hydraulic-mechanical (THM) behaviour of the system. Particular objectives are to provide the experimental database required for the calibration and validation of existing THM models of the early re-saturation phase and to verify upscaling of the thermal conductivity of the partially saturated buffer from laboratory to field scale for two types of candidate granular buffer materials: pure bentonite (sodium bentonite) and a 65/35 sand-bentonite mixture. Figure 2 shows the bentonite blocks and the liner.



Figure 2. Construction of the HE-E Experiment

The Opalinus clay around the micro-tunnel was already equipped with measurement sensors due to a preceding ventilation experiment (Mayor et al. 2007). In the course of the HE-E experiment the instrumentation was extended. Altogether there are measurements of temperature, air humidity, pore pressure and deformation. Figure 3 shows the radial arrangement of the sensors in the buffer material and the bentonite blocks.

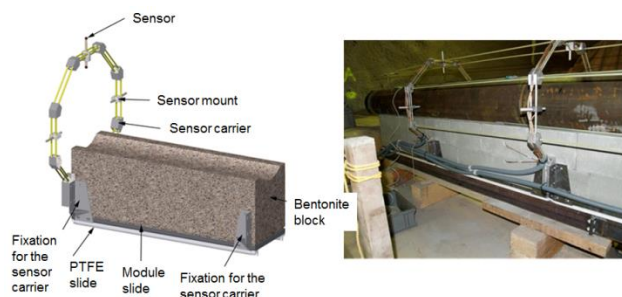


Figure 3. Radial arrangement of the measurement technique in the buffer materials and the bentonite blocks (Teodori et al. 2012).

3. MODELLING

For the realistic simulation of the HE-E (or other large-scale experiments), a three-dimensional representation including the relevant features is considered necessary. For the HE-E, model development has been greatly helped by the VIRTUS virtual underground laboratory (Wieczorek et al. 2014), a data management and visualisation tool into which the geologic and mine structure models of the MTRL were imported and the HE-E model was built. VIRTUS provides realistic 3D sections of the relevant area which can then be used for finite element mesh generation. Figure 4 shows the HE-E section including the micro-tunnel and the parallel running Gallery 98, which is expected to have a hydraulic influence, after mesh generation with GiD. Modelling is performed in steps with increasing complexity using CODE_BRIGHT.

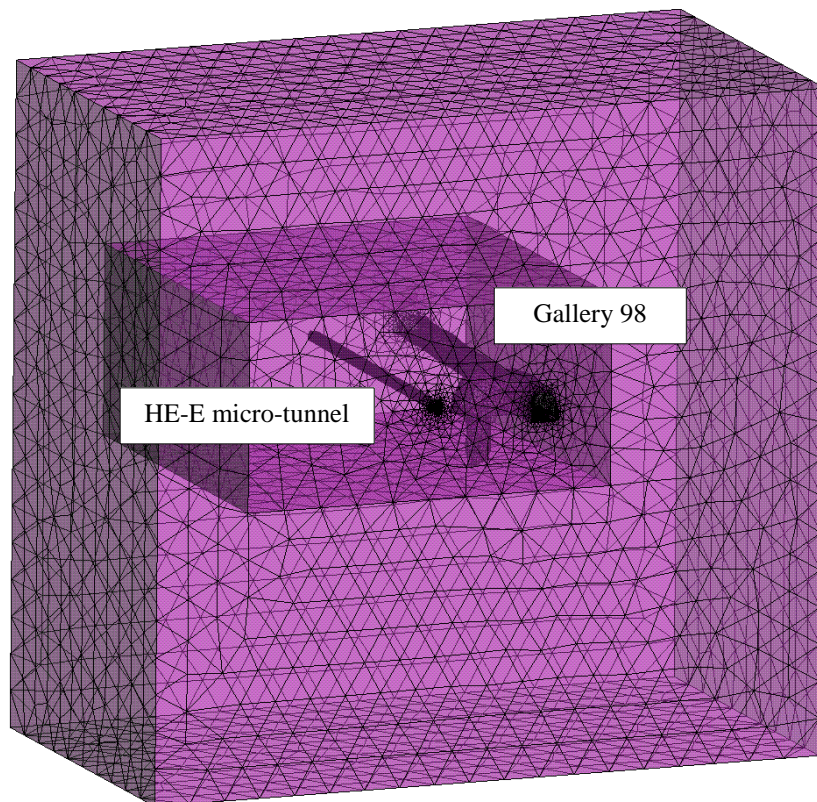


Figure 4. Detail of the finite element model for simulation of the HE-E experiment (centre: microtunnel, right: Gallery 98)

The excavation of the micro-tunnel and the ventilation experiment are modelled by first applying an atmospheric pressure on the surfaces of the micro-tunnel and the Gallery 98 and shortly afterwards a suction of -2 MPa, which represents de-saturation by ventilation. The installation of the HE-E experiment is by installing the respective materials, each with a suction given by their initial saturation. Relevant material parameters were investigated in laboratory experiments. Table 1 shows important parameters (Gaus et al. 2014). The boundary conditions for temperature were pre-determined by the measurement data and applied as prescribed temperatures on the heater surfaces. The simulation steps are shown in table 2.

Table 1. Material parameters

Parameter		Opalinus clay	Bentonite	Sand-Bentonite	Bentonit-Blocks
Porosity	Φ_0	0.137	0.45	0.47	0.33
Initial saturation	S	1	0.45	0.24	0.63
Saturated permeability	k_{sat}	2.0E-20	3.5E-20	1.2E-13	2.5E-21
Thermal conductivity	λ_{dry}	1.3	0.3	0.3	0.8
	λ_{sat}	1.9	1.3	1.3	1.3

Table 2. Simulation steps

Interval	Time [d]	
1	0.0 – 100.0	<ul style="list-style-type: none"> Initial conditions: T = 14 °C; P₁ = 1.75 MPa Excavation Gallery 98 and micro-tunnel
2	100.0 – 4474.0	<ul style="list-style-type: none"> time between excavation and ventilation experiment (VE) period of the VE time between the end of VE and begin of building up HE-E
3	4474.0 - 4484.0	<ul style="list-style-type: none"> installation of HE-E experiment
4	4484.0 – 4505.0	<ul style="list-style-type: none"> isothermal phase
5	4505.0 – 4507.0	<ul style="list-style-type: none"> calibration phase (T_{Anfang} = 14 °C, $\Delta T = 2$ °C, T_{End} = 16 °C;)
6	4507.0 – 4600.0	<ul style="list-style-type: none"> first heating phase (T_{Anfang} = 16 °C, $\Delta T = 94$ °C, T_{End} = 110 °C;)
7	4600.0 – 4869.0	<ul style="list-style-type: none"> second heating phase (T_{Anfang} = 110 °C, $\Delta T_B = 80$ °C, T_{End,B} = 190 °C; $\Delta T_{SB} = 70$ °C, T_{End,SB} = 180 °C)
8	4869.0 – 5599.0	<ul style="list-style-type: none"> constant temperature (T_{Bentonite}=190 °C; T_{Sand-Bentonite}=180 °C)

The first step, a pure thermal simulation, has been completed. A comparison of the measured temperature at various points in the buffer with an earlier TH-coupled plane 2D calculation and the new 3D simulation results shows a significant improvement, even though saturation changes had to be neglected in this first step (Fig. 5). The red sensor which is the farthest of to the heater could be modelled perfectly with the thermal 3D simulation. However, the sensor nearest the heater (pink) shows a deviation of about 5 °C.

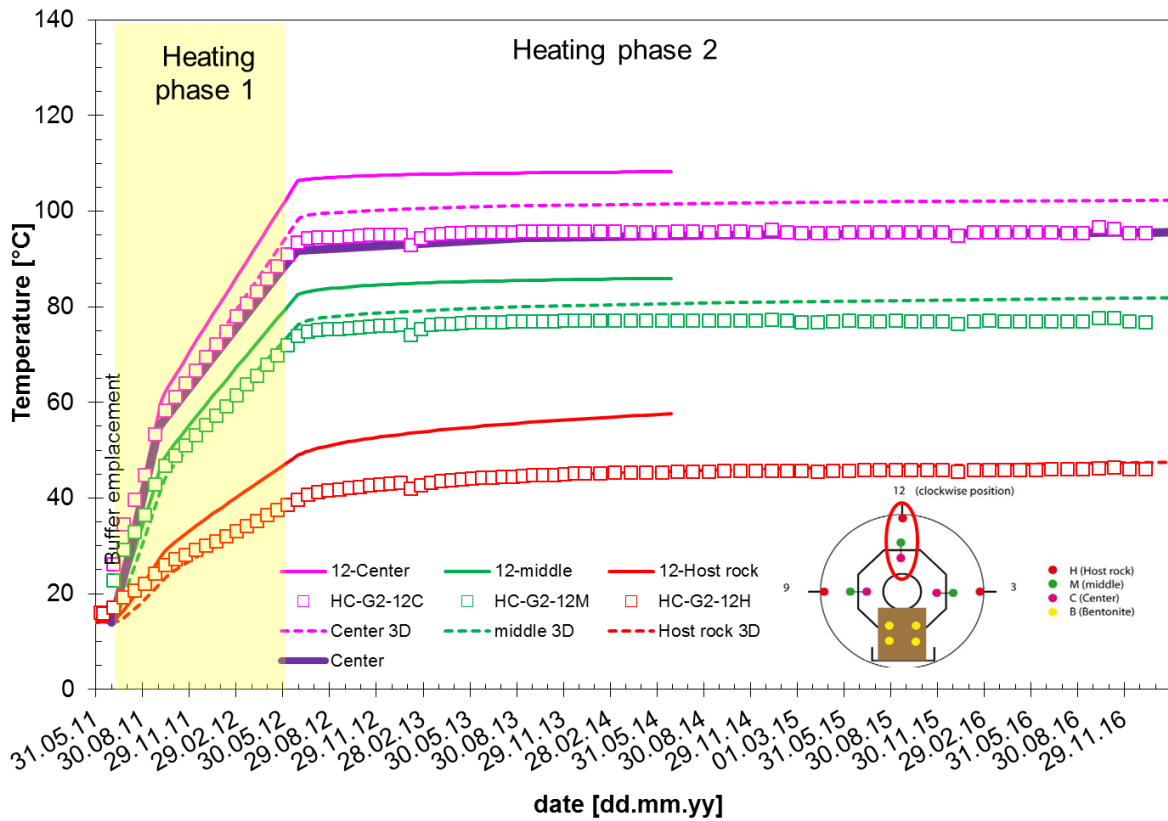


Figure 5. Temperature evolution in the HE-E buffer (centre of sand-bentonite section), in the granular buffer 10 cm (12C), 25 cm (12M) and 45 cm (12H) above the heater liner surface. Squares = measurement data, full lines = 2D simulation, dotted lines = thermal 3D simulation, big purple line = TH coupled 3D simulation

The next step, a coupled TH simulation, is in progress. There are first results for the temperature shown in figure 5 (purple line). With consideration of hydraulic effects in the TH-coupled 3D simulation, the pink sensor could be simulated very well. As a first intermediate result it is to be seen that a TH-coupled three-dimensional simulation shows a significant improvement and a satisfactory reproduction of the measurement data.

Furthermore, there is an inhomogeneous temperature distribution on the steel liner because of the different thermal conductivities of granular buffer and blocks. This phenomenon could be simulated very well with the TH-coupled 3D simulation, since the inside of the heater liner was modelled realistically. Figure 6 shows the calculated temperature distribution, while figure 7 shows the measured temperature of two sensors on the liner.

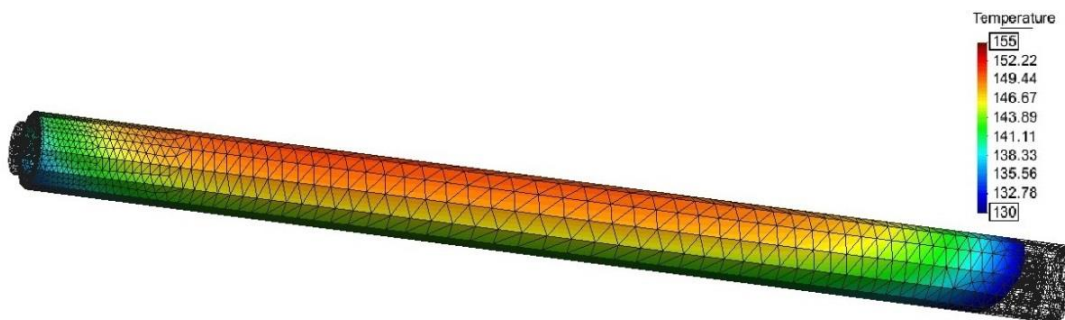


Figure 6. Modelled temperature distribution on the liner surface

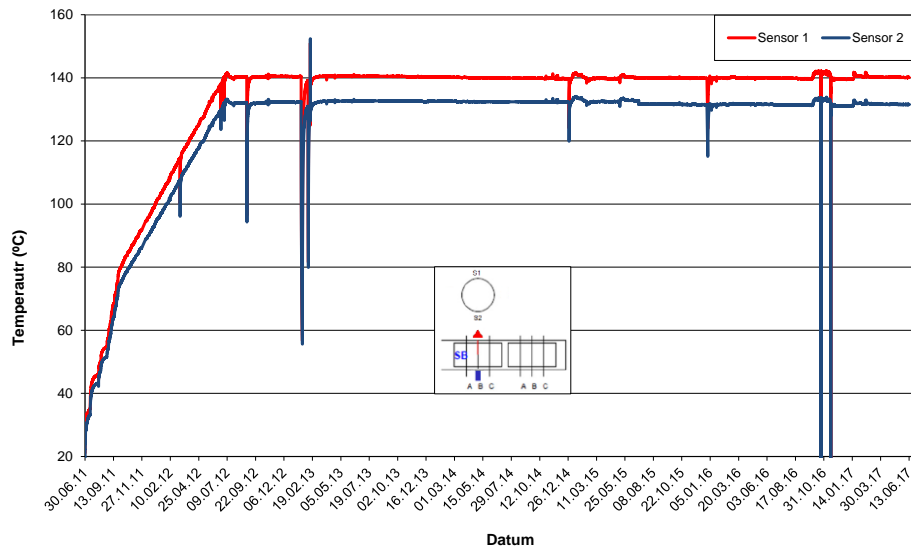


Figure 7. Measured temperature distribution on the liner surface

4. Conclusion and outlook

The first results show a significant improvement in the modelling of temperature by a three-dimensional approach. Consideration of hydraulic effects on thermal properties brings a further improvement. In this first step of TH-coupled modelling phase transitions were neglected. In ongoing simulations these are included. A fully coupled THM simulation will complete the simulation work.

ACKNOWLEDGEMENT

This research work was funded by the German Federal Ministry for Economic Affairs and Energy (BMWi) under contract no. 02E10689.

We would like to express our thanks to all our colleagues who participated in this project without actually being an author of this report.

REFERENCES

- Garitte, B.;** DECOVALEX-2015 project, task B1 final report, KTH Architecture and the Built Environment, May 2016
- Gaus, I., B. Garitte, R. Senger, A. Gens, R. Vasconcelos, J.-L. Garía-Sineríz, T. Trick, K. Wieczorek, O. Czaikowski, K. Schuster, J.C. Mayor, M. Velasco, U. Kuhlmann, M.V. Villar;** The HE-E Experiment: Layout, Interpretation and THM Modelling, Combining D2.2-11 and D3.2-2 of the PEBS Project, May 2014. <https://www.pebs-eu.de/PEBS/EN/Downloads>
- Mayor, J.C., García-Siñeriz, J.L., Velasco, M., Gómez-Hernández, J., Lloret, A., Matray, J.-M., Coste, F., Giraud, A., Rothfuchs, T., Marschall, P., Roesli, U., Mayer, G.;** Ventilation Experiment in Opalinus Clay for the disposal of radioactive waste in underground repositories, in: Bossart, P., Nussbaum, C.; Mont Terri Project – Heater Experiment, Engineered Barrier Emplacement and Ventilation Experiment, *Swiss Geological Survey, Bern, 2007.*
- Mont Terri;** 2018. <https://www.mont-terri.ch>
- Teodori, S.-P., I. Gaus, S. Köhler, J.-C. Mayor, C. Nussbaum, U. Rösli, K. Schuster, J.-L. García Siñeriz, P. Steiner, T. Trick, H. Weber, K. Wieczorek;** Report on the construction of the HE-E experiment, Deliverable D2.2-3 of the PEBS Project, 2012. <https://www.pebs-eu.de/PEBS/EN/Downloads>
- Wieczorek, K., J. Behlau, U. Heemann, S. Masik, C. Müller, M. Raab, E. Kuate Simo;** VIRTUS – Virtuelles Untertagelabor im Steinsalz, Abschlussbericht, GRS-354, Gesellschaft für Anlagen- und Reaktorsicherheit (GRS) gGmbH, Dezember 2014.

MODELLING OF CEMENT-GROUNDWATER-ROCK INTERACTION AT THE GRIMSEL TEST SITE (SWITZERLAND)

M. Carme Chaparro ^a, Maarten W. Saaltink ^b and Josep M. Soler ^c

^a Karlsruhe Institute of Technology (KIT), Institute of Applied Geosciences (AGW), Kaiserstraße 12, 76131 Karlsruhe, Germany, e-mail: mcarme.chaparro@gmail.com

^b Department of Civil and Environmental Engineering, Universitat Politècnica de Catalunya (UPC), Jordi Girona 1-3, 08034 Barcelona, Spain, e-mail: maarten.saaltink@upc.edu

^c Institute of Environmental Assessment and Water Research (IDAEA), CSIC, Jordi Girona 18, 08034, Barcelona, Spain, e-mail: josep.soler@idaea.csic

Key words: Reactive transport, Cement, Hyperalkaline plume, Numerical model.

Abstract. *A five years in situ experiment at the Grimsel Test Site (Switzerland) to study water-cement-rock interaction in fractured granite was modelled. It consisted of a hardened cement source in a borehole intersecting a water conducting fracture. Grimsel groundwater was injected into this borehole, and the evolution of water composition was monitored. The modelling approach was based on a 1D radial model for the emplacement borehole and a small volume of rock (fault gouge) around it, and a 2D model for the rest of the domain. Results showed dissolution of the fault gouge minerals. In the cement, there is an increase on porosity due to portlandite dissolution, and a decrease of porosity at the edge of the alkaline plume due to mainly calcite precipitation.*

1 INTRODUCTION

Ordinary Portland Cement (OPC) is frequently used for radioactive waste storage as a part of the engineered system or as structural support in the host rock. The cement pore water is hyperalkaline (pH>13) and can react chemically with the host rock of the repository. Our study was part of the LCS project (Long-Term Cement Studies), with the objective of studying water-cement-rock interaction and its effect on water flow and solute transport properties. To do so, an in situ experiment lasting five years was performed at the Grimsel Test Site underground laboratory (Switzerland, www.grimsel.com). A hardened cement source was installed in a borehole intersecting a water conducting fracture. Then, Grimsel groundwater was circulated or injected into this borehole and the evolution of water composition in the fracture was monitored for 5 years. A preliminary reactive transport model corresponding to the formation of a high-pH plume and its interaction with the rock was reported by Saaltink and Soler (2016). The conceptual model considered a 1D radial model for the emplacement borehole and a small volume of surrounding rock (fault gouge), and a 2D model for the rest of the domain. The results of the 1D model were used as input for the 2D model. Following the conceptual model of Saaltink and Soler (2016), the objective of our study is to develop a qualitative and partially quantitative understanding of the geochemical processes that took place during the experiment.

2 IN SITU EXPERIMENT

The experiment was performed at the Grimsel underground rock laboratory (Switzerland). Pre-hardened Ordinary Portland Cement hollow cylindrical segments were emplaced in a borehole (emplacement borehole) intersecting a water-conducting fracture. Starting from the

centre, the borehole contained an inner dummy (inert cylinder) followed by the cement and a water-filled gap. Two other boreholes (called observation and extraction boreholes) were placed at 0.56 and 1.12 meters away from the emplacement borehole. There were no cement pieces in the observation and extraction boreholes. A skin of low permeability was assumed to surround the boreholes (Figure 1). Grimsel groundwater was circulated and injected in the emplacement borehole. Water was extracted at the observation and extraction boreholes and the chemical compositions of the different solutions were monitored. After the injection was started in the emplacement borehole, elevated pH and solute concentrations reflecting interaction with the cement were observed in the observation and extraction boreholes.

3 NUMERICAL MODEL

Our conceptual model considered only a simple homogenous fracture of 5 mm thickness, taking into account the reactions that could have occurred during the interaction between the cement, Grimsel groundwater and the fault gouge filling the fracture. The simulations were carried out using the Retraso-CodeBright⁽ⁱⁱ⁾. This software package couples CodeBright⁽ⁱⁱⁱ⁾ to a module for reactive transport modelling, including aqueous complexation reactions, adsorption and precipitation/dissolution of minerals. The modelling approach considered two different models (1D radial and 2D). First, a detailed 1D radial model simulated the emplacement borehole (hardened cement paste) together with the surrounding skin (Figure 1b). Then, the results of this model (solute concentrations at the outer boundary of the skin of the emplacement borehole) were used as input for the 2D model that simulated the fracture plane at the scale of all three boreholes (emplacement, observation and extraction). The conceptual model assumed that during the initial test period without injection of water in the borehole the permeability in the skin was low enough to avoid flow of water in that zone. It also assumed that when water was injected, the flow in the skin was only affected by this injection (radial flow) and was not affected by the extraction in the other boreholes.

Table 1 displays the transport parameters of the materials used in the 1D and 2D models. In order to simulate the varying flow regime we used the monitored flow rates. The 1D model assumed a time dependent injection flow rate of the Grimsel groundwater at the gap of the emplacement borehole. The 2D model considered the time depending flow rates at the three boreholes.

	k (m ²)	ϕ	D_p (m ² s ⁻¹)	α_L (m)	α_L (m)
1D model					
Cement	8.0×10^{-18}	0.47	2.0×10^{-11}	0.002	-
Gap	3.0×10^{-10}	1.0	1.0×10^{-5}	10.0	-
Skin	3.0×10^{-15}	0.21	1.0×10^{-9}	0.02	-
2D model					
Gap	3.0×10^{-10}	1.0	1.0×10^{-5}	10.0	10.0
Skin	3×10^{-14} - 3×10^{-13}	0.21	1.0×10^{-9}	0.1	0.05
Fault gouge	3.0×10^{-13}	0.21	1.0×10^{-9}	0.1	0.05

Table 1: Parameters of the materials used in the 1D and 2D models^(iv).

The primary phases of the cement that were taken into account are C-S-H gel (Ca/Si=1.667), portlandite, ettringite, siliceous hydrogarnet and hydrotalcite. The potential secondary phases considered were C-A-S-H, tobermorite, calcite, monosulfoaluminate, monocarboaluminate, illite and M-S-H. The minerals of the fault gouge considered were quartz, K-feldspar, albite,

muscovite and phlogopite. The rate laws used for the primary minerals in the fault gouge were based on those used by Soler and Mäder (2010). For all the other phases (cement and secondary phases), large values of the rate constants and of the surface areas were used, leading to local equilibrium with respect to those phases. Initially, the gap had no minerals but large surface areas were implemented to allow mineral precipitation. The initial composition of the cement porewater is at equilibrium with the cement phases. The initial composition of the Grimsel groundwater was at equilibrium with the minerals of the fault gouge and was also based on the monitored data.

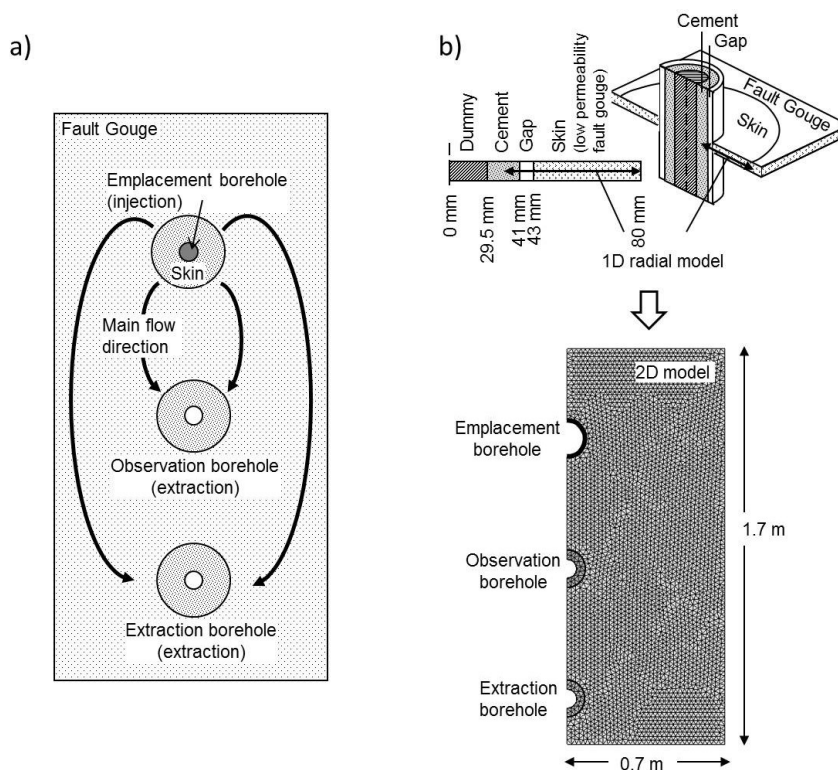


Figure 1: Conceptual model: a) Plan view of the fracture plane with the three boreholes; lines indicate the main direction of flow, b) Geometry of the 1D and 2D models ^(iv).

4 RESULTS AND DISCUSSION

4.2 1D model

The measured and modelled aqueous chemistry against time at the gap of the emplacement borehole can be compared qualitatively in order to understand the reactions that have occurred during the experiment. Generally, the measured data are more scattered than the model results. A possible explanation is the assumption of ideally mixed water in the gap. The model showed that at the beginning there was a rapid increase of pH, Ca, K and Na concentrations because of out-diffusion from the cement. Si decreased due to diffusion towards cement and SO₄ decreased because of precipitation in the rock (ettringite) plus diffusion from the gap towards the rock. Cl and F also decreased because cement pore water did not contain these components. From the beginning of the injection on, Ca concentration varied according to the changes in the flow rates. Higher injection rates implied lower Ca concentrations. K and Na concentrations decreased until the high concentrations disappeared from the cement pore water. Si

concentration remained approximately constant, as the concentrations of the Grimsel water and the cement pore water were very similar. pH varied according to the variations in Ca concentration.

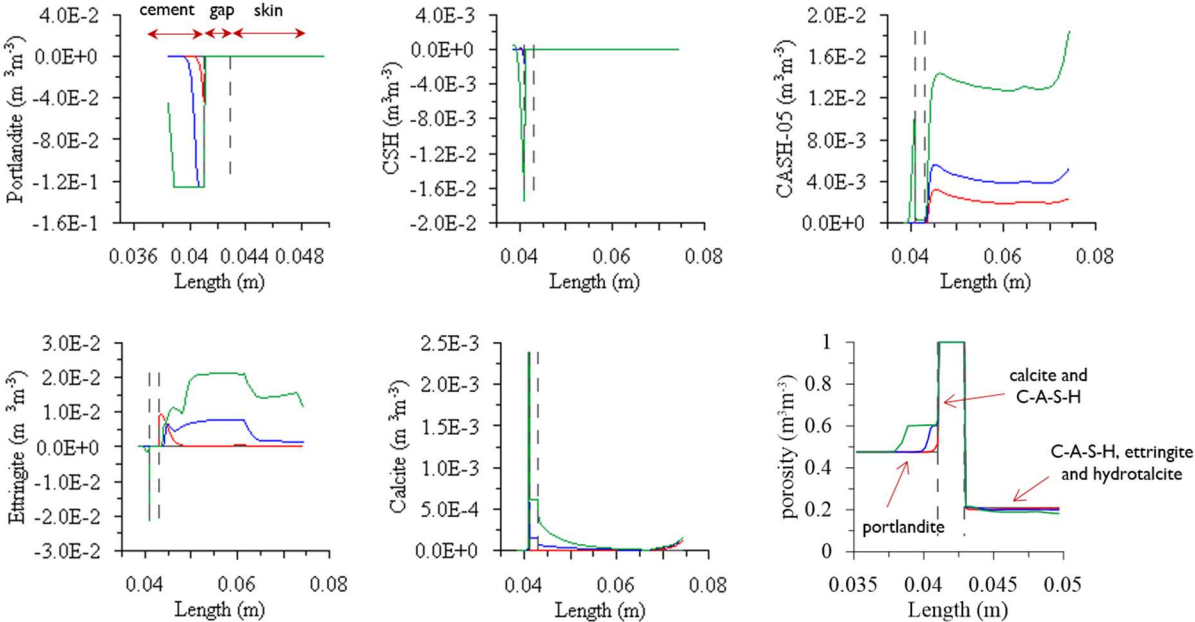


Figure 2: Variation of volumetric fraction of the minerals against length. Positive values mean precipitation and negative ones mean dissolution. Vertical dashes lines indicate the gap. Red colour indicate the end of diffusion period (2010), blue colour the change of injection rate (2011) and green colour the end of the experiment (2014).

Figure 2 displays the variation of volumetric fraction of minerals versus distance calculated by the numerical model. In the x axis, cement (from 0.035 to 0.041 m), gap (from 0.041 to 0.043 m) and the skin (from 0.043 to 0.08 m) are represented. These results could be compared with the post-mortem analysis and the mineralogical analysis. In the cement, model results show dissolution of portlandite, with a sharp dissolution front at 3 mm from the cement-gap interface after 5 years. This dissolution of portlandite, which was also observed in the post-mortem analysis, allowed the calibration of the pore diffusion coefficient ($2 \times 10^{-11} \text{ m}^2/\text{s}$). Also C-S-H dissolved though at a smaller rate. Etringite dissolved at the interface between the cement and gap only after injection of water was started. On the other hand, after injecting Grimsel groundwater, C-A-S-H precipitated near the gap and calcite did at the cement-gap interface and into the gap, due to the mixing of both waters. This calcite precipitation at the interface was also observed in the post-mortem analysis (unpublished results). At the skin, during both diffusion and injection periods, the primary minerals of the fault gouge (quartz, albite, K-feldspar, muscovite and phlogopite) dissolved due to the high-pH conditions. Also, there was precipitation at the skin of C-A-S-H, ettringite and hydrotalcite. The porosity change in the cement paste is mainly due to portlandite dissolution. It increased by 0.12 corresponding to the initial volume fraction of portlandite in the cement. The porosity reduced slightly in the skin next to the gap due to C-A-S-H, ettringite and hydrotalcite precipitation.

4.3 2D model

The modelled and measured aqueous chemistry versus time for the observation and extraction boreholes can be compared qualitatively. Results showed that changes in flow rates

(mainly emplacement) caused noticeable changes in concentrations in all boreholes, which was consistent with the observed oscillations in the measurements. Nevertheless, as for the emplacement borehole, the monitored data showed more scattering. In addition, the model seemed to overestimate the effect of the alkaline plume at the observation borehole. These discrepancies could be attributed to simplifications in the 1D model; its results were used as input for the 2D model. In addition, heterogeneity in both permeability and distribution of minerals could have an effect, which was not taken into account by the model (an initially homogeneous fracture was assumed). Bearing these limitations in mind, reasonable fits were obtained for both observation and extraction boreholes. However, modelled Si concentrations are somewhat lower than the measured ones. This is because the initial composition of Grimsel groundwater assumes equilibrium with quartz.

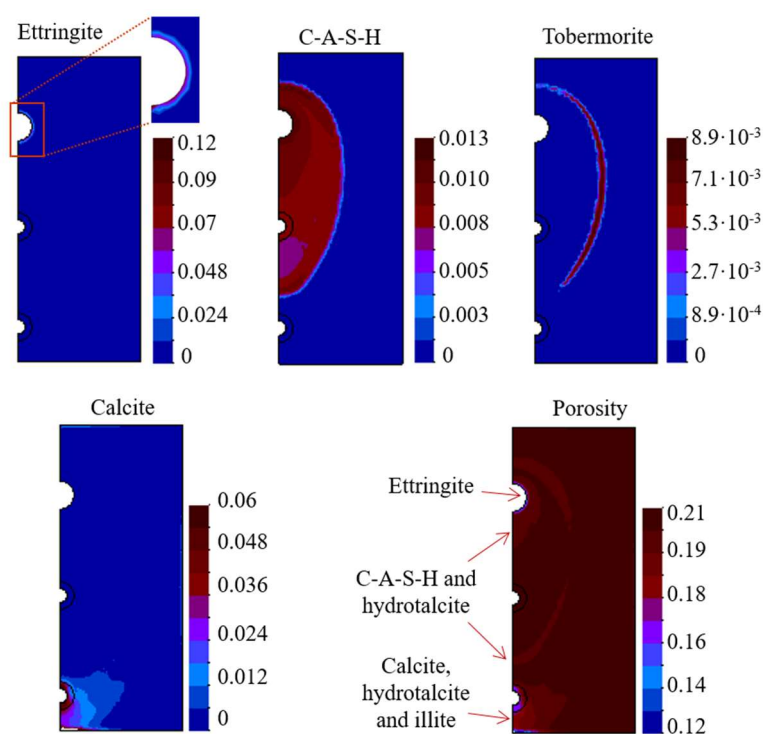


Figure 3: Variation of volumetric fraction of the minerals at the end of the experiment. Positive values mean precipitation and negative ones mean dissolution. Variation of porosity is also plotted. Dimensions are 1.7x0.7m.

All the minerals of the fault gouge (quartz, albite, K-feldspar, muscovite and phlogopite) were affected by dissolution in the centre of the plume, due to the increase in pH. Precipitation and dissolution of secondary minerals are shown in Figure 3. Ettringite precipitated at the edge of the emplacement borehole skin. CA-S-H precipitated in the centre of the plume followed by the precipitation of tobermorite. Hydrotalcite precipitated at the centre of the plume and near the extraction borehole. Small amounts of monocarboaluminate and hydrogarnet also precipitated at the centre of the plume. Near the extraction borehole there was a lot of precipitation of calcite and to a lesser extent also of illite. This precipitation of calcite is because of the high extraction flow rate near that borehole, causing a lot of mixing between the alkaline water and Grimsel groundwater. Figure 3 also shows the distribution of porosity. Near the emplacement borehole there was a reduction in porosity of 0.02 due to ettringite precipitation. In the centre of the plume there was a similar reduction due to C-A-S-H and hydrotalcite

precipitation. Near the extraction borehole there was high reduction in porosity of 0.09, because illite and especially calcite precipitated at the outer edge of the plume. The pH reflected the distribution of the alkaline plume, with higher pH close to the emplacement borehole because of the cement source and lower pH near the extraction borehole.

5 CONCLUSIONS

- The interaction of cement and rock at the Grimsel Test Site was modelled. The conceptual model consisted of a simple flow system considering a homogeneous fracture and a chemical system for the interaction between the cement, groundwater and fault gouge filling the fracture. Modelling approach consisted of a 1D radial model simulating the emplacement borehole with the cement paste and the surrounding skin, and a 2D model starting at the emplacement borehole skin and including the two other boreholes (observation and extraction). The solution composition at the outer boundary of the 1D model was incorporated into the 2D model as a boundary condition.
- In both models, results showed that changes in flow rates, mainly in the emplacement borehole, cause noticeable changes in concentrations in all boreholes.
- The numerical models predicted dissolution of primary minerals of the fault gouge (albite, K-feldspar, phlogopite, muscovite and quartz). The 1D model showed a reduction of porosity in the cement due to portlandite dissolution. The 2D model predicted different scenarios according to the location within the plume. At the centre of plume there is porosity reduction, because of precipitation of C-A-S-H, ettringite, tobermorite and hydrocalcite. At the outer part of the plume (near the extraction borehole), there is porosity reduction due to precipitation of illite, hydrotalcite and especially calcite.

REFERENCES

- [i] Saaltink, M. W., Soler, J. M., 2016. Grimsel Test Site - Long-Term Cement Studies. Reactive transport modeling of experiment 2 at Grimsel. Tech. rep., POSIVA OY, Working Report 2016-14
- [ii] Saaltink, M. W., Batlle, F., Ayora, C., Carrera, J., Olivella, S., 2004. Retraso, a code for modeling reactive transport in saturated and unsaturated porous media. *Geologica Acta*, 2 (3), 235-251.
- [iii] Olivella, S., Gens, A., Carrera, J., Alonso, E.E., 1996. Numerical formulation for a simulator (code_bright) for the coupled analysis of saline media. *Eng. Comput.* 13 (7), 87–112.
- [iv] Chaparro, M.C., Saaltink, M.W., Soler, J.M., 2017. Reactive transport modelling of cement-groundwater-rock interaction at the Grimsel Test Site. *Physics and Chemistry of the Earth*, 99, 64-76.
- [v] Soler, J. M., Mäder, U. K., 2010. Cement-rock interaction: Infiltration of a high-pH solution into a fractured granite core. *Geologica Acta*, 8 (3), 221-233.

ASSESSMENT OF A FEBEX MODEL

A. Rodriguez-Dono* and S. Olivella*

* Department of Civil and Environmental Engineering
Technical University of Catalonia (UPC)
Campus Nord UPC, 08034 Barcelona, Spain
e-mail: code.bright@upc.edu
web page: https://deca.upc.edu/en/projects/code_bright

Key words: Sensitivity analysis, coupled analysis, swelling, bentonite, nuclear waste.

Abstract. *This paper assesses a model for the FEBEX (full-scale engineered barrier experiment) in-situ test, simulating the disposal of heat-emitting, high-level spent nuclear fuel. The model has been developed using CODE_BRIGHT. This model is based on previous modelling efforts. The model focuses on the thermo-hydro-mechanical behaviour of the bentonite barrier surrounding a heater that simulates the heat production of radioactive spent fuel.*

1. Introduction

The present report contains the description of a model for the large-scale in situ heating test FEBEX (full-scale engineered barrier experiment). In this test, after five years of heating, one of the heaters was switched off and the experiment was partially dismantled, allowing the final state of the barrier to be observed directly. In this way, very valuable information on the state of the bentonite at the end of the test was obtained. The test has received attention during the initial (Gens et al., 1998) and intermediate stages (Alonso & Alcoverro, 2005). Finally, Gens et al. (2009) discussed the thermal, hydraulic and mechanical observations in the bentonite barrier and in the host rock, paying special attention to the progress of hydration in the barrier, the effects of heating and vapour transport, and the development of swelling pressures in the barrier.

In the FEBEX experiment, heaters are emplaced in the axis of a tunnel excavated in granite to simulate the heat production of radioactive waste. The test is fully instrumented, and attention is focused on the thermo-hydro-mechanical (THM) behaviour of the near-field region constituted by the compacted bentonite barrier surrounding the heater and the immediately adjacent rock. Interpretation of the test is assisted by the performance of a coupled numerical analysis based on a formulation that incorporates the relevant THM phenomena. Further description of the FEBEX in situ test can be found in Gens et al. (2009).

The model of this test has been developed using CODE_BRIGHT (Olivella et al., 1994 and 1996), a Finite Element Method program that enables coupled thermo-hydro-mechanical analysis in geological media. This is a code version that incorporates customized pre- and post- process interfaces so that simulation models that use CODE_BRIGHT —available from https://deca.upc.edu/en/projects/code_bright— can be developed more easily. It allows easy modification of parameters, boundary conditions, excavation protocols, meshing and organization of calculation intervals. The reason is that it has been developed using the GiD interface (<http://www.gidhome.com>) that permits pre- and post- process of data in a user-friendly way.

The model for FEBEX presented in this report is based on the FEBEX Task 9 specifications document (Gens, 2017) and on the material properties of previous modelling efforts (Gens et al., 2009; Sanchez et al., 2012; Rodriguez-Dono et al., 2018).

The main objective of this report is to obtain results from the mentioned FEBEX model to make comparisons with in-situ measurements and results from other codes. Moreover, Rodriguez-Dono et al., 2018 also developed a model of the well-known FEBEX experiment that was exploited in terms of the implementation of additional processes such as coupled flows and double structure models to investigate their impact of hydration and stress development.

Additional information on the full FEBEX project and its modelling is given in Huertas et al. (2006), Villar (2002) and Toprak et al. (2018).

2. UPC's FEBEX stage 1 model

2.1. Main numerical features

The geometry of the model has been taken from the FEBEX Task 9 specifications document (Gens, 2017). The host rock (granite), the bentonite buffer, the concrete plug and the canister (heaters) are the materials considered. Each heater has a volume of 2.89 m³. The model is two-dimensional, assuming axisymmetry along the tunnel axis.

The mesh of the model is composed of 2687 quadrilateral elements. Unlike the model used in Gens et al. (2009), this model takes advantage of the unstructured mesh development for the discretization of the host rock. With an unstructured mesh, the model will have less elements in the host rock section and thus, it will run faster. However, the buffer is discretized with a structured mesh, as this is more adequate in the zone of interest to reduce numerical errors.

Table 1 shows the intervals considered in this analysis. Heaters switch on at 0.001 days and day 1968 would correspond to the end of the first dismantling. However, no excavation has been modelled corresponding to this first dismantling. Only the heater#1 switch off has been considered so far.

In order to match the measured evolution of temperature during the experiment (see more details about this in Gens et al., 2009), the heat power was progressively modified (see table 1) until the 100°C target temperature was reached. Note that the design conditions of the experiment contemplate a maximum temperature of 100°C at the contact between the heater and bentonite (Villar, 2002; Huertas et al., 2006); since it is assumed that engineered clay barriers do not change their properties for temperatures below 100°C. From that point on, the temperature was prescribed at the value of 100°C in both heaters. Later, one of the heaters was removed but the other continued heating.

2.2. Initial and boundary conditions

A mechanical boundary condition restraining the normal displacements has been applied all along the external boundary for all time intervals. The initial stress has been set to -28 MPa in the granite and to -0.5 MPa in the rest of the materials (negative values correspond to compression). The initial suction of the bentonite has been set to -135 MPa. Finally, an initial porosity of 0.1 has been set for the concrete plug, and an initial porosity of 0.01 has been set for both the granite and the canister. For the bentonite, the initial porosity has been set to 0.375.

In addition, a constant liquid pressure of 0.9 MPa is imposed on the external boundary, corresponding to the unaltered far host rock (granite). To simulate ventilation, a water pressure of

-1 MPa has been set in the excavated tunnel before construction of the bentonite buffer. After construction, a water pressure of 0.1 MPa has been set on the remaining unconstructed tunnel walls.

As indicated above, during intervals 3 to 4 the power of the heaters is prescribed and therefore the temperature increases. Once the temperature reaches the target value on the surface canister (100 °C) the boundary condition on the heater is changed from constant power to constant temperature (more information about boundary condition implementation in the Code_Bright User's Guide (2018), downloadable from the Code_Bright web page – deca.upc.edu/en/projects/code_bright).

Table 1. Time intervals considered for the simulation up to 1968 days

Time interval #	Comments	Initial time (days)	Final time (days)	Prescribed heat flow $\left(\frac{\text{J}}{\text{s m}^3}\right)$	Prescribed temperature (°C)
1	Excavation in granite rock	-100	0	—	12
2	Construction of bentonite, canisters and concrete plug	0	0.001	—	12
3	Heaters switch on to 1200 W	0.001	20	415	—
4	Heaters to 2000 W	20	53	692	—
5	Heaters at 100°C	53	1827	—	100
6	Heater #1 switch off Heater #2 at 100°C	1827	1968	—	0 (heater #1) 100 (heater #2)

2.4. Results

2.4.1. Heating power

A constant power of 1200 W was applied to the heaters during the first 20 days of operation. Power was then increased to 2000 W and maintained constant for an additional period of 33 days. Then, at day 53, the heating system was switched to an automatic constant temperature control mode to achieve a constant maximum temperature of 100°C in the bentonite.

2.4.2. Relative humidity

Figure 1 shows the computed distributions of relative humidity along radial segments on sections C, E1, H and F2) at 2 different times (90 and 1800 days). Figure 2 shows the computed evolutions of relative humidity given at 3 points (P1, P2 and P3) on 3 sections C and E1 from $t = 0$ days to $t = 1855$ days.

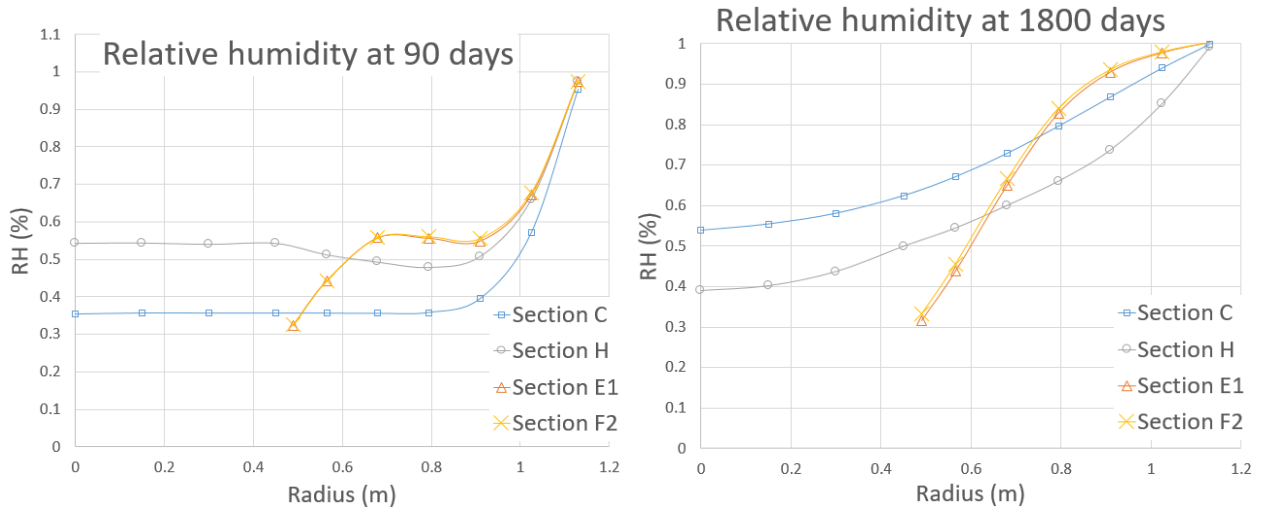


Figure 1. Computed distributions of relative humidity along radial segments on 4 sections (C, E1, H and F2) at 2 different times (90 and 1800 days).

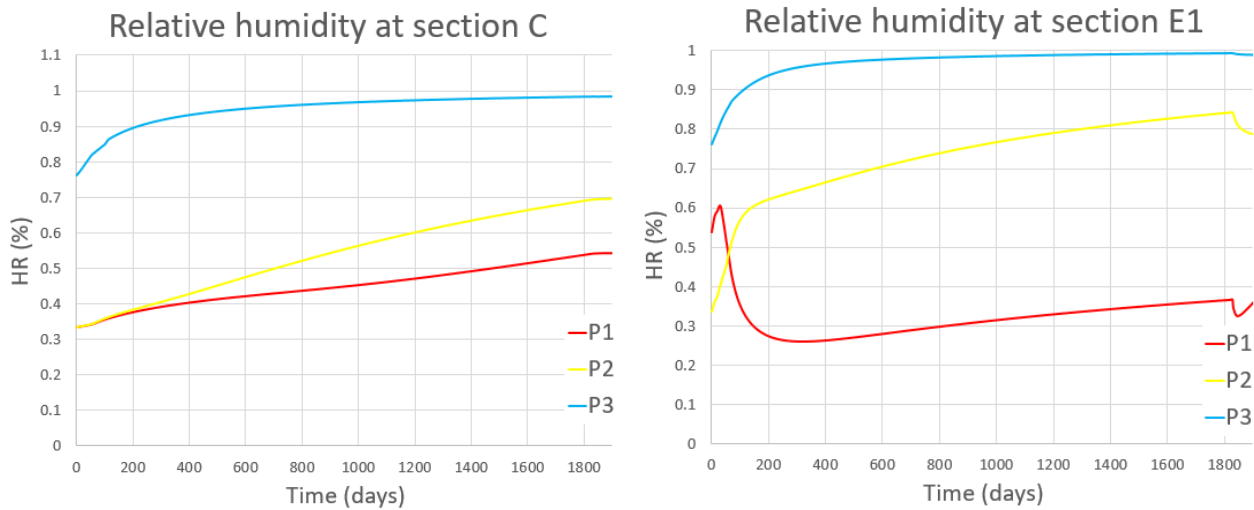


Figure 2. Computed evolutions of relative humidity given at 3 points (P1, P2 and P3) on 3 sections (C, E1 and H) and at 2 points (P1 and P2) on 1 section (F2) from $t = 0$ to $t = 1855$ days.

2.4.3. Temperature

Figure 3 shows the computed distributions of temperature along radial segments on 3 sections (D1, I and G) and at 2 different times (90 and 1800 days). Figure 4 shows the computed distributions of temperature along the axial segment at times $t_1 = 90$ days and $t_2 = 1800$ days.

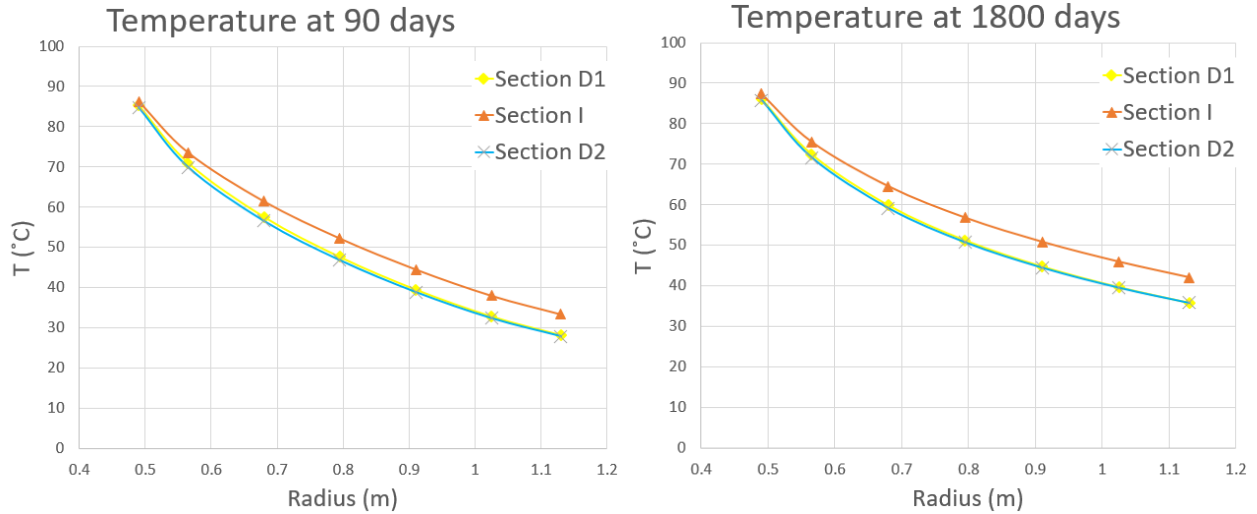


Figure 3. Computed distributions of temperature along radial segments on 3 sections (D1, I and G) and at 2 different times (90 and 1800 days).

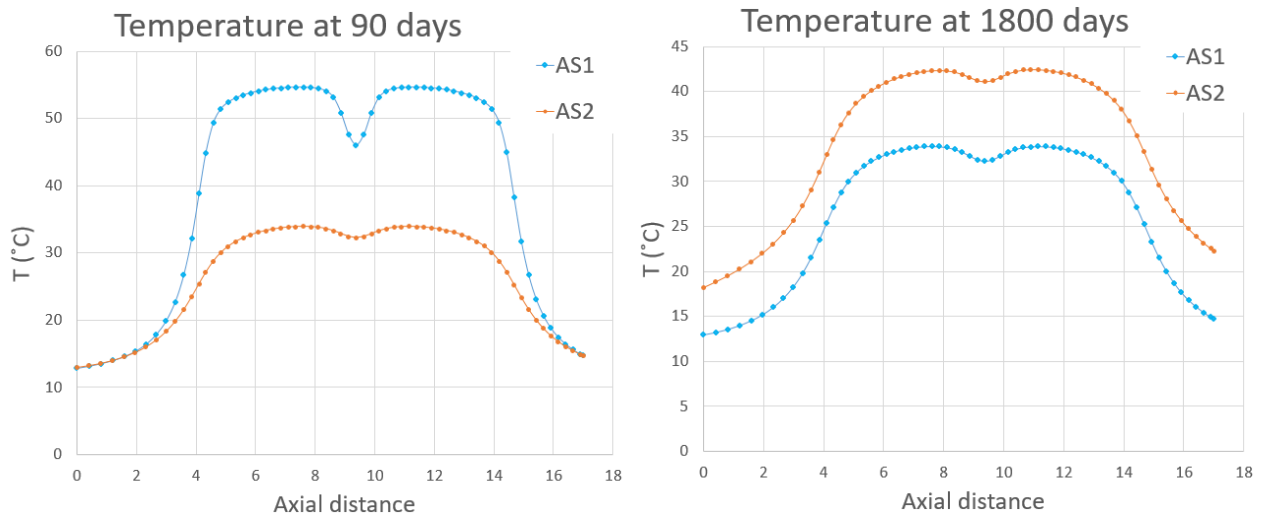


Figure 4. Computed distributions of temperature along the axial segment at times $t_1 = 90$ days and $t_2 = 1800$ days.

2.4.4. Total stresses

Figure 6 shows the computed evolutions of radial total stresses (RTS) at 3 points (P1, P2 and P3) on 1 section (E2) and the computed evolution of axial total stress (ATS) at 1 point (P1) on 1 section (B2) from $t = 0$ days to $t = 1855$ days.

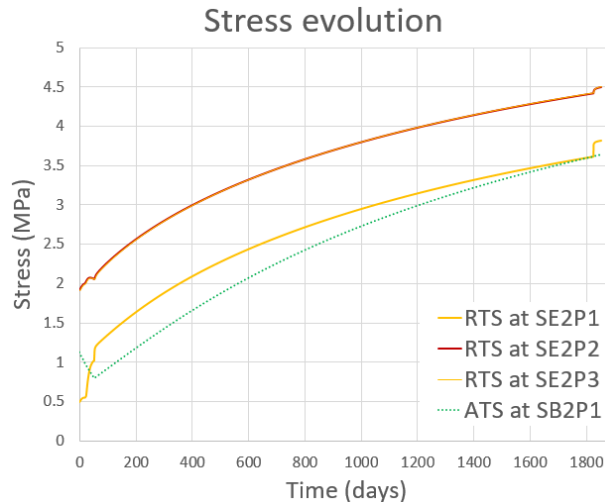


Figure 6. Computed evolutions of radial total stresses (RTS) at 3 points (P1, P2 and P3) on section E2 and axial total stress (ATS) at point P1 on section B2, from $t = 0$ to $t = 1855$ days.

3. References

- Alonso E, Alcoverro J. The FEBEX test as a benchmark case for THM modelling: historical perspective and lessons learnt. In: Alonso E, Ledesma A, editors. *Advances in understanding engineered clay barriers*, London: Taylor & Francis; 2005, p. 3-19.
- Gens A, Garcia-Molina AJ, Olivella S, Alonso E, Huertas F. Analysis of a full scale in situ test simulating repository conditions. *Int J Numer Anal Methods Geomech.* 1998;22(7):515-48.
- Gens A, Sanchez M, Guimaraes LDN, Alonso E, Lloret A, Olivella S et al. A full-scale in situ heating test for high-level nuclear waste disposal: observations, analysis and interpretation. *Geotech.* 2009;59(4):377-99. doi: 10.1680/geot.2009.59.4.377
- Huertas F, Farina P, Farias J, Garcia-Siñeriz JL, Villar MV, Fernandez AM, et al. Full-scale engineered barrier experiment. ENRESA, Madrid. Updated final report, technical publication 05-0/2006.
- Olivella S, Carrera J, Gens A, Alonso, E. Nonisothermal multiphase flow of brine and gas through saline media. *Transport in Porous Media*, 1994;15(3):271–293. doi:10.1007/BF00613282
- Olivella S, Gens A, Carrera J, Alonso E. Numerical formulation for a simulator 'CODE_BRIGHT' for the coupled analysis of saline media. *Engng Comput.* 1996;13(7):87-112.
- Sanchez M & Gens A. FEBEX project: Final report on thermo-hydro-mechanical modelling, Technical Publication 05-2/2006. Madrid: Enresa.
- Toprak E, Olivella S, Pintado X. Modelling Engineered Barriers for Spent Nuclear Fuel Repository using a Double Structure Approach for Pellet based Components. *Environmental Geotechnics* 2018, 1-70.
- Villar MV. Thermo-hydro-mechanical characterisation of a bentonite from Cabo de Gata: A study applied to the use of bentonite as sealing material in high-level radioactive waste repositories, Technical Publication 01/2002. Madrid: Enresa.

MODELLING OF FIBER-REINFORCED CONCRETE AND APPLICATION CASE

I.P. Damians^{*}, S. Olivella^{*}, and C. Cots[†]

^{*} Department of Civil and Environmental Engineering
Universitat Politècnica de Catalunya – BarcelonaTech (UPC)
Campus Nord UPC, 08034 Barcelona, Spain
Email: ivan.puig@upc.edu

[†] BASF Construction Chemicals S.L.
Carretera del Medio 219, 08907 Hospitalet de Llobregat, Spain

Key words: Fiber-Reinforced Concrete, Shotcrete, Tunnel 3D Model

Abstract. *This report summarizes the first results of 2D and 3D finite element method numerical modelling analysis of fiber-reinforced concrete behaviour and a tunnel case study application. A porosity strength-dependant material model was assumed and preliminary calibrated to fit the mechanical performance of fiber-reinforced concrete stress and crack opening displacement measured results.*

1 INTRODUCTION

This extended abstract summarizes the methodology and first results of the 2D and 3D finite element (FE) modelling analysis of fiber-reinforced concrete behaviour. Fiber-reinforced concrete (both metallic and/or polymeric) is a worldwide extended construction technique for many precast concrete applications. For example, a proper fiber dosage may be capable to bear and avoid the concrete shrinkage cracks in particular cases, without needing additional steel-rebar installation. A preliminary case study is presented and methodology proposed to analyse the fiber-reinforced shotcrete application in tunnelling. A first attempt tunnel 3D modelling is presented as a case study in this report.

A porosity strength-dependant material model has been used to perform fiber-reinforced concrete behaviour and damage propagation^[1]. To calibrate the numerical model, measurements following the EN-14651 test^[2] were obtained with four different polyethylene fiber dosages. This European Standard specifies a method of measuring the flexural tensile strength of fibered concrete specimen and allows the determination of the limit of proportionality (LoP; which relates to the vertical load applied) and the crack mouth opening displacement (CMOD; which relates to the open gap evolution of the prescribed notch).

2 NUMERICAL MODEL

Figure 1a presents a test sample following the EN 14651, and Figure 1b presents the 2D plane strain FE model mesh generated (897 quadrilateral elements generating 961 nodes). As stated, a constitutive model which relates the porosity evolution to the tensile strength was considered to fit the fiber-reinforced concrete behaviour^[1]. This material model allows the performance of tensile strength loss after a certain value of material porosity is reached. Elastic-plastic behaviour with Drucker-Prager failure criterion was assumed, implemented with the porosity strength-dependant model in the EN-14651 case studies.

Table 1 presents the concrete material properties assumed to perform the EN-14651 tests. Main material properties of the further tunnelling case study are also given.

Table 1: Material properties: EN-14651 test and tunnel case study (main materials):

Parameters:	Main materials:					Units:
	Concrete (EN-14651)	Soil (Tunnel)	Shotcrete layers (Tunnel)	Truss beams (Tunnel)	Invert (Tunnel)	
Unit weight, γ	23.5	20.5	23.5	27.5	23.5	kN/m ³
Initial porosity, ϕ_0	0.145 ^(a)	0.250	0.145 ^(a)	0.001	0.145	-
Elastic modulus, E	30000	1000	25000 & 35000 ^(b)	210000	35000	MPa
Poisson's ratio, ν	0.15	0.30	0.15	0.30	0.15	-
Friction angle, ϕ	30 & 38 ^(c)	-	30	-	-	deg.
Dilatancy angle, ψ	30 & 38 ^(c)	-	30	-	-	deg.
Cohesion, c	200	-	200	-	-	kPa
Reference porosity, ϕ_{00} ^(d)	0.150	-	0.150	-	-	-
Porosity function, n ^(e)	50	-	50	-	-	-

Notes: ^(a) Assuming a solid particles density of $\gamma_s=27.5$ kN/m³, a concrete unit weight of $\gamma_c=23.5$ kN/m³ returns an initial porosity of $\phi=0.145$ ($\phi=(\gamma_s-\gamma_c)/\gamma_s$). ^(b) Different shotcrete layers were assumed: the first one to be installed just after the soil excavation and in contact with the soil, and the second one (stiffer) after installing the truss, in contact with the first concrete layer. ^(c) Two different cases are shown in this study in order to perform sensitivity analysis due to strength changes. ^(d) The reference porosity relates to the porosity value from where the tensile strength (cohesion) is zero. ^(e) The porosity function refers to the shape of the decreasing strength from the initial porosity to the reference porosity, i.e., n=1 (straight linearly decreasing); n=10 (smooth curve shape); n=100 (sharp curve decreasing). (For a deep explanation about the model see Reference ^[1])

a) EN-14651 test performance:



b) 2D FE model geometry:

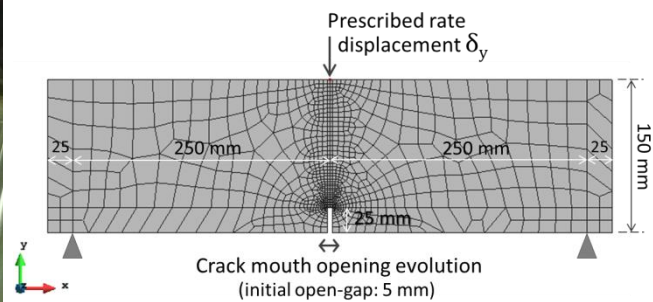
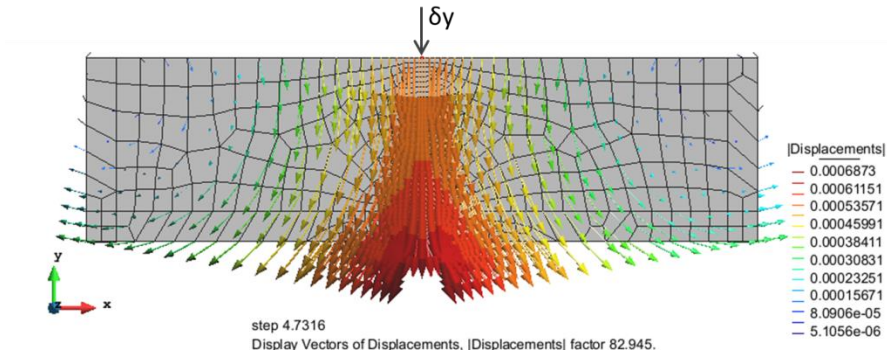


Figure 1: EN-14651 test (a) and 2D finite element model mesh detail (b).

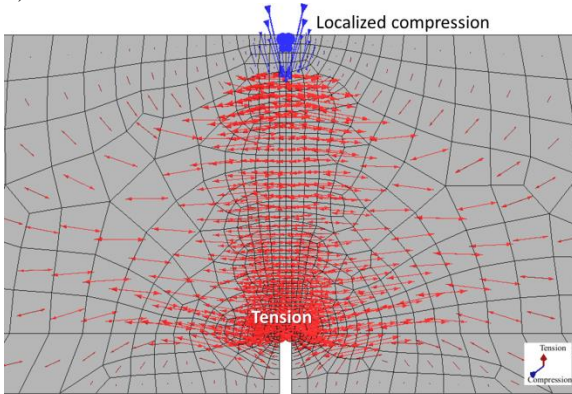
3 RESULTS

Figure 2 presents the EN-14651 modelled test displacement results, the inner stress development, and the plastic shear contour fields obtained. As shown, a clear zone location of the higher tension values was obtained at the notch's inner tip, where the deviatoric (shear) plastic strains arose. The material porosity changes achieved are shown in Figure 3a consequently related to the cohesion strength loss (Figure 3b). A zone without cohesion strength was obtained relating to crack propagation processes and damage emergence.

a) Vector displacements:



b) Main stress vectors detail:



c) Plastic shear contour field:

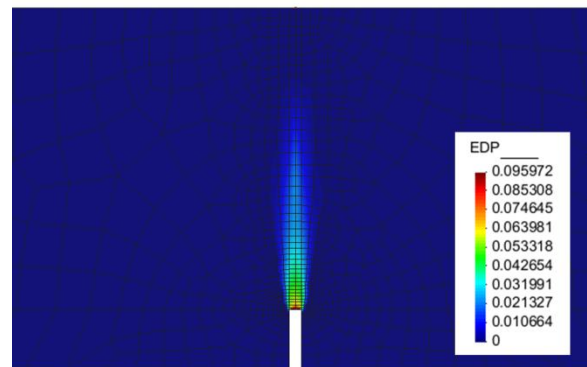
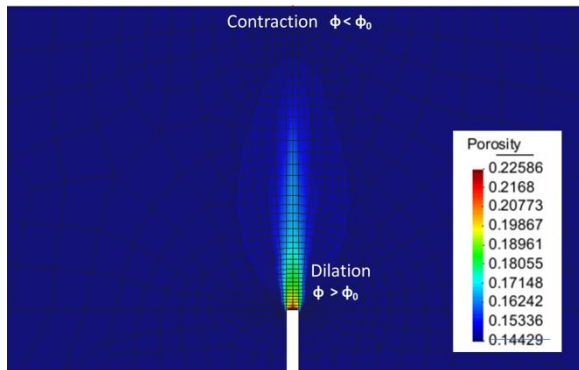


Figure 2: EN-14651 model results: displacement vectors (a), stress (b), and plastic shear shadings (c).

a) Porosity changes (damaged zone location):



b) Tensile strength - cohesion loss:

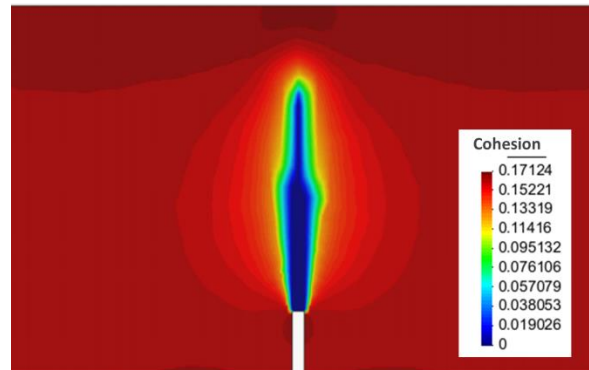


Figure 3: Porosity changes (a) and tensile strength loss (b).

In Figure 4a, plots from the horizontal stress changes at the notch's inner tip are given for two different concrete friction angle model assumptions ($\phi=30^\circ$ and 38°). Clear strength loss was obtained for both cases, with an expected higher peak horizontal stress values for the strengthened case. Figure 4b presents the comparison between the two modelled cases and four measured test cases with different polyethylene fibre dosage. The strength loss was clearly obtained, and a reasonable agreement between the calculated (2D model) and measured EN-14651 test response was achieved.

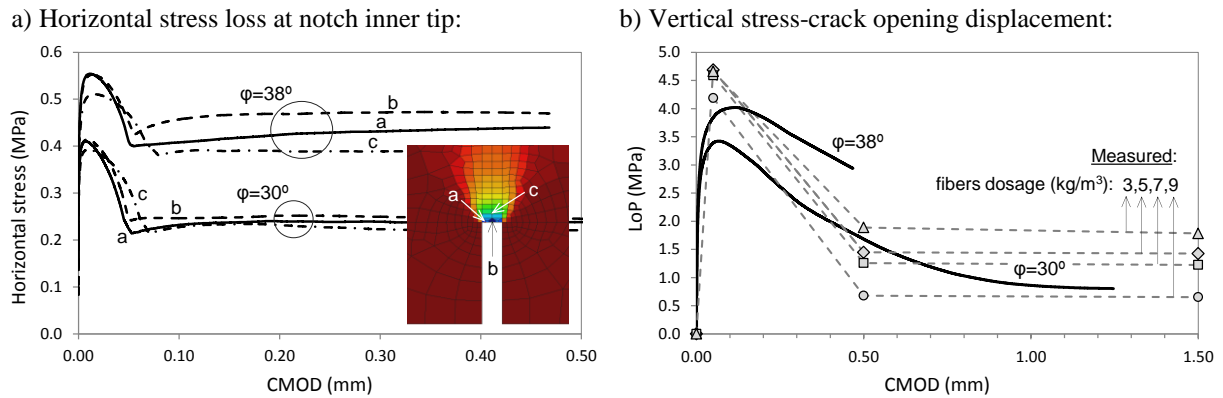


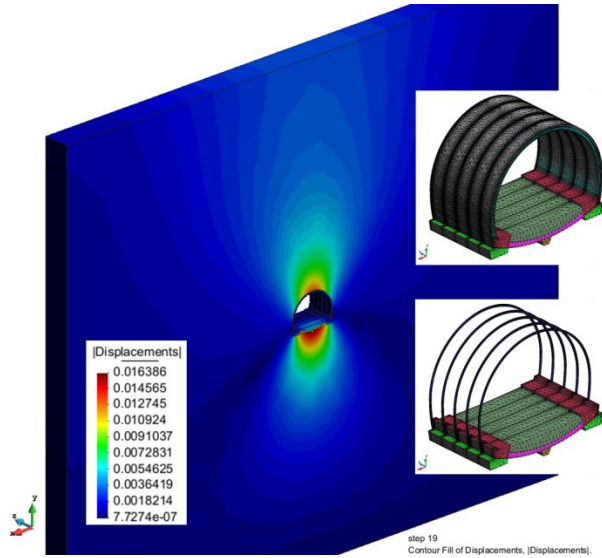
Figure 4: Horizontal stress loss (a) and Stress-displacement numerical-measured results comparison (b).

A preliminary tunnel application case was modelled and results at the end of construction (EoC) presented in Figure 5. The 3D numerical model was made with 541674 tetrahedral elements generating 94984 nodes. The modelled tunnel has about 12 m-diameter and 8 m-length, and assumed to be placed at about 70 m-depth. The model was calculated with a staged-construction considering step-by-step soil 1.6 m-thick-slice excavation and structural components installation through the tunnel axis. A first 0.2 m-thick shotcrete layer was considered to be installed after 1.6 m soil-slice excavation. 0.1 m-thick steel truss beams were then installed directly on the 1st shotcrete layer, performing a 1.5 m spacing distribution through the tunnel axis. After the underlying drain, invert construction and lateral concrete guide wall, a second shotcrete layer was finally projected surrounding the inner face of the tunnel. As previously specified (see Table 1), elastic-plastic model with Drucker-Prager failure criterion and porosity strength-dependant model was assumed for the shotcrete material zones, whereas the other components were assumed linear elastic (soil/ground, truss beams, invert, underlying drain, etc.). Further models with refined porosity strength-dependant and staged-construction are under the scope of the ongoing tasks.

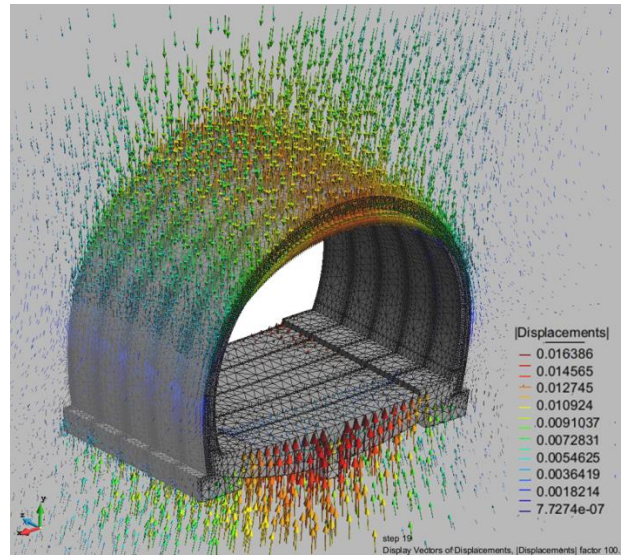
4 CONCLUSIONS

- A 2D numerical finite element modelling was generated to analyse the stress-crack opening displacement results of fiber-reinforced concrete samples.
- A constitutive elastic-plastic material model including a porosity strength-dependant fits the measured test data (EN-14651) in a reasonable manner, and seems promising to further analysis of fiber-reinforced concrete applications.
- A 3D model of a tunnel is presented considering material plasticity and porosity strength-dependant of two shotcrete layer materials. The assumed staged-construction model methodology resulted capable to achieve satisfactory results with the porosity strength-dependant mode implementation and allowing other real-case assumptions (geometry, structural data, different boundary conditions, etc.).

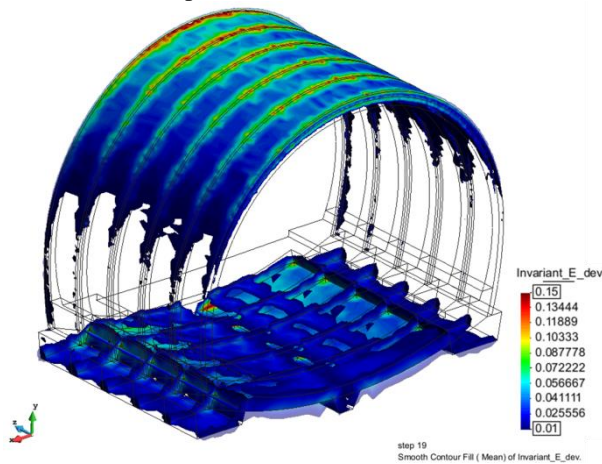
a) Global displacements and tunnel details:



b) Vector displacements at EoC:



c) Total (elastic+plastic) shear strains at EoC:



d) Plastic shear strains at EoC:

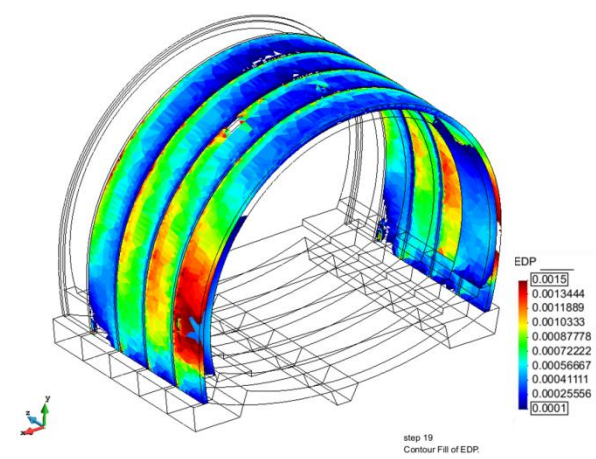


Figure 5: Tunnel 3D model results.

REFERENCES

- [1] Trabelsi H., Jamei M., Zenzri H., and Olivella S.; 2012. Crack patterns in clayey soils: Experiments and modeling. International Journal for Numerical and Analytical Methods in Geomechanics. Volume 36, Issue 11, Pages: 1410-1433.
- [2] EN 14651; 2005. Test method for metallic fibered concrete - Measuring the flexural tensile strength (limit of proportionality (LOP), residual). European Standard (EN), European Committee for Standardization (CEN/TC 229). Brussels, Belgium. June 2005.

MODELLING SPHERICAL GAS FLOW IN MX80 BENTONITE

I.P. Damians^{*}, S. Olivella^{*}, and A. Gens^{*}

^{*} Department of Civil and Environmental Engineering
Universitat Politècnica de Catalunya – BarcelonaTech (UPC)
Campus Nord UPC, 08034 Barcelona, Spain
Email: ivan.puig@upc.edu

Key words: HM 3D Model, Gas Flow, Mx80 Bentonite

Abstract. Gas injection tests performed on compact bentonite samples were carried out at the British Geological Survey. A 3D numerical model was developed to simulate the different gas injection test case studies and to achieve similar gas pressure, flow, and stress responses.

1 INTRODUCTION

A gas injection test performed on compacted Mx80 bentonite was carried out at the British Geological Survey. The experiment data for this study is analyzed by DECOVALEX Task A and reported in [1]. These tests are useful to increase the understanding of gas flow potential through these low permeability materials. With these tests it is possible to improve bentonite functionality (e.g., in nuclear waste repositories) and confirm its suitability to isolate spent fuel.

2 MATERIAL PROPERTIES AND NUMERICAL MODEL

To model the Mx80 Bentonite material behavior, embedded fracture permeability-cubic law model with a relative permeability as a function of saturation of matrix and saturation of fractures was implemented. Table 1 presents the material properties and Figure 1 presents the random intrinsic permeability distribution assumed at each model sample layer (2/3 weighting for higher permeability zone, and 1/6 weighting for lower permeability zones, which is related to the initial porosity). The mechanical elastic properties were defined by 307 MPa of Young's modulus and Poisson's ratio equal to 0.44. Plasticity was considered with a failure criterion parameters (Drucker Prager) defined by a friction angle of 10°, dilatancy angle equal to 1°, and 50 kPa of cohesion.

Table 1. Mx80 Bentonite material parameters for hydraulic properties heterogeneity:

Porosity, $\phi_0^{(a)}$	Intrinsic permeability, k_0	Associated spacing, a	Initial aperture, b_0	Maximum aperture, b_{max}	Water retention curve ^(b)		Gas/Liquid relative permeability, n_{α} -power ^(c)
					$P_{VG,0}$	λ_{VG}	
0.40	2.15×10^{-19}	2.0×10^{-5}		3.40×10^{-6}	37.80		
0.41	3.90×10^{-19}	9.5×10^{-6}	1.0×10^{-8}	2.66×10^{-6}	27.00	0.45	3 / 3
0.42	7.10×10^{-19}	5.0×10^{-6}		2.16×10^{-6}	19.44		
-	m^2	m	m	m	MPa	-	-

Notes: ^(a) Random porosity between 0.40, 0.41, and 0.42 with 1/6, 1/6, and 2/3 weighting each, respectively (see Figure 1); ^(b) Water retention curve according to Van Genuchten model (λ_{VG} : shape function); ^(c) relative permeability is a function of the degree of saturation: $k_{r\alpha} = (S_{\alpha})^n$.

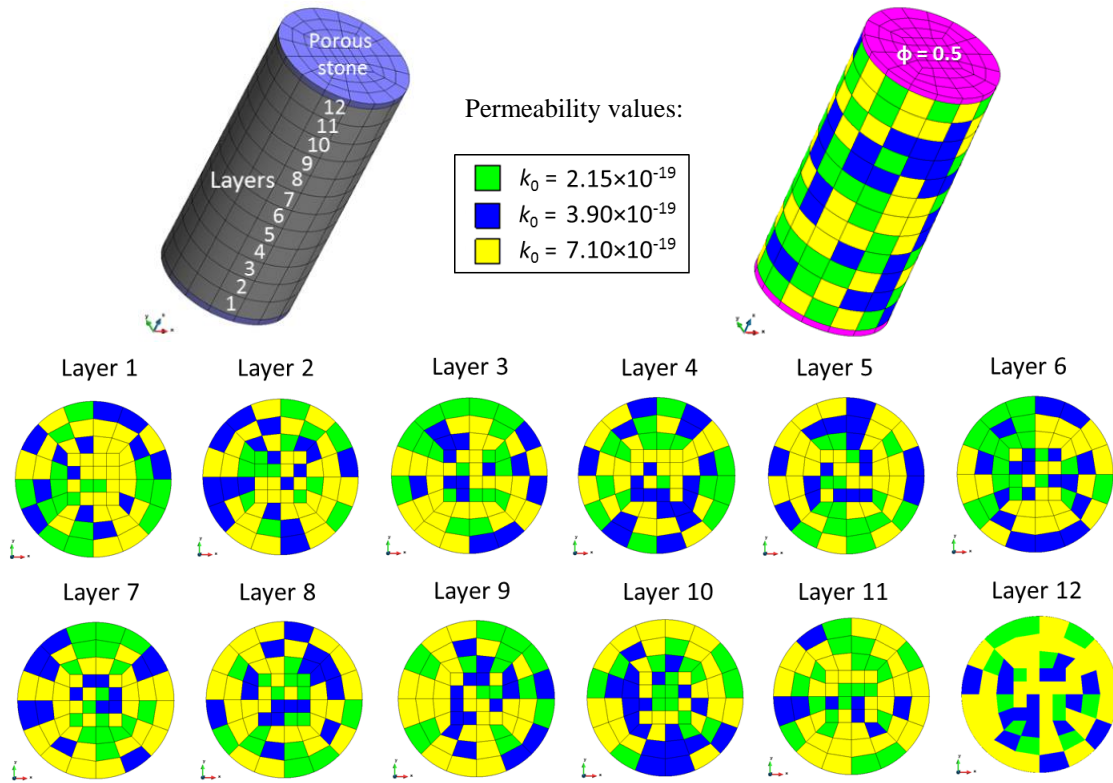
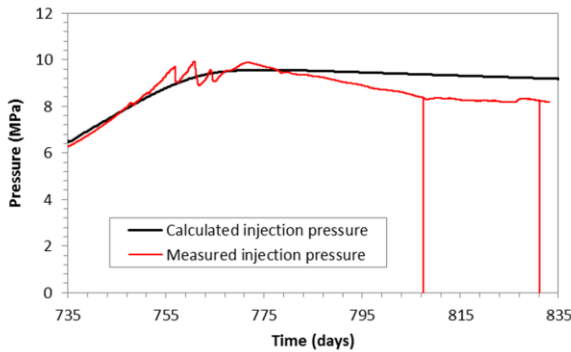


Figure 1: Layer-by-layer intrinsic permeability distribution assumed (2/3 weighting for higher permeability zone, and 1/6 weighting for lower permeability zones).

3 RESULTS

Comparison plots between the measured gas pressure and radial flow test results and calculated ones are presented in Figure 2. Figure 3 presents the gas pressure and advective gas flow results at 735 (beginning of the injection in the centre of the sample), 785 (after spherical breakthrough), and 835 days.

a) Gas pressure:



b) Radial flow (total):

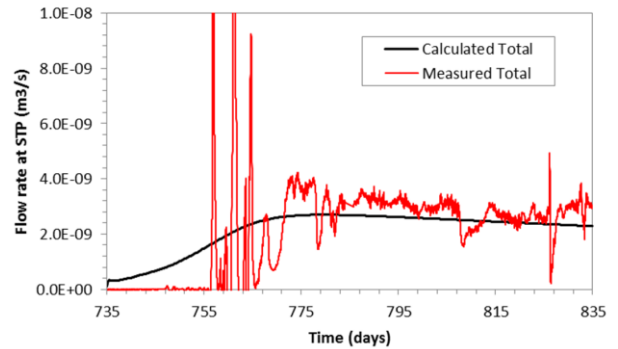


Figure 2: Gas pressure (a) and total radial flow (b) evolution results.

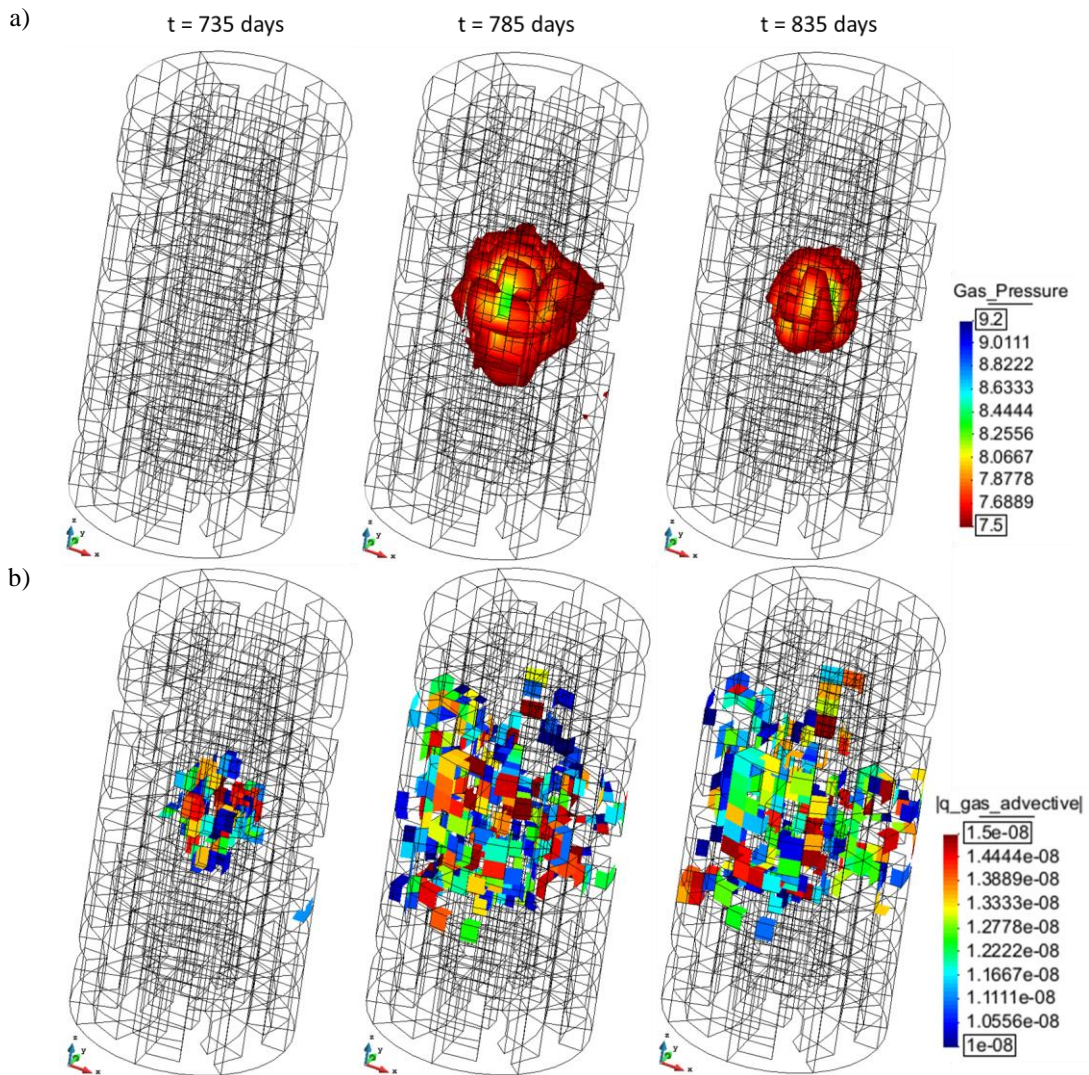


Figure 3: Gas pressure (a) and advective gas flux (b) results at 735, 785, and 835 days.

4 CONCLUSIONS

The proposed methodology provides reasonably satisfactory results. Agreement was achieved on the spherical flow test responses modelling the gas injection tests with an embedded fracture permeability-cubic law model assuming relative permeability as a function of saturation of matrix and fractures, and elastic-plastic mechanical features.

ACKNOWLEDGEMENTS

Support by the National Radioactive Waste Management Agency (ANDRA).

REFERENCE

- ^[1] Harrington J.F., Graham C.C., Cuss R.J., and Norris S.; 2017. Gas network development in a precompacted bentonite experiment: Evidence of generation and evolution. Applied Clay Science Journal, Volume 147. October 2017, pp. 80-89.

MODELING THE REACTIVATION OF A DUCTILE FAULT

Victor Vilarrasa^{*}, Roman Makhnenko[†] and Francesco Parisio^{††}

^{*} Institute of Environmental Assessment and Water Research (IDAEA)
Spanish National Research Council (CSIC)
Jordi Girona 18-26, 08034 Barcelona, Spain
Associated Unit: Hydrogeology Group UPC-CSIC
e-mail: victor.vilarrasa@idaea.csic.es, web page: h2ogeo.upc.edu/en/12-directorio-personal-ghs/539-victor-vilarrasa-4

[†] Department of Civil and Environmental Engineering (CEE)
Illinois University at Urbana-Champaign
2221 Newmark Civil Engineering Bldg, 61801 Urbana, Illinois, USA
e-mail: romanmax@illinois.edu, web page: <https://cee.illinois.edu/directory/profile/romanmax>

^{††} Department of Environmental Informatics
Helmholtz Centre for Environmental Research – GmbH - UFZ
Permoserstraße 15, 04318 Leipzig, Germany
e-mail: francesco.parisio@ufz.de

Key words: HM coupled analysis, Fluid injection, Induced seismicity, Geo-energies

Abstract. *Fluid injection at depth associated with geo-energy operations has significantly increased lately in an attempt to mitigate climate change. The downside is that the generated pressure buildup decreases the effective stresses, bringing the stress state towards rock yield conditions, which may induce significant seismicity. We investigate the effect of CO₂ injection on the stability of a ductile fault, formed by a clay-rich low-permeable core and a damage zone on both sides of the core, which properties vary depending on the rock with which the fault is in contact. Simulation results show that pressure buildup causes fault reactivation, leading to a progressive plastic strain accumulation that would induce multiple microseismic events, aseismic slip, or a combination of both.*

1 INTRODUCTION

Fluid injection into deep geological formations has significantly intensified as a result of an increasing interest in subsurface energy operationsⁱ. Most subsurface energy sources are carbon-free and they even have the potential to yield negative emissions if they are combined with CO₂ storage. Despite the potential of geo-energy operations to mitigate climate change, they are usually accompanied with high risks of triggering induced seismicity, which in some cases might reach magnitudes that provoke sensible effects on local population (for magnitudes M roughly larger than 2)ⁱⁱ and, in the worst cases, even create property and infrastructure damage. The negative consequences of such felt earthquakes may lead to the cancellation of projects, as has occurred at Basel, Switzerland, in an enhanced geothermal projectⁱⁱⁱ or at Castor, Spain, in a seasonal natural gas storage project^{iv}.

Felt induced seismicity is mainly nucleated in brittle crystalline basements^{v,vi}. Nevertheless, most fluid injection operations take place in sedimentary rocks that are significantly more permeable than the crystalline basement and exhibit higher ductility, especially if the clay content is high. As a result, the component of deformation generating seismic signals at sufficiently high frequency in sedimentary rocks is generally of low

magnitude ($M < 2$) and it cannot be felt on surface^{vii}, so it is termed induced microseismicity. Yet, felt earthquakes are also induced in operations that involve injection in sedimentary rocks^{viii}. This can be due to a series of reasons: (1) fluid is injected in the basal aquifer which is in direct contact with the crystalline basement and thus, pressurizes it^{ix}; (2) the presence of high-permeable faults that act as conduits connect the injection formation with the crystalline basement^x; and (3) poromechanical effects modify the stress state far away from the injection zone^{xi}. Thus, even though felt induced seismicity may be associated with fluid injection in sedimentary rocks, it usually remains nucleated at depth in the crystalline basement. In all cases, both in sedimentary rocks and in the crystalline basement, induced seismic events imply fault reactivation.

Modeling fault reactivation, both in brittle and ductile rock, is a challenging endeavor. In this study, we focus on modeling the reactivation of a ductile normal fault with a high clay content that intersects a sequence of reservoir and low-permeable formations. We simulate CO₂ injection, although the results are applicable for the injection of other fluids, e.g., water, wastewater and methane. We consider that the injection formation is hydraulically isolated from its surroundings because it lays between low-permeable clay-rich formations and it is bounded by the low-permeable fault.

2 METHODOLOGY

We model a geological system composed of a crystalline basement and two sequences of reservoir and low-permeable clay-rich formations (Figure 1). The whole system is crossed by a steep fault, with a dip of 60°, which has an offset of 25 m due to previous seismic slip. The fault core is assumed to be homogeneous along the whole fault. However, the damage zone varies depending on the rock the fault is in contact with. The top of the secondary aquifer is placed at 1.275 m deep. Laterally, the model extends 15 km on each side of the fault. A horizontal injection well is placed 1 km away from the fault. The problem is modelled in plane strain condition.

The initial conditions are hydrostatic fluid pressure, temperature of 60 °C, and a normal faulting stress regime with a vertical stress gradient of 23 MPa/km and the horizontal stresses equal to 0.69 times the vertical stress. The hydraulic boundary conditions are constant pressure on the outer boundaries and a CO₂ injection rate of 0.002 kg/s/m. The mechanical conditions are constant overburden equal to the lithostatic stress on the top boundary and no displacement perpendicular to the other boundaries.

To model reactivation of the clay-rich ductile fault, we assume elastoplastic behavior. Total strain tensor $\boldsymbol{\varepsilon}$ is decomposed into elastic and inelastic (or plastic) strain

$$d\boldsymbol{\varepsilon} = d\boldsymbol{\varepsilon}^e + d\boldsymbol{\varepsilon}^i, \quad (1)$$

where $\boldsymbol{\varepsilon}^e$ is the elastic strain tensor and $\boldsymbol{\varepsilon}^i$ is the plastic strain tensor. Inelastic deformation occurs when the stresses exceed a critical state at which the rock yields. This critical state is defined by a yield surface $F = 0$. Thus, only elastic deformation occurs when $F \leq 0$, and both elastic and plastic strains need to be considered when $F > 0$. We adopt a Drucker-Prager yield function

$$F = q - Mp' - c\beta, \quad (2)$$

where q is deviatoric stress, p' is mean effective stress and parameters M and β , for a normal faulting stress regime, are given by

$$M = \frac{6 \sin \phi'}{3 - \sin \phi'} \quad , \quad \beta = \frac{6 \cos \phi'}{3 - \sin \phi'} \quad , \quad (3)$$

where ϕ' is the internal friction angle and c the cohesion. To model plastic strain, we use a viscoplastic model available in CODE_BRIGHT, but assigning high values of the viscosity parameter Γ in order to obtain irreversible strain that is not time dependent, and which essentially depends on the yield criteria. The analogy between viscoplasticity and plasticity is obtained from

$$d\epsilon^i = \Gamma \langle \Phi(F) \rangle dt \frac{\partial G}{\partial \sigma'} = \Lambda \frac{\partial G}{\partial \sigma'} \quad , \quad (4)$$

where Λ is the plastic multiplier, t is time, $\Phi(F)$ is a stress function, σ' is the effective stress tensor, and G is the flow rule, which is given by

$$G = q - \alpha(Mp' + c\beta) \quad , \quad (5)$$

where α is a non-associativity parameter that can vary between 0 and 1. α equal to 0 indicates that there is no dilatancy, and α equal to 1 means that the flow rule is associated and gives dilatancy angle equal to the friction angle.

Finally, the stress function is given by a power law

$$\Phi(F) = F^m \quad , \quad (6)$$

where m is a constant.

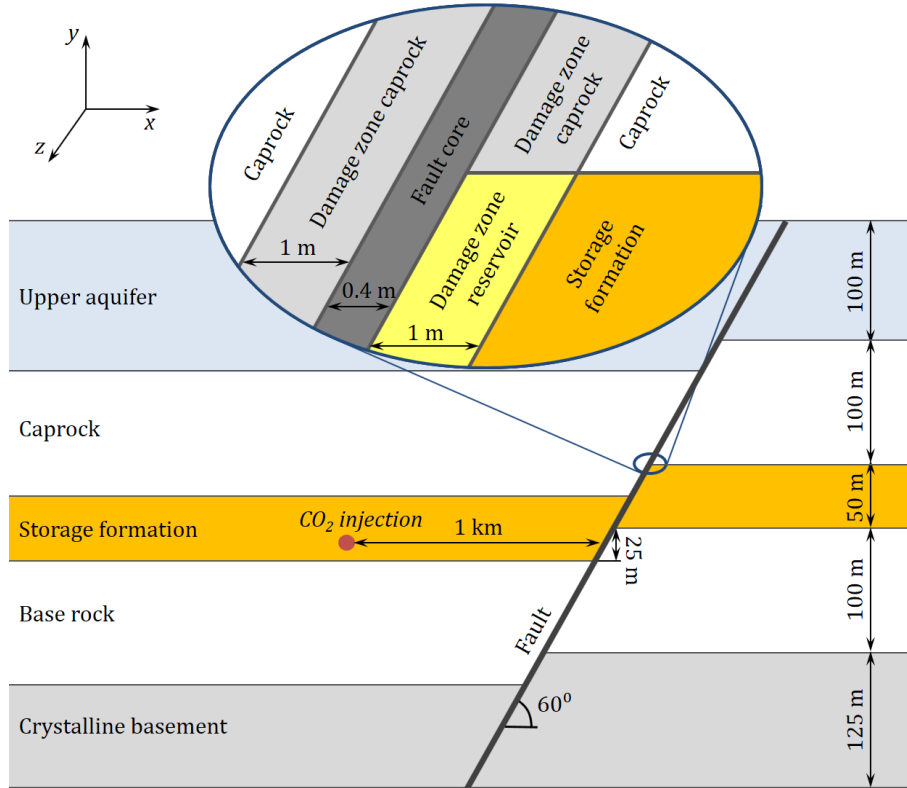


Figure 1. Schematic representation of the model geometry with the details on the fault structure that includes a fault core and a damage zone on both sides of the core that varies depending on the rock type the fault is in contact with.

Table 1 summarizes the rock properties of all the materials included in our model^{xiii}. We solve this hydro-mechanical coupled problem using CODE_BRIGHT^{xiii,xiv}, with the modifications made by Vilarrasa et al.^{xv} to model CO₂ injection.

Table 1. Hydro-mechanical properties of the geomaterials included in the model

Formation	Permeability, k (m ²)	Relative water permeability, k_{rw} (-)	Relative CO ₂ permeability, k_{rc} (-)	Entry pressure, p_0 (MPa)	van Genuchten shape parameter m (-)	Porosity, ϕ (-)	Young's modulus, E (GPa)	Poisson ratio, ν (-)	Cohesion, c (MPa)	Friction angle, ϕ' (°)
Storage formation	$4 \cdot 10^{-14}$	S_w^3	S_c^3	0.02	0.8	0.23	14	0.31	9	42
Caprock	$3 \cdot 10^{-21}$	S_w^6	S_c^6	1.5	0.3	0.05	2.8	0.40	6	24
Base rock	$2.5 \cdot 10^{-21}$	S_w^6	S_c^6	1.5	0.3	0.05	3.0	0.39	6	24
Upper aquifer	$1 \cdot 10^{-14}$	S_w^3	S_c^3	0.20	0.8	0.13	28	0.21	12	31
Crystalline basement	$4 \cdot 10^{-20}$	S_w^6	S_c^6	12.0	0.3	0.01	55	0.18	60	30
Fault core	$1 \cdot 10^{-19}$	S_w^6	S_c^6	4.0	0.3	0.10	1.0	0.30	0	24
Damage zone reservoirs	$2 \cdot 10^{-13}$	S_w^3	S_c^3	0.02	0.8	0.25	7.0	0.35	0	30
Damage zone confinement layers	$1.5 \cdot 10^{-19}$	S_w^6	S_c^6	5.0	0.3	0.09	1.4	0.42	0	24
Damage zone basement	$1 \cdot 10^{-16}$	S_w^4	S_c^4	1.0	0.5	0.07	42	0.30	0	30

3 RESULTS

CO₂ injection causes pressure buildup that reduces the mean effective stress, bringing the stress state towards the yield surface (Figure 2a). After 35 days of injection, the yield condition is reached within the fault and inelastic strains are generated (Figure 2b). Instead of a sudden, sharp shear slip which would induce a large earthquake, plastic strain is progressive. Thus, reactivation of a ductile fault induces a sequence of microseismic events, aseismic slip, or a combination of both^{xvi}.

Figure 3 displays the distribution of the plastic strain after half a year of CO₂ injection. Overall, 20 m of the fault in contact with the lower half of the storage formation are reactivated. Assuming that the fault undergoes failure conditions all along the length of the horizontal well, the cumulative magnitude of the microseismic events is estimated to be $M = 1.7$ for a 2 km long well^{xvii}. In this case, the low-permeability of the fault hinders fluid pressure propagation away from the storage formation and thus, the crystalline basement does not become critically stressed.

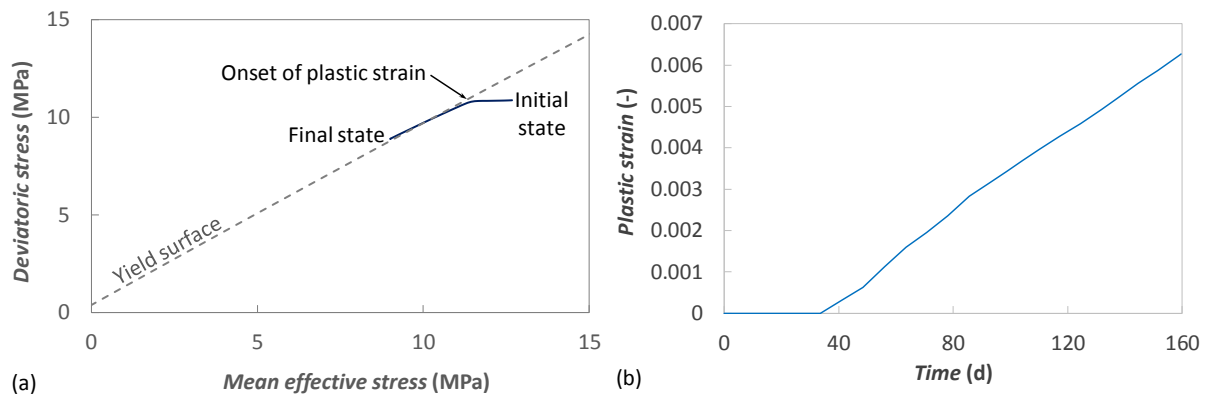


Figure 2. (a) Stress path in the deviatoric stress - mean effective stress plane (from Vilarrasa et al., 2017) and (b) plastic strain evolution in the fault core, at a point placed 7 m above the bottom of the reservoir (from Vilarrasa and Makhnenko^{xviii})

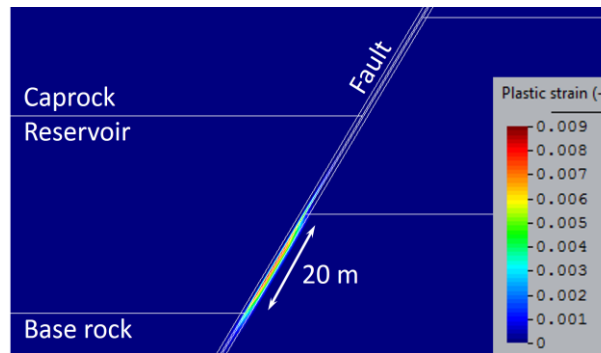


Figure 3. Plastic strain distribution after half a year of CO₂ injection (modified from Vilarrasa et al.^{xvii})

4 CONCLUSIONS

We have modeled the reactivation of a ductile fault as a result of CO₂ injection with CODE_BRIGHT. Clay-rich faults can be of low strength, and thus, may be reactivated at relatively low pressure buildup. The reactivation of a ductile fault may give rise to a sequence of microseismic events, aseismic slip, or a combination of both. Thus, the seismic risk remains low because of their ductility. However, it is extremely important to measure the in situ stress state and fault properties to evaluate the maximum sustainable injection pressure. Proper characterization and modeling of rock behavior allows for estimation of the likelihood of the crystalline basement becoming critically stressed as a result of pore pressure or stress changes and induced large earthquakes.

ACKNOWLEDGMENTS

VV would like to acknowledge financial support from the EU Project “FracRisk” (European Community's Horizon 2020 Framework Programme H2020-EU.3.3.2.3 under grant agreement n 640979).

REFERENCES

[i] McCartney, J.S., M. Sanchez, I. Tomac, 2016. Energy geotechnics: Advances in

-
- subsurface energy recovery, storage, exchange, and waste management. *Computers and Geotechnics*, 75, 244-256.
- [ii] Rutqvist, J., A.P. Rinaldi, F. Cappa, P. Jeanne, A. Mazzoldi, L. Urpi, Y. Guglielmi, V. Vilarrasa, 2016. Fault activation and induced seismicity in geological carbon storage—Lessons learned from recent modeling studies. *Journal of Rock Mechanics and Geotechnical Engineering*, 8(6), 789-804.
- [iii] Häring, M.O., U. Schanz, F. Ladner, B.C. Dyer, 2008. Characterisation of the Basel 1 enhanced geothermal system. *Geothermics*, 37(5), 469-495.
- [iv] Gaite, B., A. Ugalde, A. Villaseñor, E. Blanch, 2016. Improving the location of induced earthquakes associated with an underground gas storage in the Gulf of Valencia (Spain). *Physics of the Earth and Planetary Interiors*, 254, 46-59.
- [v] Verdon, J.P., 2014. Significance for secure CO₂ storage of earthquakes induced by fluid injection. *Environmental Research Letters*, 9(6), 064022.
- [vi] Vilarrasa, V., J. Carrera, 2015. Geologic carbon storage is unlikely to trigger large earthquakes and reactivate faults through which CO₂ could leak. *Proceedings of the National Academy of Sciences*, 112(19), 5938-5943.
- [vii] Phillips, WS, J.T. Rutledge, L.S. House, M.C. Fehler (2002). Induced microearthquake patterns in hydrocarbon and geothermal reservoirs: Six case studies. In *The mechanism of induced seismicity* (pp. 345-369). Birkhäuser, Basel.
- [viii] Ellsworth, W.L., 2013. Injection-induced earthquakes. *Science*, 341(6142), 1225942.
- [ix] Keranen, K.M., H.M. Savage, G.A. Abers, E.S. Cochran, 2013. Potentially induced earthquakes in Oklahoma, USA: Links between wastewater injection and the 2011 Mw 5.7 earthquake sequence. *Geology*, 41(6), 699-702.
- [x] Zhang, Y., M. Person, J. Rupp, K. Ellett, M.A. Celia, C.W. Gable, ..., T. Dewers, 2013. Hydrogeologic controls on induced seismicity in crystalline basement rocks due to fluid injection into basal reservoirs. *Groundwater*, 51(4), 525-538.
- [xi] Segall, P., S. Lu, 2015. Injection-induced seismicity: Poroelastic and earthquake nucleation effects. *Journal of Geophysical Research: Solid Earth*, 120(7), 5082-5103.
- [xii] Vilarrasa, V., R. Makhnenko, S. Gheibi, 2016. Geomechanical analysis of the influence of CO₂ injection location on fault stability. *Journal of Rock Mechanics and Geotechnical Engineering*, 8(6), 805-818.
- [xiii] Olivella, S., J. Carrera, A. Gens, E. E. Alonso, 1994. Non-isothermal Multiphase Flow of Brine and Gas through Saline media. *Transport in Porous Media*, 15, 271-293
- [xiv] Olivella, S., A. Gens, J. Carrera, E. E. Alonso, 1996. Numerical Formulation for a Simulator (CODE_BRIGHT) for the Coupled Analysis of Saline Media. *Engineering Computations*, 13(7), 87-112
- [xv] Vilarrasa, V., O. Silva, J. Carrera, S. Olivella, 2013. Liquid CO₂ injection for geological storage in deep saline aquifers. *International Journal of Greenhouse Gas Control*, 14, 84-96.
- [xvi] Lengliné, O., J.E. Elkhoury, G. Daniel, J. Schmittbuhl, R. Toussaint, J.P. Ampuero, M. Bouchon, 2012. Interplay of seismic and aseismic deformations during earthquake swarms: An experimental approach. *Earth and Planetary Science Letters*, 331, 215-223.
- [xvii] Vilarrasa, V., R. Makhnenko, L. Laloui, 2017. Potential for Fault Reactivation due to CO₂ Injection in a Semi-Closed Saline Aquifer. *Energy Procedia*, 114, 3282-3290.
- [xviii] Vilarrasa, V., R. Makhnenko, 2017. Caprock integrity and induced seismicity from laboratory and numerical experiments. *Energy Procedia*, 125, 494-503.

THERMO-HYDRO-MECHANICAL SIMULATION OF GAS INJECTION INTO FRACTURED MEDIA

Ahmad Zareidarmiyan^{a,b}, Hossein Salarirad^a, Victor Vilarrasa^b, and Sebastia Olivella^c

^a Department of Mining and Metallurgical Engineering
Amirkabir University of Technology - Tehran Polytechnic (AUT), Tehran, Iran
E-mail: ahmad.zarei@aut.ac.ir

^b Institute of Environmental Assessment and Water Research (IDAEA),
Spanish National Research Council (CSIC)
C/ Jordi Girona 18-26, 08034 Barcelona, Spain
Associated Unit: Hydrogeology Group UPC-CSIC

^c Department of Civil and Environmental Engineering
Technical University of Catalonia (UPC-BarcelonaTech)
Campus Nord UPC, 08034 Barcelona, Spain

Keywords: THM Coupled Analysis, Enhanced Oil Recovery (EOR), Caprock Integrity, CODE_BRIGHT

Abstract. *This contribution describes the thermo-hydro-mechanical (THM) simulation of gas injection as an enhanced oil recovery (EOR) method for improving oil production efficiency in fractured oil reservoirs. Gas migrates through predefined discontinuities with stress-dependent permeability. The aperture of these discrete fractures controls permeability and capillary pressure variations. Thus, the model handles the combined THM effects of two-phase (gas and liquid) flow and permeability changes induced by deformation.*

1 INTRODUCTION

Utilization of the subsurface by different energy-related activities, such as Improved Oil Recovery (IOR), Geological Carbon Storage (GCS), and Enhanced Geothermal Systems (EGS), implies fluid injection that leads to multi-phase flow and thermo-hydro-mechanical (THM) processes which may compromise the rock mechanical stability and trigger micro-seismic events^{1,2}. To simplify an already complex coupled simulation, geological media is usually considered as a continuous porous media. However, deep geological formations are fractured.

How to treat fractures in numerical models is a debatable issue because their behavior dominates production and injection activities. Indeed, fractures have a significant effect on reservoir fluid flow as a result of changes in reservoir permeability, porosity, and their anisotropic behavior. These changes are strongly affected by variations in pore pressure, temperature, saturation, and effective stress (reservoir deformation). Based on the classification

proposed by Nelson³, four basic types of reservoir fractures can be defined as those that: (1) provide the essential porosity and permeability to the reservoir, (2) provide the essential permeability, (3) provide a permeability assist to an already producible reservoir, (4) impart no positive reservoir quality but create strong reservoir anisotropy and inhomogeneity.

Focusing on hydrocarbon reservoirs, studies have shown that a considerable amount of fossil fuel reserves, over 60% of the conventional oil and 50% of the gas reserves, are found in carbonate rocks which are naturally fractured⁴. Considering naturally fractured reservoirs (NFRs) as an equivalent continuous porous media and neglecting the impact of fractures on both flow and deformation, which is the usual approach, may be a non-reasonable assumption in some cases such as in carbonate oil reservoirs^{3,5}.

The goal of this study is to show the capability of CODE_BRIGHT to explicitly include fractures in deep geological media. To this end, we model a portion of a NFR, including two fractures that cross. We simulate injection of gas at a colder temperature than that of the rock and show the coupled THM response.

2 METHODS

2.1 Geometry

We consider a model that represents a $50 \times 50 \text{ m}^2$ portion of a reservoir that is initially saturated with water (Fig. 1). The top of the reservoir is located at a depth of 1000m. Two fractures with angles of 60° and -30° are embedded into the reservoir matrix. The fractures are treated as an equivalent porous media using the concept of embedded fractures⁶. The initial conditions correspond to hydrostatic pressure, a geothermal gradient of $33^\circ\text{C}/\text{km}$ with a surface temperature of 25°C and lithostatic stress. The considered stress regime is such that the vertical stress is greater than the horizontal stresses following the relationship $\sigma_h = 0.68\sigma_v$.

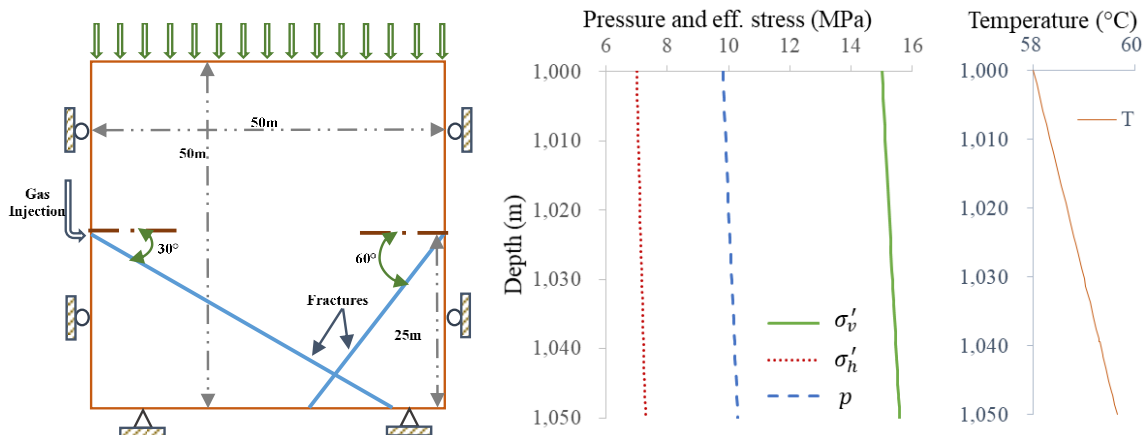


Figure 1: Schematic representation of the model geometry and initial conditions.

The mechanical boundary conditions are the lithostatic stress on the upper boundary, no displacement normal to the lateral boundaries and fixed displacement on the lower boundary. Gas is injected on the left boundary throughout the entire thickness (0.1m) of the sub-horizontal

fracture at a constant overpressure of 6 MPa and temperature of 35 °C (Fig. 1). We also perform an isothermal simulation to quantify the effect of cooling. The properties of the materials are shown in Table 1.

Table 1: Material properties used in the THM model

Property	Reservoir	Fracture
Rock density, ρ (kg/m ³)	2400	2300
Young's modulus, E (MPa)	4500	400
Poisson ratio, ν (-)	0.27	0.27
Porosity, ϕ (-)	0.1	0.1
Permeability, k (m ²)	10 ⁻¹⁷	10 ⁻¹⁴
Initial aperture, b_0 (m)	-	10 ⁻⁵
Maximum aperture, b_{Max} (m)	-	10 ⁻⁴
Thermal expansion coefficient, α_T (1/°C)	3×10 ⁻⁵	10 ⁻⁵
Thermal conductivity, λ (W/m·K)	2	2
Specific heat capacity, c_p (J/kg·K)	1000	1000

2.2 Fluid mechanics

Cold gas injection causes fluid pressure to increase and temperature to decrease, thus changing the effective stresses and producing deformations that exert an influence on the evolution of fluid pressure.

Fluid flow through fractures is governed by Darcy's law⁶

$$\mathbf{q}_\alpha = -\frac{kk_{r\alpha}}{\mu_\alpha}(\nabla p_\alpha + \rho_\alpha g \nabla z), \quad (1)$$

where \mathbf{q}_α (m/s) is the α -phase volumetric flux, k (m²) is intrinsic permeability, $k_{r\alpha}$ (-) is the relative permeability of α -phase, ρ_α (kg/m³) and μ_α (Pa.s) are the density and viscosity of α -phase, g (m/s²) is gravity, p_α (Pa) is α -phase pressure and α can be either w, water, or g, gas.

Considering a planar fracture, the intrinsic permeability can be calculated as⁶

$$k_f = \frac{b^2}{12}, \quad (2)$$

where b is the aperture of the fracture.

When a set of n fractures is included in a finite element, the equivalent intrinsic permeability of the element in the direction parallel to the fractures can be calculated as⁶

$$k \cong k_{matrix} + \frac{b^3}{12a}, \quad (3)$$

where k_{matrix} (m²) is the reference intrinsic permeability of the fracture matrix, that is, when the fractures are closed, and a is the spacing between fractures. The change in the intrinsic permeability of the matrix (porous media) can be derived by Kozeny-Carman formula⁷⁻⁹

$$k_{matrix} = k_0 \frac{\varphi^3}{(1-\varphi)^2} \frac{(1-\varphi_0)^2}{\varphi_0^3}, \quad (4)$$

where φ (-) is porosity and φ_0 (-) is the reference porosity.

The aperture of the fracture can be estimated as a function of deformation as⁶

$$b = b_0 + \Delta b = b_0 + a(\varepsilon - \varepsilon_0), \quad (5)$$

where ε is volumetric strain and ε_0 is the threshold value for volumetric strain above which fractures open up.

Considering both Equations (3) and (4), it can be seen that the element permeability depends on the fracture spacing (a), which is a characteristic size of the material, but it is independent of the element size (s). Here, we consider one fracture in each element ($a = s$). When a fracture is open, the flow rate per unit length is given by the cubic law^{10,11}

$$Q = -\frac{b^3}{12\mu_\alpha}(\nabla p_\alpha + \rho_\alpha g \nabla z). \quad (6)$$

2.3 Geomechanics

We assume the rock deforms elastically, so deformation is reversible. To assess fracture stability, we adopt the Drucker-Prager yield function (F) as the yield criteria

$$F = q - Mp' - c\beta, \quad (7)$$

where q is deviatoric stress, p' is the mean effective stress, and c is cohesion. Parameters M and β depend, assuming that the Mohr-Coulomb failure criteria is circumscribing the Drucker-Prager failure criteria and assuming tri-axial compression, i.e., $\sigma_1 > \sigma_2 = \sigma_3$, are given by

$$M = \frac{6\sin\varnothing'}{3-\sin\varnothing'}, \beta = \frac{6\cos\varnothing'}{3-\sin\varnothing'}, \quad (8)$$

where \varnothing' is the internal friction angle. While $F < 0$ denotes elastic behavior, $F \geq 0$ implies both elastic and plastic strain.

4 RESULTS

Gas injection causes fluid pressure to increase and temperature to drop, thus reducing the effective stresses (Fig. 2a) and producing deformation. Such deformation, in turn, causes permeability changes (by more than one order of magnitude) (Fig. 2b) that modify fluid pressure. These effective stress changes lead to failure conditions at the injection point after 1 day of injection (Fig. 3). In contrast, the Mohr circle does not become tangent to the failure envelope at the intersection between the two fractures. Thus, the fracture may only be reactivated close to the injection point.

This behavior can also be observed in the $q - p'$ plane (Fig. 4a). Prior to injection, the reservoir is stable and far from the plastic regime. Once injection begins, the mean effective stress reduces more sharply than the deviatoric stress and the yield envelope is rapidly reached at the injection point. At this point, the rock begins to behave plastically. Strain occurs plastically for nearly one day. Then, the deviatoric stress decreases while the mean effective stress remains practically constant and the injection point ceases to plastify. Note that failure conditions are only reached when the fluid is injected cold. Therefore, the induced thermal stress reduction plays an important role in fracture stability.

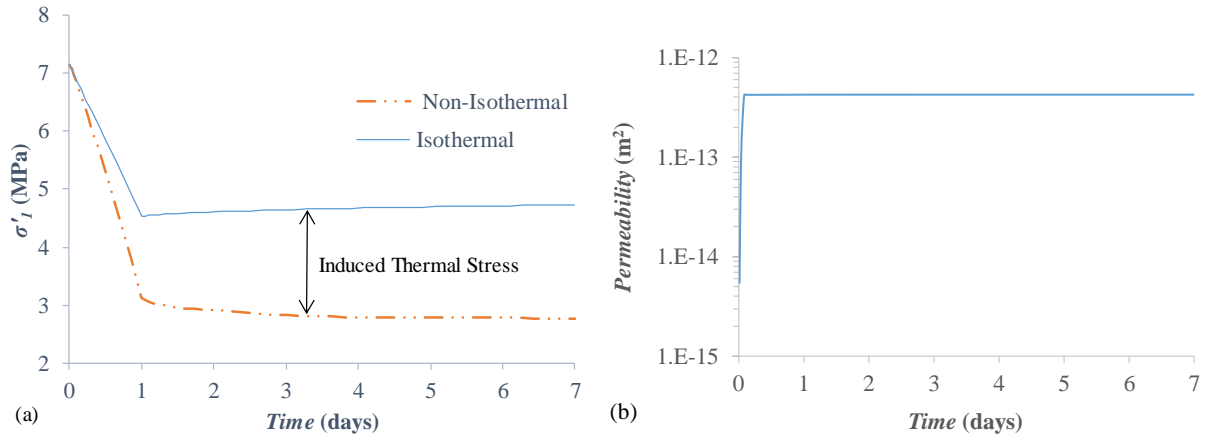


Figure 2: (a) Maximum principal stress evolution, indicating the thermal effect, and (b) fracture permeability evolution at the injection point.

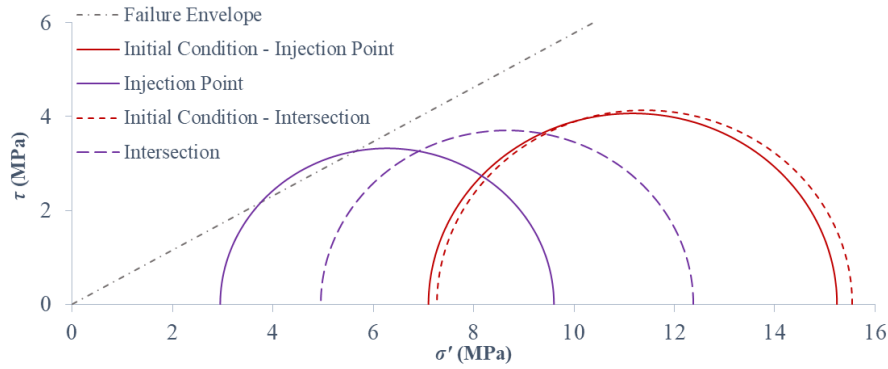


Figure 3: Mohr circles at the initial state and after 1 day of injection.

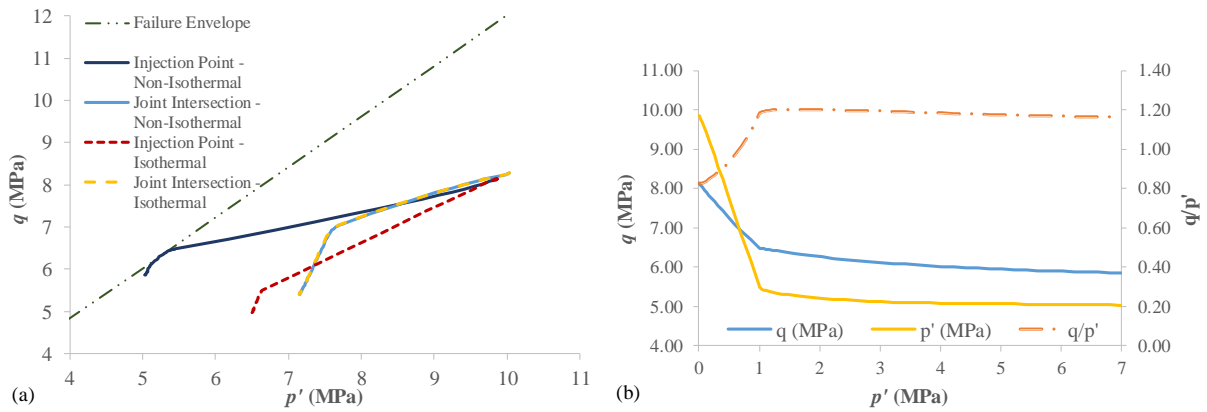


Figure 4: (a) $q - p'$ trajectory of injection point and fractures intersection point for a 1-week injection, and (b) mean effective and deviatoric stresses evolution at the injection point.

CONCLUSIONS

We have conducted simulations of cold gas injection into a fractured reservoir to study the

risk of mechanical failure. The specific scenario we model is meant to reflect a small part of a real naturally fractured reservoir. Additionally, we assume the geomaterials to be elastic and potential failure is evaluated by considering the Drucker-Prager criteria. We find that fracture instability is caused by the combined effect of fluid pressure buildup and cooling, which induces thermal stress reduction. For the assumed pressure buildup, i.e., 6 MPa, and cooling, i.e., 35°C, a ratio $\sigma_h > 0.68\sigma_v$ does not lead to shear failure of the fracture at the injection point.

6 ACKNOWLEDGMENTS

The first author acknowledges the financial support received from the “Iran’s Ministry of Science, Research and Technology” (Ph.D. students sabbatical grants). VV would like to acknowledge financial support from the EU Project “FracRisk” (European Community's Horizon 2020 Framework Programme H2020-EU.3.3.2.3 under grant agreement n 640979).

7 REFERENCES

1. Rutqvist J, Rinaldi AP, Cappa F, Jeanne P, Mazzoldi A, Urpi L, Guglielmi Y, Vilarrasa V. Fault activation and induced seismicity in geological carbon storage – Lessons learned from recent modeling studies. *J Rock Mech Geotech Eng*. 2016;8(6):789-804.
2. De Simone S, Vilarrasa V, Carrera J, Alcolea A, Meier P. Thermal coupling may control mechanical stability of geothermal reservoirs during cold water injection. *Phys Chem Earth*. 2013;64:117-126.
3. Nelson RA. *Geologic Analysis of Naturally Fractured Reservoirs*. Gulf Professional Pub; 2001.
4. Schlumberger. Carbonate Reservoirs: Meeting Unique Challenges to Maximize Recovery. *Schlumberger Mark Anal*. 2007;1:1-12.
5. Narr W, Schechter DS, Thompson LB. *Naturally Fractured Reservoir Characterization*. Society of Petroleum Engineers; 2006. <http://store.spe.org/Naturally-Fractured-Reservoir-Characterization-P40.aspx>. Accessed January 12, 2018.
6. Olivella S, Alonso EE. Gas flow through clay barriers. *Géotechnique*. 2008;58(3):157-176.
7. Kozeny J. Über kapillare leitung der wasser in boden. *R Acad Sci Vienna, Proc Cl I*. 1927;136:271-306.
8. Carman PC. Flow of Gases Through Porous Material. 1956.
9. Carrier WD. Goodbye, Hazen; Hello, Kozeny-Carman. *J Geotech Geoenvironmental Eng*. 2003;129(11):1054-1056.
10. Witherspoon PA, Amick CH, Gale JE, Iwai K. Observations of a potential size effect in experimental determination of the hydraulic properties of fractures. *Water Resour Res*. 1979;15(5):1142-1146.
11. Witherspoon PA, Wang JSY, Iwai K, Gale JE. Validity of Cubic Law for fluid flow in a deformable rock fracture. *Water Resour Res*. 1980;16(6):1016-1024.

TH MODELLING OF METHANE HYDRATE PHASE CHANGE IN MARINE SEDIMENTS

M. De La Fuente^{1,3}, J. Vaunat², H. Marín-Moreno³

¹National Oceanography Centre, University of Southampton, European Way, Southampton, SO14 3ZH, United Kingdom.

Email: mdlf1g15@soton.ac.uk

²Department of Civil and Environmental Engineering, Universitat Politècnica de Catalunya, Barcelona, Spain.

³National Oceanography Centre, University of Southampton Waterfront Campus, European Way, Southampton SO14 3ZH, United Kingdom.

Key words: Methane Hydrate-Bearing sediments, Hydrate dissociation, THM coupled analysis, GiD interface.

Abstract. *Methane hydrate-bearing sediments are geologic systems characterized by a large number of interdependent physical phenomena, including exothermic formation and endothermic dissociation of hydrate and ice phases, geomechanical deformation, variations in the hydraulic and geomechanical properties and non-isothermal multi-phase, multi-component flows. The numerical modelling of these systems require robust and efficient mathematical models capable of capturing the aforementioned interdependencies in a coupled manner. These models need to account for the heat and mass balance equations of each component of the system as well as for the restrictions and constitutive laws that reproduce the phenomenology of heat and fluid flows, phase change conditions and geomechanical response. This paper presents a new numerical model for the solution of the coupled hydro-thermal flow behavior of methane hydrate-bearing sediments subjected to hydrate dissociation and reformation.*

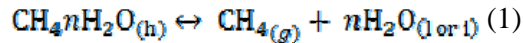
1 INTRODUCTION

Methane hydrate-bearing sediments (MHBS) play a major role as future energy supply (Krey et al., 2009; Muradov 2013), but also a major hazard for drilling and gas production (Collett et al., 2009), global climate change (Archer, 2007; Minshull et al., 2016) and seafloor instability (Sultan et.al., 2004; Nixon and Grozic, 2007). Despite the promising contribution of hydrates as a future energy source, their safe, cost-efficient and environmentally friendly extraction still faces technical difficulties, which encompasses not only the scientific aspects but also political, economic and societal implications (Boswell et al., 2017). At field-scale scale, MHBS may destabilize spontaneously as part of geological processes, unavoidably during petroleum drilling-production operations or intentionally as part of gas extraction from the hydrate itself. During dissociation, solid hydrate dissociates into its gas and water components triggering uncontrolled release of gas and drastic changes in the mechanical properties of the sediment. These phenomena pose one of the major technical risks for offshore oil and gas industry within hydrate production scenarios.

The experimental study to comprehend the behavior of MHBS has been hindered by the low solubility of methane in water, the high economic cost of field-scale trials and the inherent sampling difficulties associated with the thermodynamic stability of the sediment during core extraction. This situation has prompted key developments in numerical modelling to predict their behavior. For many years, hydrate simulation has focused on evaluating the productivity of methane extraction from in-situ sediments. As a result, several coupled fluid-thermal flow and thermo-hydro-mechanical (THM) numerical simulators have been developed (e.g., Rutqvist & Moridis (2008), Kimoto et al. (2010), Uchida (2012), Klar et.al. (2013), Sánchez & Gai (2016)). This paper describes a new TH formulation for MHBS that can be used for scientific and engineering analysis of the geomechanical stability of hydrate reservoirs. Our formulation has been implemented in the finite element simulator CODEBRIGHT (Olivella et al., 1996) extending its modelling capabilities for hydrate systems in deformable porous and fractured media. The following section describes the theoretical framework and develop the mathematical formulation of the model. Next, the capability of the model at predicting the thermo-hydraulic response of a reservoir during hydrate phase change is analysed.

2 THEORETICAL FRAMEWORK AND MATHEMATICAL FORMULATION

Gas hydrates are solid ice-like crystalline compounds that naturally form under low temperature and high pressure conditions as a combination of gas and water molecules. Of particular interest are methane hydrates (MH) in which the guest gas is a hydrocarbon. Under suitable thermodynamic conditions, methane gas reacts with water molecules to form MH according to:



These compounds are massively concentrated in deep-sea sediments, marine slopes and permafrost regions where the thermodynamic conditions for their stability are easily satisfied (Kvenvolden, 1988; Max and Johnson, 2016). Within the reservoir, their chemical stability is highly dependent on changes in the thermodynamic conditions (pressure and temperature of the system) and the pore water chemistry (water-soluble components). For instance, a rise in temperature, a drop in pressure or an increase in soluble inhibitors, such as salt, may lead to hydrate breakdown into its forming components.

2.1 Components and phases

To fully describe MHBS systems, the problem is formulated in a multi-component and multi-phase approach (Figure 2). We consider a granular porous media composed by four mass components: methane (m), water (w), grains (gr) and salt (st), which can be partitioned among five possible phases: gaseous (g), aqueous (l), hydrate (h), ice (i) and solid (s). The sand grains are assumed to form a solid continuum, which provides the deformable skeletal structure to the porous medium. Hydrate and ice can grow within this pore structure as immobile and non-deformable phases, and liquid and gas are restricted to flow in the residual.

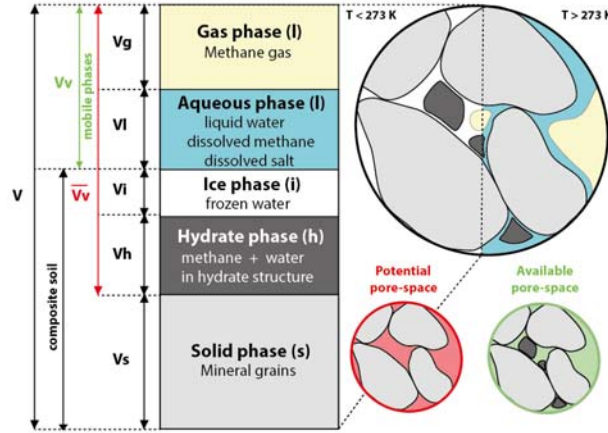


Figure 2: Volumetric relationships and pore-scale phase distribution for MHBS in a representative control volume (RCV). Note that for simplicity the scheme shows complete transformation of liquid water into ice at freezing temperature, the formulation, however, considers the presence of unfrozen water below freezing temperature.

2.2 Governing equations

The governing equations for non-isothermal multiphase flow of water and gas through porous deformable saline media presented by Olivella et al. (1996) have been modified here to capture the basic mechanisms involved in the physical process of hydrate and ice phase change.

2.2.1 Balance equations

In MHBS systems, the mass change of fluid is caused by fluid flow and hydrate and ice dissociation. Thus, the mass balance equations for water and methane present in the medium are written as:

$$\frac{\partial [(\theta_l^w s_l + \theta_g^w s_g)(1-s_l) + \theta_l^w s_l(1-s_h) + \theta_h^w s_h] \bar{\phi}}{\partial t} + \text{div}(j_h^w + j_l^w + j_l^w + j_g^w) = 0 \quad (2)$$

$$\frac{\partial [(\theta_l^m s_l + \theta_g^m s_g)(1-s_l)(1-s_h) + \theta_h^m s_h] \bar{\phi}}{\partial t} + \text{div}(j_h^m + j_l^m + j_g^m) = 0 \quad (3)$$

Where θ_l^w is determined by both molecular diffusion and mechanical dispersion of salt and methane dissolved in liquid water, and the mass flux of water and methane in non-mobile phases (i.e., $j_h^w, j_l^w, j_g^w, j_h^m, j_l^m, j_g^m$) are controlled by hydrate and ice phase change.

Hydrate formation-dissociation is assumed here to be governed by first order kinetics as suggested by Kim et al. (1987) and Englezos et al. (1987), in which the rate of phase change is proportional to the product of surface area and driving force (i.e. pressure difference between the phase-equilibrium and existing pressure):

$$R_h(T, P_g) = \bar{\phi} S_h A_{hs} \left[K_a (P_{atss}(T) - P_g) - K_f (P_g - P_{atss}(T)) \right] \quad (4)$$

Considering null mechanical deformation of the pores media the mass change of methane and water related with hydrate dissociation can be rewritten from equation 4 as:

$$\frac{\partial m_h^m}{\partial t} = \frac{\partial \theta_h^m S_h \bar{\phi}}{\partial t} = -M_m R_h(T, P_g) \quad (5)$$

$$\frac{\partial m_h^w}{\partial t} = \frac{\partial \theta_h^w S_h \bar{\phi}}{\partial t} = -M_w N_h R_h(T, P_g) \quad (6)$$

Where the incremental variation in hydrate saturation within a calculation cycle is given by:

$$\frac{\partial S_h}{\partial t} = -\frac{M_h}{\bar{\phi} \rho_h} R_h(T, P_g) \quad (7)$$

On the other hand, changes in ice saturation due to water freezing or ice melting are computed here by combining the Clausius–Clapeyron equation and the Van Genuchten model as suggested by Nishimura et al., (2009):

$$S_i = \left(1 + \left(\frac{1 - \left(1 - \frac{\rho_i}{\rho_t}\right) F_i - \rho_i \ln\left(\frac{T}{273.15}\right)}{F} \right)^{\frac{1}{1-\lambda}} \right)^{-\lambda} \quad (8)$$

2.2.2 Energy balance

The energy consumption or liberation associated to hydrate and ice phase change are taken into consideration here using the corresponding latent heats of dissociation and melting respectively:

$$L_{\text{melting}} = 3.34e^5 \frac{J}{Kg} \quad (9)$$

$$L_{\text{dissociation}} = 3.39e^5 \frac{J}{Kg} \quad (10)$$

Hence, the formulation captures energy changes during endothermic and/or exothermic processes through specific internal energies and the corresponding changes in volume fractions.

3 MODEL PERFORMANCE

The model performance focus on predicting the evolution of the primary thermophysical properties (e.g., pressure, temperature, phase saturation distribution, salt concentration) in hydrate-bearing systems subjected to changes in pressure and temperature that can induce hydrate dissociation and reformation. This section reproduces one of the benchmark study cases designed by the National Energy Technology Laboratory (NETL) as part of the national methane hydrate reservoir simulator code comparison study. The study case analyses a closed domain subjected to changes in pressure and temperature along its extension. From the specified initial conditions (Figure 3) the simulations proceeds to equilibrium conditions in temperature and pressure, dissociating and reforming the hydrate phase during the transition process.

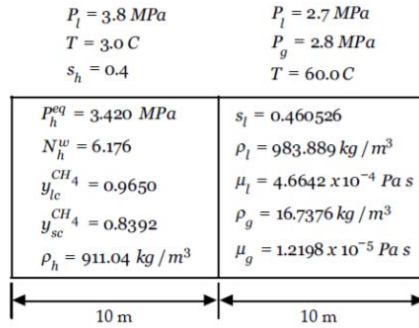


Figure 3: Schematic representation as reported in Benchmark test 2 (NETL)

Figure 4 illustrates the transition to equilibrium through the evolution of gas pressure, hydrate saturation and temperature profiles along the sample at 1, 10, 100 and 1000 days.

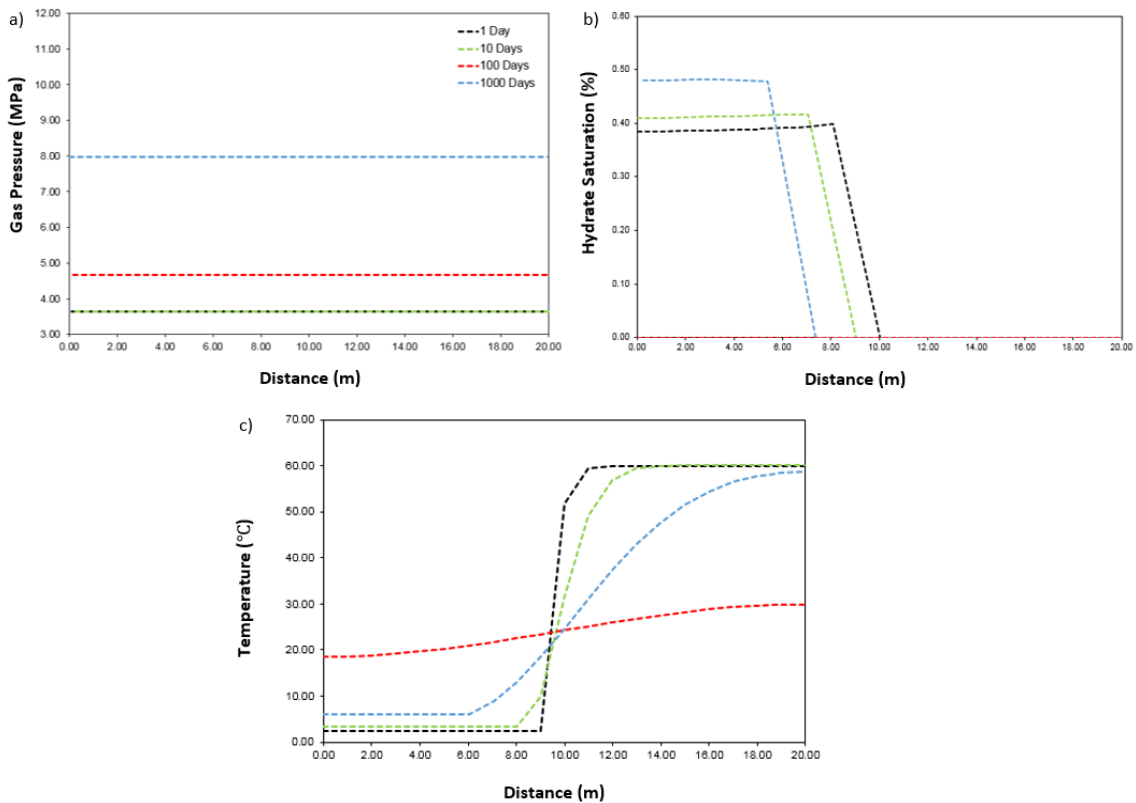


Figure 4: Profiles of a) gas pressure, b) hydrate saturation and c) temperature along the reservoir at 1, 10, 100 and 1000 days.

Hydrate dissociation occurs initially in response to both thermal stimulation and depressurization; however, later in time dissociation is principally due to thermal stimulation as the released CH_4 gas increases the system pressure above the initial conditions. After 10 days, hydrate dissociation occurs in conjunction with hydrate creation on the left side of the dissociation front caused by the gas migration and the endothermic cooling of the system.

7 CONCLUSIONS

A new mathematical formulation has been developed to analyze coupled TH problems involving gas hydrate bearing sediments. The formulation has been implemented in CODE_BRIGHT extending its modelling capabilities for hydrate systems in deformable porous and fractured media. The TH capabilities of the code are investigated here based on a benchmark study of a closed domain subjected to hydrate dissociation and reformation. The model results show a reasonable evolution of the primary variables of the system, where the equilibration of the temperature and pressure along the reservoir trigger hydrate phase change. This paper focus on several processes of interest to the simulation of CH₄ production from gas hydrates in porous media including multi-fluid flow and heat transport along with hydrate and ice phase transitions. This piece of work does not assess the geomechanical performance of the sediment during the dissociation phenomena, but the formulation already employs the Hydrate-CASM constitutive model (De La Fuente et.al, n.d, submitted) to account for the geomechanical effect of hydrate saturation in the sediment response. The next step in the model development will include the analysis of the mechanical changes induced during hydrate formation and dissociation and the assessment of the reservoir geomechanical performance.

NOTATION:

$\bar{\phi}$	Potential porosity	R_h	Kinetic rate of hydrate phase change	m	Component mass
ρ	Density	A_{hs}	Hydrate surface reactive area	M	Molecular mass of a component
\bar{j}	Total mass flux	K_d	Dissociation constant	N	Hydrate number
\bar{i}	Non-advective mass flux	P_{atss}	Dissociation pressure	L	Latent heat
S_x	Degree of Saturation	P_g	Gas pressure	λ	Shape function for retention curve
θ	Mass content per unit volume of phase	K_f	Formation constant		

REFERENCES

- Archer, D. (2007). Methane hydrate stability and anthropogenic climate change. *Biogeosciences*, 4, 521–544.
- Boswell, Ray et al. (2017), The increasingly complex challenge of gas hydrate reservoir simulation. Proceeding of the 9th International Conference on Gas Hydrates.
- De La Fuente, M., J. Vaunat, and H. Marín-Moreno. (n.d, submitted to Journal of Geophysical Research - Solid Earth), The Hydrate-CASM for modeling the geomechanical behavior of methane hydrate-bearing sediments.
- Englezos, P., Kalogerakis, N., Dholabhai, P. D. & Bishnoi, P. R. (1987). Kinetics of Formation of Methane and Ethane Gas Hydrates. *Chemical Engineering Science* 42(11), 2647–2658.
- Jung, J. W., & Santamarina, J. C. (2011). Hydrate adhesive and tensile strengths, *I2*(8), 1–9.
- Kim, H., Bishnoi, P., Heidemann, R. & Rizvi, S. (1987). Kinetics of methane hydrate decomposition. *Chemical Engineering Science* 42(7), 1645– 1653. 42.
- Kimoto, S., Oka, F., & Fushita, T. (2010). A chemo–thermo–mechanically coupled analysis of ground deformation induced by gas hydrate dissociation. *International Journal of Mechanical Sciences*, 52(2), 365–376.

- Klar, A., Uchida, S., Soga, K., & Yamamoto, K. (2013). Explicitly Coupled Thermal Flow Mechanical Formulation for Gas-Hydrate Sediments. *SPE Journal*, 18(2), 196–206. <https://doi.org/10.2118/162859-PA>
- Krey, V., Canadell, J. G., Nakicenovic, N., Abe, Y., Andruleit, H., Archer, D., ... Yakushev, V. (2009). Gas hydrates: entrance to a methane age or climate threat? *Environmental Research Letters*, 4(3), 34007.
- Kvenvolden, K. a. (1988). Methane hydrate: a major reservoir of carbon in the shallow geosphere? *Chemical Geology*, 71(1–3), 41–51.
- Max, M.D., Johnson, A. H. (2016). Exploration and Production of Oceanic Natural Gas Hydrate: Critical Factors for Commercialization. Springer International Publishing, Switzerland.
- Minshull, T. A., Marín-Moreno, H., Armstrong McKay, D. I., & Wilson, P. A. (2016). Mechanistic insights into a hydrate contribution to the Paleocene-Eocene carbon cycle perturbation from coupled thermohydraulic simulations. *Geophysical Research Letters*, 43(16), 8637–8644. <https://doi.org/10.1002/2016GL069676>
- Muradov, N. (2013). Decarbonization at crossroads: the cessation of the positive historical trend or a temporary detour? *Energy & Environmental Science*, 6(4), 1060.
- Nishimura, S., Gens, A., Jardine, R. J., & Olivella, S. (2009). THM-coupled finite element analysis of frozen soil: formulation and application. *Géotechnique*, 59(3), 159–171.
- Nixon, M. F., and J. L. H. G. (2007). Submarine slope failure due to gas hydrate dissociation: A preliminary quantification. *Can. Geotech. J.*, 44, 314–325, [doi:10.1139/T06-121](https://doi.org/10.1139/T06-121).
- Olivella, S., Gens, A., Carrera, J., Alonso, E. E. (1996). Numerical formulation for a simulator (CODE BRIGHT) for the coupled analysis of saline media. *Eng. Comput.* 13, 87–112.
- Rutqvist, J., G. J. Moridis, T. Grover, and T. C. (2008). Geomechanical response of known permafrost hydrate deposits to depressurization-induced production, paper 5726 presented at the 6th International Conference on Gas Hydrates, Chevron, Vancouver, B. C., Canada, 6–10 July.
- Sánchez M, G. X. (n.d.). Geomechanical and numerical modeling of gas hydrate sediments. In: Wuttke, Bauer, Sanchez, editors. 1st International conference on energy geotechnics, Kiel, Germany. Energy geotechnics. CRC Press/Balkema; 2016. p. 19–24. 2016.
- Sultan, N., Cochonot, P., Foucher, J., & Mienert, J. (2004). Effect of Gas Hydrates Dissociation on Seafloor Slope. *Simulation*, 213(December), 103–111.
- Uchida, S., K. Soga, and K. Yamamoto. (2012), Critical state soil constitutive model for methane hydrate soil. *Journal of Geophysical Research: Solid Earth* 117(B3).